creative commons
COMMONS DEED

저작자표시-비영리-변경금지 2.0 대한민국

이용자는 아래의 조건을 따르는 경우에 한하여 자유롭게

- 이 저작물을 복제, 배포, 전송, 전시, 공연 및 방송할 수 있습니다.

다음과 같은 조건을 따라야 합니다:

저작자표시. 귀하는 원저작자를 표시하여야 합니다.

비영리. 귀하는 이 저작물을 영리 목적으로 이용할 수 없습니다.

변경금지. 귀하는 이 저작물을 개작, 변형 또는 가공할 수 없습니다.

- 귀하는, 이 저작물의 재이용이나 배포의 경우, 이 저작물에 적용된 이용허락조건을 명확하게 나타내어야 합니다.
- 저작권자로부터 별도의 허가를 받으면 이러한 조건들은 적용되지 않습니다.

저작권법에 따른 이용자의 권리는 위의 내용에 의하여 영향을 받지 않습니다.

이것은 이용허락규약(Legal Code)을 이해하기 쉽게 요약한 것입니다.

Disclaimer

dCollection

Ph.D. DISSERTATION

Computational Investigation on the Anisotropic Surface Structures and Growth of GaAs: from *Ab Initio* to Thermodynamics

by

In Won Yeu

August 2020

DEPARTMENT OF MATERIALS SCIENCE AND ENGINEERING

COLLEGE OF ENGINEERING

SEOUL NATIONAL UNIVERSITY

Computational Investigation on the Anisotropic Surface Structures and Growth of GaAs: from *Ab Initio* to Thermodynamics

Advisor : Prof. Cheol Seong Hwang

by

In Won Yeu

A thesis submitted to the Graduate Faculty
of Seoul National University in partial fulfillment of the requirements
for the Degree of Doctor of Philosophy
Department of Materials Science and Engineering

August 2020

Approved
by

Chairman of Advisory Committee : Seungwu Han
Vice-chairman of Advisory Committee : Cheol Seong Hwang
Advisory Committee : Gun-Do Lee
Advisory Committee : Jung-Hae Choi
Advisory Committee : Sangtae Kim

Abstract

Computational Investigation on the Anisotropic Surface Structures and Growth of GaAs: from *Ab Initio* to Thermodynamics

In Won Yeu

Materials Science and Engineering

College of Engineering

Seoul National University

Over the past decades, the vapor-phase growth techniques of III-V nanoscale materials have improved tremendously by careful control of the growth variables: growth mode, growth conditions of temperature (T) and pressure (P), and substrate orientation. For such nanoscale growth, the growth condition dependent variation in surface energy and reconstruction plays a critical role in determining the anisotropic interaction between vapor sources and crystalline surfaces. Nevertheless, the lack of atomic-scale understanding makes both experimental and theoretical approaches heuristic, which deters the development in precise control of the growth. This dissertation provides a step-by-step *ab initio* thermodynamic approach based on density functional theory (DFT), to take a step forward in the theoretical modeling on the growth of III-V nanomaterials. First, the variation in surface reconstructions of GaAs (100), a representative surface of III-V compounds, was calculated as a function of T and P. Combination of *ab initio* calculation technique with the thermodynamic treatment of the vapor-phase growth system enabled us to predict surface phase diagram under any T–P condition. The effects of the vibrational and configurational entropy, which has been commonly neglected in conventional

atomic-scale calculations, were thoroughly investigated. Second, the equilibrium crystal shapes (ECS)s of GaAs were predicted by combining the surface energies of several low-index surfaces. At this stage, an unknown (111)B reconstruction was proposed as stabilized at high T by high surface entropy. Finally, the mechanism on the unidirectional growth along a certain <111>B direction and the polarity dependence of stacking-fault formation was fully elucidated for the growth of GaAs nanowire (NW). It was identified that the unidirectional growth is the consequence of anisotropic adsorption on crystallographic surfaces with different bonding states, leading to the anisotropic surface nucleation. In addition, the intriguing asymmetric formation of stacking sequence during the growth along the two opposite directions of a polar direction, <111>A and <111>B in zinc-blende structure, was demonstrated to be originated from the difference in the polar surfaces, (111)A and (111)B. The overall *ab initio* approaches are truly independent of any empirical data, bridging the scale-gap between the atomistic DFT calculation at 0 K and the macroscopic growth processes under arbitrary growth conditions. The remarkable agreements with experimental observations validate the simulation methods, and thus will contribute to the control of nanoscale growth not only for GaAs but also for other materials.

Keywords: III-V surface reconstruction, equilibrium crystal shape, nanowire, anisotropic growth, *ab initio* thermodynamics, surface vibration

Student Number: 2015-20877

Table of Contents

List of Tables

List of Figures

List of Abbreviations

LED	Light Emitting Diode
PV	Photovoltaic
SOC	System on Chip
SA	Selective Area
T	Temperature
P	Pressure
MBE	Molecular Beam Epitaxy
MOVPE	Metal-Organic Vapor-Phase Epitaxy
DFT	Density Functional Theory
ECS	Equilibrium Crystal Shape
NW	Nanowire
LDA	Local Density Approximation
GGA	Generalized Gradient Approximation
PAW	Projector-Augmented Wave
VASP	Vienna *Ab Initio* Simulation Package
ZB	Zinc-Blende
WZ	Wurtzite
BZ	Brillouin Zone
DOS	Density of State
ZPE	Zero Point Energy
RHEED	Reflection High-Energy Electron Diffraction
STM	Scanning Tunneling Microscopy
SF	Stacking-Fault
TW	Twin

VLS	Vapor-Liquid-Solid
OAG	Oxide-Assisted Growth
VS	Vapor-Solid
ANW	<111>A (A-polar) NW
BNW	<111>B (B-polar) NW
TEM	Transmission Electron Microscopy

Chapter 1. Introduction

1.1. Overview of III-V compounds and growth

As the Si-based electronic devices have approached the limit of innovation, III-V semiconductors with high mobility have been attracting substantial attention as an alternative material [1,2]. In addition, the III-V has been exploited in a variety of photonic applications, such as light emitting diode (LED) and photovoltaic (PV), due to its intrinsic property of direct band gap and controllability of the band gap [3-5]. The superior electronic and optical properties of III-V enable the combined electronic and photonic systems on a single chip (SOC), which has been expected to be a highly promising way to reduce the power consumption compared with conventional devices.

In order to integrate the III-V on the conventional platform with mass production, the material is desirable to be grown on the commercial Si wafer with a heterogeneous epitaxial form on the substrate [6,7]. The main technical difficulties of the epitaxial III-V on Si are the generation of dislocations, cracks, and anti-phase boundary, which are induced by the lattice mismatch, difference in the thermal expansion coefficient, and polarity of III-V, respectively. Many attempts have been carried out to solve these problems, and it has been found that selective area (SA) growth is one of the effective ways of suppressing the propagation of dislocations and cracks as well as lowering the density of the anti-phase boundary [8-13]. The limited growth area in the SA method allows the strain and thermal stress to be effectively released through surface [14]. Therefore, extensive experiments have been carried out to grow III-V in high quality and uniformity by tailoring temperature

(T) and pressure (P) conditions in vapor-phase growth techniques, such as SA molecular beam epitaxy (SA-MBE) or SA metal-organic vapor-phase epitaxy (SA-MOVPE).

1.2. Challenges in growth of III-V compounds

For the growth of III-V compounds, the two constituent elements, cation and anion, have different incorporation rate. Therefore, their actual partial pressures in MBE or MOVPE are not equal each other and usually higher for anion than for cation (V/III > 1). Depending on the substrate orientation as well as T of the substrate and P of each vapor source, the crystal morphology and the density of several planar defects change but the control of the morphology and defects has been attempted by heuristic approaches and still remained as a quite challenging task [15-18]. To obtain III-V crystals in a highly controlled manner, the interrelationship between the growth conditions and the growth characteristics has to be theoretically elucidated.

From the theoretical viewpoint, however, the material growth from the vapor phase can hardly be predicted from the simple thermodynamic or kinetic considerations. This is because both the thermodynamic and kinetic aspects contribute to the growth, and it is difficult to determine which aspect is dominant under given conditions.

During the vapor-phase growth, the formation of the crystal facets and the changes in surface energy and reconstruction govern the anisotropic interaction between vapor sources and crystal solids. The faceted crystal shape under the thermodynamic equilibrium is the consequence of minimizing total surface energy for a given volume. On the other hand, the surface reconstruction plays critical roles in making

difference in growth kinetics among different crystallographic surfaces. Despite the crucial role of the surface, a way of theoretically predicting surface energy and its effects on the anisotropic growth has yet to be fully developed.

1.3. Purpose of the dissertation

This dissertation proposes a step-by-step *ab initio* thermodynamic approach based on density functional theory (DFT), to take a step forward in the theoretical modeling on the growth of III-V materials. GaAs was selected as a representative III-V compound. Starting from the variation in surface reconstructions, equilibrium crystal shape (ECS) and adsorption-nucleation-growth kinetics were predicted by demonstrating the influence of the surface structures.

The theoretical results were thoroughly verified by showing a perfect agreement with experimental observations. Note that the conventional surface energy calculated by DFT is given as a function of the chemical potential [19-21]. The chemical potential (*ab initio* parameter) depends on the environment conditions but is difficult to be matched with a given T–P (thermodynamic parameters). In this dissertation, all the predictions were presented as a function of T and P by combining the atomic-scale calculation with the thermodynamic treatment of the vapor-solid system. It enabled us to connect the zero-temperature DFT calculations to the observations at the experimentally relevant conditions of MBE and MOVPE.

In the computational aspect, vibrational and configurational entropies, which have been commonly neglected in *ab initio* calculations for surface, were taken into account. By investigating the entropy contribution to our simulations, it was identified that the inclusion of the entropy terms is essential to achieve reliable

predictions for the systems with large entropy changes: transition from vapor to solid through adsorption on the various surfaces with different bonding states.

1.4. Organization of the dissertation

The dissertation is organized as follows. The first chapter is an introduction to what we are going to focus on, and defines the problem and scope to be covered in this dissertation. Chapter 2 explains theoretical backgrounds and calculation methods that are required to understand and reproduce the results presented throughout this dissertation. In chapter 3, the surface phase diagram that shows the variation in reconstructions of GaAs (100) is established. Chapter 4 describes T–P dependent ECS by constructing the Wulff shape from the calculated surface energy of several low-index surfaces. In this chapter, an unreported (111)B reconstruction is proposed, which is stabilized at high T by high vibrational entropy. In the fifth chapter, the mechanism behind the unidirectional growth (nanowire growth) along <111>B direction is elucidated in terms of the anisotropic adsorption behavior of Ga and As sources. In addition, the involvement of stacking-fault and polytypism in the grown GaAs nanowire (NW) is explored along with its dependence on the growth condition and direction. In every chapter, the entropy contribution to the prediction is discussed and an effort to verify the simulation is made by comparison with available experimental reports.

1.5. Bibliography

[1] J. A. Del Alamo, Nanometre-Scale Electronics with III–V Compound Semiconductors, *Nature*, **479**, 317-323, (2011).

[2] H. Riel, L.-E. Wernersson, M. Hong and J. A. Del Alamo, III–V Compound Semiconductor Transistors—from Planar to Nanowire Structures, *MRS Bull.*, **39**, 668-677, (2014).

[3] H. Kroemer, Quasi-Electric Fields and Band Offsets: Teaching Electrons New Tricks (Nobel Lecture), *ChemPhysChem*, **2**, 490-499, (2001).

[4] M. S. Gudiksen, L. J. Lauhon, J. Wang, D. C. Smith and C. M. Lieber, Growth of Nanowire Superlattice Structures for Nanoscale Photonics and Electronics, *Nature*, **415**, 617-620, (2002).

[5] M. Yao, N. Huang, S. Cong, C.-Y. Chi, M. A. Seyedi, Y.-T. Lin, Y. Cao, M. L. Povinelli, P. D. Dapkus and C. Zhou, GaAs Nanowire Array Solar Cells with Axial p–i–n Junctions, *Nano Lett.*, **14**, 3293-3303, (2014).

[6] D.-M. Geum, M.-S. Park, J. Y. Lim, H.-D. Yang, J. D. Song, C. Z. Kim, E. Yoon, S. Kim and W. J. Choi, Ultra-High-Throughput Production of III-V/Si Wafer for Electronic and Photonic Applications, *Sci. Rep.*, **6**, 20610, (2016).

[7] Y. B. Bolkhovityanov and O. P. Pchelyakov, GaAs Epitaxy on Si Substrates: Modern Status of Research and Engineering, *Phys.-Usp.*, **51**, 437, (2008).

[8] O. Skibitzki, I. Prieto, R. Kozak, G. Capellini, P. Zaumseil, Y. A. R. Dasilva, M. D. Rossell, R. Erni, H. von Känel and T. Schroeder, Structural and Optical Characterization of GaAs Nano-Crystals Selectively Grown on Si Nano-Tips by MOVPE, *Nanotechnology*, **28**, 135301, (2017).

[9] C.-P. Chu, S. Arafin, T. Nie, K. Yao, X. Kou, L. He, C.-Y. Wang, S.-Y. Chen, L.-J. Chen and S. M. Qasim, Nanoscale Growth of GaAs on Patterned

Si (111) Substrates by Molecular Beam Epitaxy, *Cryst. Growth Des.*, **14**, 593-598, (2014).

[10] C. V. Falub, H. von Känel, F. Isa, R. Bergamaschini, A. Marzegalli, D. Chrastina, G. Isella, E. Müller, P. Niedermann and L. Miglio, Scaling Hetero-Epitaxy from Layers to Three-Dimensional Crystals, *Science*, **335**, 1330-1334, (2012).

[11] J. Li, J. Bai, J.-S. Park, B. Adekore, K. Fox, M. Carroll, A. Lochtefeld and Z. Shellenbarger, Defect Reduction of GaAs Epitaxy on Si (001) Using Selective Aspect Ratio Trapping, *Appl. Phys. Lett.*, **91**, 021114, (2007).

[12] C.-W. Hsu, Y.-F. Chen and Y.-K. Su, Nano Epitaxial Growth of GaAs on Si (001), *Appl. Phys. Lett.*, **99**, 133115, (2011).

[13] P. Aseev, A. Fursina, F. Boekhout, F. Krizek, J. E. Sestoft, F. Borsoi, S. Heedt, G. Wang, L. Binci and S. Martí-Sánchez, Selectivity Map for Molecular Beam Epitaxy of Advanced III–V Quantum Nanowire Networks, *Nano Lett.*, **19**, 218-227, (2018).

[14] F. Glas, Critical Dimensions for the Plastic Relaxation of Strained Axial Heterostructures in Free-Standing Nanowires, *Phys. Rev. B*, **74**, 121302, (2006).

[15] J. Motohisa, J. Noborisaka, J. Takeda, M. Inari and T. Fukui, Catalyst-Free Selective-Area MOVPE of Semiconductor Nanowires on (111) B Oriented Substrates, *J. Cryst. Growth*, **272**, 180-185, (2004).

[16] K. Ikejiri, J. Noborisaka, S. Hara, J. Motohisa and T. Fukui, Mechanism of Catalyst-Free Growth of GaAs Nanowires by Selective Area MOVPE, *J. Cryst. Growth*, **298**, 616-619, (2007).

[17] C. Renard, N. Cherkashin, A. Jaffre, T. Molière, G. Hallais, L. Vincent, J. Alvarez, D. Mencaraglia, A. Michel and D. Bouchier, Growth of High Quality Micrometer Scale GaAs/Si Crystals from (001) Si Nano-Areas in SiO2, *J. Cryst. Growth*, **401**, 554-558, (2014).

[18] L. Güniat, P. Caroff and A. Fontcuberta i Morral, Vapor Phase Growth of Semiconductor Nanowires: Key Developments and Open Questions, *Chem. Rev.*, **119**, 8958-8971, (2019).

[19] N. Moll, A. Kley, E. Pehlke and M. Scheffler, GaAs Equilibrium Crystal Shape from First Principles, *Phys. Rev. B*, **54**, 8844, (1996).

[20] N. Moll, M. Scheffler and E. Pehlke, Influence of Surface Stress on the Equilibrium Shape of Strained Quantum Dots, *Phys. Rev. B*, **58**, 4566, (1998).

[21] Q. Liu, N. Moll, M. Scheffler and E. Pehlke, Equilibrium Shapes and Energies of Coherent Strained InP Islands, *Phys. Rev. B*, **60**, 17008, (1999).

Chapter 2. Theoretical backgrounds

2.1. Density functional theory (DFT)

The following descriptions in this part are brief explanations of the basic formulas that form the background of DFT. For more details, the books written by Sholl and Steckel [1] and Giustino [2] are excellent texts devoted to the fundamentals and applications of DFT from a practical point of view.

2.1.1. Kohn-Sham equations

One of the most fundamental things that describe the state of a given material is the energy of the atomic configuration $\{R_I\}$, where $\{R_I\}$ indicates the positions of atoms that constitute the material. This is called the potential energy surface, $E(\{R_I\})$, which contains the relevant information needed to describe almost all the properties of the collection of atoms. The attempts to compute $E(\{R_I\})$ are based on the *Born-Oppenheimer approximation: as electrons respond to change in environment much faster than nuclei, nuclei can be assumed to be held immobile while electrons move*. It enables us to treat the behavior of electrons as mathematical problem in the field given by a set of fixed nuclei, and the governing equation of the behavior of electrons is the Schrödinger equation:

$$\left[-\frac{\hbar^2}{2m}\sum_{i=1}^{N}\nabla_i^2 + \sum_{i=1}^{N}V(r_i) + \sum_{i=1}^{N}\sum_{j<i}U(r_i, r_j)\right]\Psi = E\Psi, \tag{2.1}$$

where m is the electron mass; r_i denotes position of electron i; N is the number of electrons in the system; and E is the ground state energy of the electrons where the state of the electrons is represented by $\Psi = \Psi(r_1, \dots, r_N)$. The first, second, and third terms in bracket on the left-hand side of Eq. (2.1) correspond to the kinetic energy

of electron, the interaction energy between electron and nuclei, and the interaction energy between different electrons, respectively.

Unfortunately, except for hydrogen atom, the Schrödinger equation of material systems that we are interested in cannot be solved even by numerical computer simulation due to the complications of the many-body interaction among electrons, $\sum_{i=1}^{N}\sum_{j<i}U(r_i,r_j)$. The alternative of the Schrödinger equation is the Kohn-Sham equations [3]:

$$\left[-\frac{\hbar^2}{2m}\nabla^2+V(r)+V_H(r)+V_{XC}(r)\right]\phi_i(r)=\varepsilon_i\phi_i(r), \tag{2.2}$$

where ε_i and ϕ_i are the Kohn-Sham energy and wave function of a single electron i. The first and second terms in bracket on the left-hand side of Eq. (2.2) indicate the kinetic energy and the external nuclear potential, respectively. The third term is referred to as the Hartree potential, $V_H(r)$, which describes the interaction between an electron and the total electron density contributed by all the electrons, $n(r)$. The remaining fourth term is called the exchange and correlation potential, $V_{XC}(r)$, which is defined to contain quantum mechanical effects and the correction for the unphysical self-interaction included in the Hartree potential, that is, interaction between an electron and itself through the total electron density.

Compared to the Schrödinger equation in Eq. (2.1), the summation among the N electrons is excluded in Eq. (2.2), which shows the one-body feature of the Kohn-Sham equations. Instead, the interaction between different electrons, $\sum_{i=1}^{N}\sum_{j<i}U(r_i,r_j)$ in Eq. (2.1), is replaced by the dependence of $V_H(r)=e^2\int\frac{n(r')}{|r-r'|}d^3r'$ and $V_{XC}(r)=\frac{\delta E[n(r)]}{\delta n(r)}$ on the total electron density, $n(r)=\sum_{i=1}^{N}\phi_i^*(r)\phi_i(r)$. By the transformation from N-body to one-body problem, the

computational cost is highly diminished, which allows the energy prediction of materials constituted of many electrons by numerically solving the electronic structure equation.

The above-explained reformulation of the governing equation of electrons is based on the two fundamental theorems proved by Hohenberg-Kohn [4]: *(i) The ground state energy from Schrödinger equation is a unique functional of the electron density; (ii) The electron density that minimizes the energy of the overall functional is the true electron density corresponding to the full solution of the Schrödinger equation*. Since the ground state energy and other related properties are a unique functional of the electron density, *E[n(r)]*, the electronic structure calculation is usually referred to as DFT. It is notable that the total electron density, $n(r) = \sum_{i=1}^{N} \phi_i^*(r)\phi_i(r)$, is not only the solution but also the component of the Kohn-Sham equations through the two functional potentials: $V_H(r)$ and $V_{XC}(r)$. Therefore, the Kohn-Sham equations must be solved by the iterative method until the self-consistency is achieved as illustrated in Fig. 2.1.

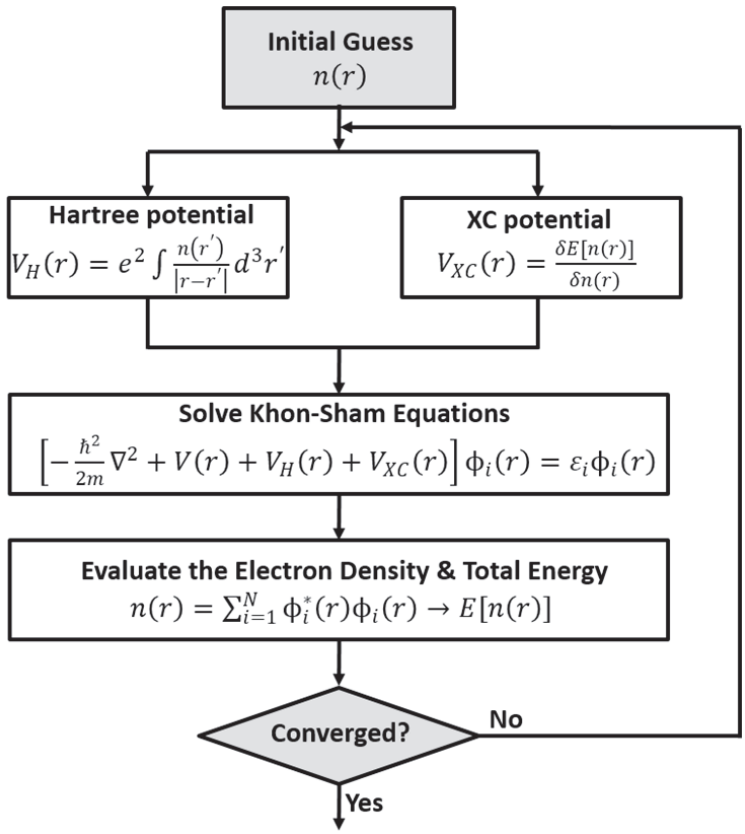

Figure 2.1 Schematic of the iterative DFT algorithm to find the self-consistent solutions of the Kohn-Sham equations.

2.1.2. Exchange and correlation potential

The accuracy of the solution to the Kohn-Sham equations is determined by the exchange and correlation potential, $V_{XC}(r)$; If the exact from of $V_{XC}(r)$ was known, the following ground state energy and density of electrons would be guaranteed to be accurate. However, what is the exact form of the $V_{XC}(r)$ is not known and approximations to the exchange and correlation potential are the best option available today.

In the approximation, the potential values at each position are parameterized by

using the free electron gas model in which the exact formula of the $V_{XC}(r)$ can be derived. In the case that only the local electron density is used for the parametrization, the approximated potential is called the local density approximation (LDA), $V_{XC}^{LDA}(r) = V_{XC}^{electron\ gas}[n(r)]$. On the other hand, when the local gradient of the electron density as well as the local electron density is employed, the resulting potential is referred to as the generalized gradient approximation (GGA), $V_{XC}^{GGA}(r) = V_{XC}^{electron\ gas}[n(r), \nabla n(r)]$. The two classes, LDA and GGA, are the most widely used functional as the exchange and correlation potential.

2.1.3. Details in DFT calculations

There is no ideal one exchange and correlation potential suitable for all kinds of structure and property calculations. For example, as the strength of the gradient corrections in GGA functionals increases, surface energy tends to be more underestimated while the prediction on adsorption energy becomes improved [5]. Therefore, the exchange and correlation potential must be appropriately selected according to the type of calculation.

For all the calculations in this dissertation, the LDA-based Ceperley-Alder exchange correlation functional [6] parameterized by Perdew and Zunger [7] was used with the projector-augmented wave (PAW) [8,9], as implemented in the Vienna *Ab Initio* Simulation Package (VASP) [10-13]. The 3d, 4s, and 4p orbitals of Ga, as well as the 4s and 4p orbitals of As, were treated as valence electrons. The plane-wave basis function was expanded within 500 eV cutoff energy, and Gamma-centered 12×12×12 k-points were sampled for the conventional zinc-blende (ZB) unit cell. The convergence of the bulk total energy with respect to the cutoff energy

and the number of k-points were all confirmed within 10 meV per formula unit. The atoms in bulk unit cell were relaxed until the forces were less than 10^{-4} eV/Å. On the other hand, the atoms at the top five layers in slab supercell were relaxed until the forces were less than 0.02 eV/Å, while the other atoms at the bottom layers were fixed.

For the slab supercell generated to represent the surface, the in-plane size was determined according to the symmetry of reconstruction, and the height of the slab was set to contain sufficient atomic layers (at least nine atomic layers) and vacuum separation (> 15 Å). Then, the k-points along the in-plane directions of the slab supercell were scaled according to the supercell size to maintain comparable k-point density to that of the conventional ZB unit cell. The dipole correction [14] along the vacuum direction and the anti-symmetrical slab having the fixed bottom side passivated by pseudo-hydrogen were employed, to eliminate undesired interaction between the top and bottom surfaces.

2.2. Surface energy calculations and crystal symmetry

The crystal structure of III-V compounds is either ZB or wurtizte (WZ): the stable structure of nitride (III-N) is WZ, while that of phosphide (III-P), arsenide (III-As), and antimonide (III-SB) is ZB [15]. Since both the ZB ($F\bar{4}3m$) and WZ ($P6_3mc$) structures have no inversion symmetry (*i.e.*, non-centrosymmetric), various inequivalent surfaces exist and some of them along polar directions show distinctive structural and physical properties between the two opposite surfaces [16,17]. Depending on whether the surface orientation is nonpolar or polar, the method of obtaining the surface energy is different.

2.2.1. Slab method for nonpolar surfaces

In the case of nonpolar surfaces, the conventional slab geometry was used to calculate surface energy. The representative low-index surfaces to which the slab method is applicable are (100) and (110) of ZB-GaAs. Along <100> directions, $\bar{4}$ rotoinversion axis is aligned as confirmed by the atomic structure in Fig. 2.2(a) where the top and bottom are flipped and rotated by 4-fold from each other. Mirror plane perpendicular to <110> directions is also identified in Fig. 2.2(b). For these (100) and (110) surfaces with other nonpolar surfaces, the hydrogen-passivated surface energy including the atomic energy of the hydrogen ($\gamma_H + \alpha$) is evaluated simply by the energy difference between the slab and bulk structures:

$$\gamma_H + \alpha = \frac{\left(E_{surf}^{elec}\right) - N_{Ga}(\mu_{Ga(GaAs)}) - N_{As}(\mu_{As(GaAs)})}{2A}, \quad (2.3)$$

where E_{surf}^{elec} is the ground state electronic energy of the hydrogen-passivated symmetrical slab (*e.g.*, Fig. 2.2(a) and (b)); $\mu_{Ga(GaAs)}$ and $\mu_{As(GaAs)}$ are the chemical potentials of the Ga and As species in the reservoir (ZB-GaAs), respectively; and N_{Ga}, N_{As}, and A are the numbers of Ga and As atoms and the surface area of the slab, respectively. Note that the hydrogen used for the passivation is pseudo-hydrogen with a non-integer core charge Z, together with Z electrons. The dangling bonds of Ga atom were saturated by the pseudo-hydrogen with Z=1.25, while those of As atom were saturated by the pseudo-hydrogen with Z=0.75. These pseudo-hydrogens are widely utilized to passivate III-V dangling bonds [18].

After obtaining the electronic energy of the hydrogen-passivated symmetrical slab by the relaxation calculation, the hydrogen atoms at either top or bottom surface were

removed and the corresponding surface was reconstructed. Then, the next relaxation was conducted only for the atoms at the reconstructed surface while the other atoms are fixed. Using the resulting energy, the surface energy of reconstruction was computed as follows:

$$\gamma^{elec} = \frac{\left(E_{surf}^{elec}\right) - N_{Ga}(\mu_{Ga(GaAs)}) - N_{As}(\mu_{As(GaAs)})}{A} - (\gamma_H + \alpha), \quad (2.4)$$

where, γ^{elec} is the electronic surface energy; and E_{surf}^{elec} is the ground state electronic energy of the reconstructed anti-symmetrical slab. The hydrogen-passivated surface energy $(\gamma_H + \alpha)$ was given by the separate calculation, Eq. (2.3), as explained above.

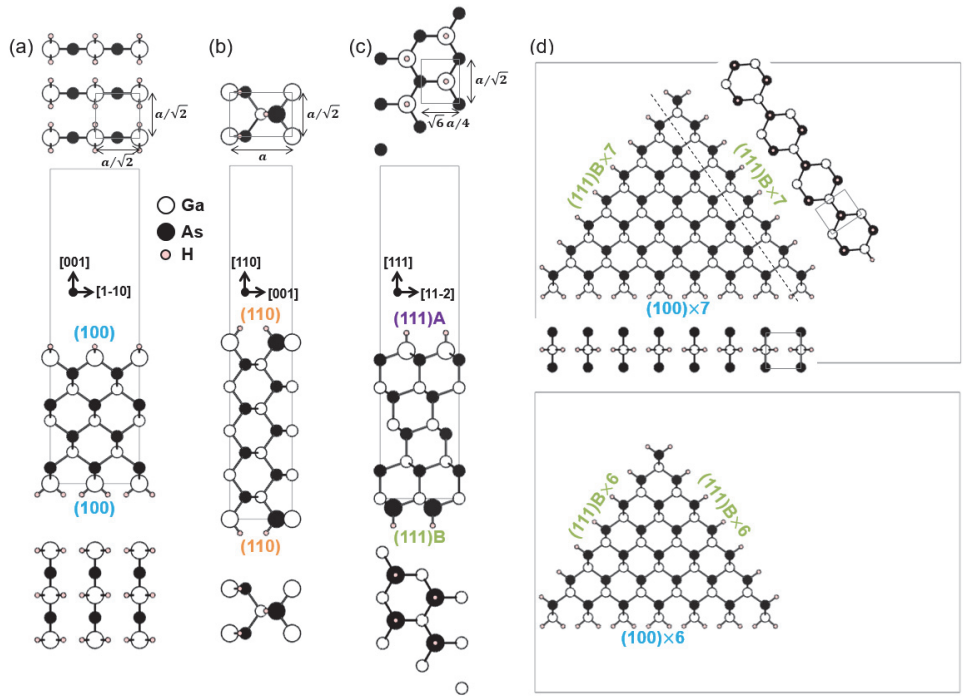

Figure 2.2 Top, side, and bottom views of the slab geometry where both the top and bottom (a) (100), (b) (110), and (c) (111) surfaces are saturated by pseudo-hydrogen. The surface (1×1) primitive cell and corresponding unit length with respect to the lattice constant of the conventional bulk cell of GaAs (a = 5.61 Å as calculated by LDA potential) are denoted in the top view. (d) Cross-sectional view of the three-dimensional wedge-shaped geometry, infinite triangular prism, consisting of two (111)B surfaces and one (100) surface saturated by pseudo-hydrogen. Insets in the large wedged structure are the corresponding normal view, in which the surface (1×1) primitive cell is marked by gray rectangle. The large and small wedged structures expose seven and six primitive cells on each of the three surfaces, respectively, as denoted in the figure.

2.2.2. Wedge method for polar surfaces

For polar surfaces, on the other hand, the construction of the hydrogen-passivated symmetrical slab is not possible. The representative low-index surface is (111) of ZB-GaAs along which 3-fold rotation axis is aligned, leading to the two different types of surfaces on the opposite directions: Ga-terminated (111)A and As-terminated (111)B as shown in Fig. 2.2(c). Therefore, the evaluation of the surface energy of either (111)A or (111)B is not allowed using the conventional slab method.

Instead, the wedge-shape geometry proposed by Zhang and Wei [19] was employed, where two (111)B and one (100) surfaces saturated by pseudo-hydrogen are exposed. Figure 2.2(d) shows the wedge geometry, which is identical with the infinite triangular prism considering the 3-dimensional periodicity. The electronic energy of the wedge-shape geometry is broken down into contributions coming from the bulk GaAs, three surfaces, and three corners. The energy contribution from the three corners is effectively canceled out by subtracting the energy of the small wedge, bottom panel in Fig. 2.2(d), from that of the large wedge, top panel in Fig. 2.2(d). The remaining energy from the subtraction includes the bulk energy of eight formula unit and the surface energy of the two (111)B and one (100) surfaces. Since the bulk energy and (100) surface energy were already calculated, the additional subtraction allows only the surface energy of (111)B saturated by pseudo-hydrogen to be extracted. Then, the surface energy of (111)A saturated by pseudo-hydrogen was obtained from the energy of (111) slab shown in Fig. 2.2(c). These hydrogen-passivated surface energies of (111)A and (111)B were taken in Eq. (2.4) to evaluate the reconstructed surface energies of (111)B and (111)A, respectively.

2.3. *Ab initio* thermodynamics for surface

As explained in the section 2.1, the electronic structure calculation programs such as VASP give us the ground state energy for a given atomic configuration $\{R_I\}$. The *ab initio* potential energy surface, $E(\{R_I\})$, contains all the relevant information required to evaluate thermodynamic properties like the chemical potential. The basic idea behind the *ab initio* thermodynamics for surface is to mathematically describe the interaction between vapor and solid by relating their corresponding thermodynamic potentials. In the following sections, we illustrate how the *ab initio* potential energy surface is employed to calculate the chemical potentials of solid and vapor phases and how their chemical potentials are related to represent the chemical interactions occurring in the solid-vapor systems. The mathematical description of the solid-vapor systems is very useful for simulating surface reactions such as catalytic reactions as well as material growth that we are concentrating on in this dissertation. For more details, the book section written by Reuter *et al.* [20] and that by Rogal and Reuter [21] will be of great help.

2.3.1. Chemical potential of solid

The chemical potential of bulk solid, $\mu_{(Solid)}(T,P)$, was considered to be the Helmholtz free energy ($F=E-TS_{vib}$) per formula unit, since the PV contribution to the Gibbs free energy ($G=F+PV$) is negligible in the low pressure solid-vapor system described in this study. The vibrational contribution to the free energy ($F^{vib}=TS_{vib}$) is defined by:

$$F^{vib} = \frac{1}{N_k}\sum_{k\in BZ}\sum_{i=1}^{M}\{\frac{\hbar w_i(k)}{2} + k_B T \ln\left(1 - e^{-\frac{\hbar w_i(k)}{k_B T}}\right)\}, \quad (2.5)$$

where, N_k and M are the numbers of k-points and phonon modes, respectively; ħ and k_B are the reduced Planck constant and the Boltzmann constant, respectively; and $w_i(k)$ is the angular frequency of the i-th phonon mode at k-point sampled in the Brillouin zone (BZ). The phonon calculations of 3-dimensional bulk crystals were carried out using PHONOPY program within the harmonic approximation [22]. In addition, since the situation described in this dissertation is the solid-vapor system at low pressures, the volume dependence of the vibrational frequency was neglected. As an example, Fig. 2.3 shows the calculated phonon density of state (DOS) of ZB-GaAs and partial phonon DOS of As in ZB-GaAs.

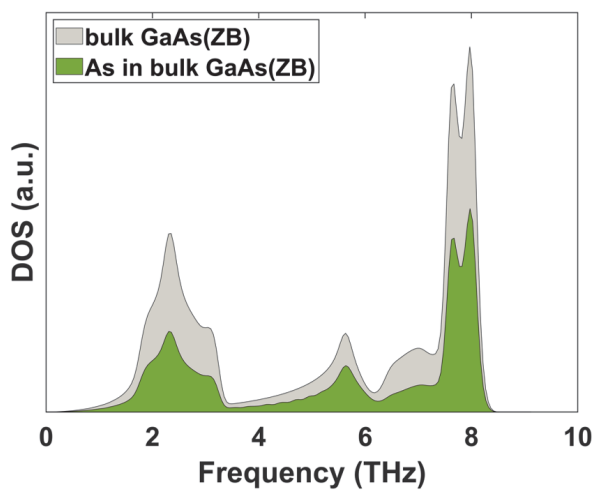

Figure 2.3 The total phonon DOS of zinc-blende (ZB) GaAs (gray area) and corresponding partial phonon DOS of As in the bulk GaAs (green area).

2.3.2. Chemical potential of vapor

On the other hand, the chemical potential of vapor phase is written as:

$$\mu_{i(Gas)}(T, P_i) = E_{i(Gas)}^{elec} + E_{i(Gas)}^{ZPE} + \Delta\mu_{i(Gas)}(T, P^o) + k_B T \ln(\frac{P_i}{P^o}), \quad (2.6)$$

where $E_{i(Gas)}^{elec}$ and $E_{i(Gas)}^{ZPE}$ $(= \sum_{i=1}^{M} \frac{\hbar w_i}{2})$ are the ground state electronic energy and

zero point energy (ZPE) of the considered vapor, respectively; P_i and P^o are the partial pressure and the standard pressure (=1 atm), respectively; and $\Delta\mu_{i(Gas)}(T, P^o)$ is the standard chemical potential. The standard chemical potentials are listed in NIST-JANAF thermochemical tables for some vapor molecules [23].

For unlisted vapor molecules, $\Delta\mu_{i(Gas)}(T, P^o)$ can be directly evaluated by using statistical mechanics in which the thermodynamic potentials of molecule are derived from the molecular partition functions of each degree of freedom (*e.g.*, translational, rotational, vibrational, and electronic freedom). We can write the free energy contributions coming from each degree of freedom as:

$$\Delta\mu_{i(Gas)}(T, P^o) = F^{vib} + F^{rot} + F^{trans} - k_B T \ln I^{spin}, \tag{2.7}$$

where F^{vib}, F^{rot}, and F^{trans} are the free energy contributions coming from vibrational, rotational, and translational motions, respectively; and I^{spin} is the electronic spin degeneracy of the ground state determined by the electron configuration of molecular orbital. In the assumption that the considered molecule is ideal gas and rigid rotor, the vibrational, rotational, and translational contributions to the free energy are defined by:

$$F^{vib} = \sum_{i=1}^{M} k_B T \ln\left(1 - e^{-\frac{\hbar w_i}{k_B T}}\right), \tag{2.8}$$

$$F^{rot} = -k_B T \ln\left(\frac{\pi^{\frac{1}{2}}}{\sigma}\sqrt{\frac{2I_A k_B T}{\hbar^2}}\sqrt{\frac{2I_B k_B T}{\hbar^2}}\sqrt{\frac{2I_C k_B T}{\hbar^2}}\right), \tag{2.9}$$

$$F^{trans} = -k_B T \ln\left[\left(\frac{2\pi m}{h^2}\right)^{\frac{3}{2}}\frac{(k_B T)^{\frac{5}{2}}}{P^o}\right], \tag{2.10}$$

respectively. In Eq. (2.8), M indicates the number of vibrational normal modes (=3N–5 for linear molecules, and =3N–6 for non-linear molecules) and w_i is the corresponding angular frequency. In Eq. (2.9), I_A, I_B, and I_C are the principal

moments of inertia; and σ is the symmetry number determined by the molecule geometry. The principal moments of inertia were calculated by diagonalization of 3-by-3 inertia tensor. In Eq. (2.10), m is the molecular mass, and h is the Planck constant. The detailed derivation of Eq. (2.7)-(2.10) can be found in the statistical mechanics textbook written by McQuarrie [24].

Figure 2.4 shows the chemical potential of oxygen molecule, $\Delta\mu_{O(O2)}(T, P^o) = \frac{1}{2}\Delta\mu_{O2}(T, P^o)$, obtained by the two different approaches: one is referring to the enthalpy and entropy tabulated in NIST-JANAF thermochemical tables (*G=H–TS*) and the other is calculating the electronic, vibrational, rotational, and translational contributions to the free energy using Eq. (2.7)-(2.10). The values of the two approaches are well matched each other, which demonstrates the validity of the chemical potential computed by the statistical mechanics.

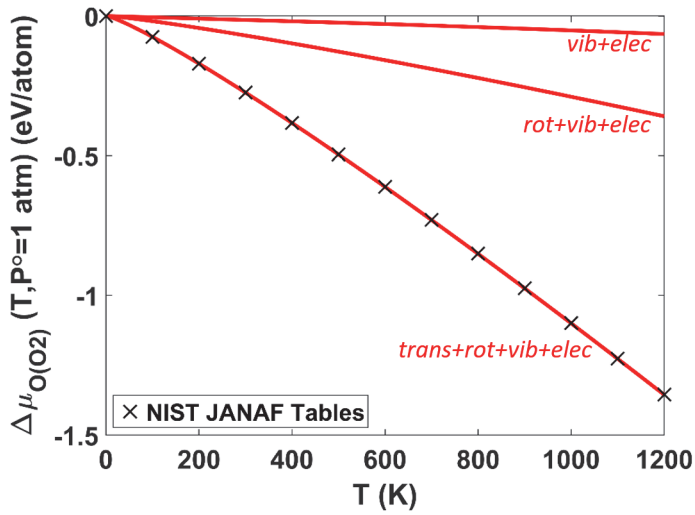

Figure 2.4 The chemical potential of oxygen molecule, $\Delta\mu_{O(O2)}(T, P^o) = \frac{1}{2}\Delta\mu_{O2}(T, P^o)$. The red lines shows the sum of free energy contributions from electronic, vibrational, rotational, and translational degrees of freedom. The chemical potentials of oxygen molecule listed in NIST-JANAF thermochemical tables are also denoted as the black cross marks for comparison.

Molecules of As_2 and As_4 are the dominant vapor environment for the growth of GaAs, because the partial pressure of As is much higher than that of Ga under common conditions in MBE or MOVPE (V/III > 1). However, the thermodynamic data of the As_2 and As_4 molecules is not available in NIST-JANAF thermochemical tables [23]. Instead, we evaluated the chemical potentials of the As_2 and As_4 molecules by directly calculating the standard chemical potential in Eq. (2.7). The required parameters in Eq. (2.8)-(2.10) are given by DFT calculations conducted on an isolated molecule in 17.5×17.5×17.5 $Å^3$ cell. With 1×1×1 k-point, the structures of the molecules were relaxed until the forces were less than 10^{-6} eV/Å and their vibrational normal frequencies were obtained by the finite displacement method

within the harmonic approximation. The resulting standard chemical potentials of the As_2 and As_4 molecules are shown in Fig. 2.5(a) and (b), respectively.

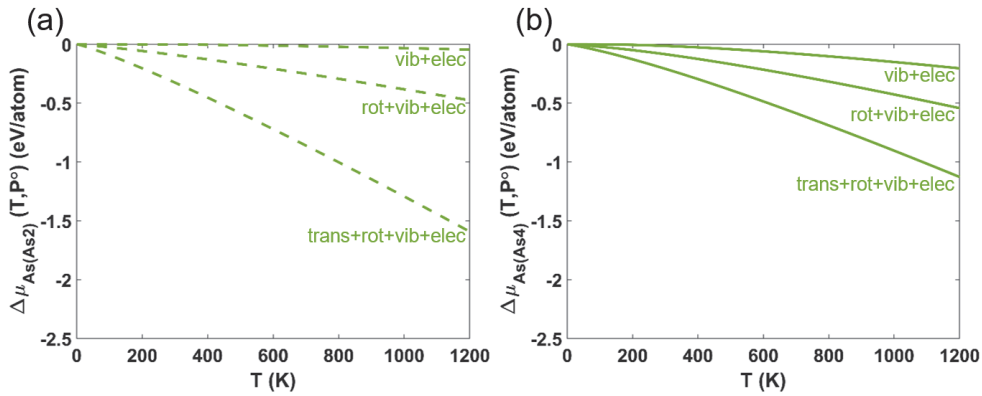

Figure 2.5 The calculated values of standard chemical potential (P^o=1 atm) of (a) As_2 and (b) As_4. Contributions of individual degrees of freedom to the standard chemical potential are denoted: translational, rotational, vibrational motions, and electronic spin degeneracy of the ground state.

By summing up the T-dependent $\Delta\mu_{i(Gas)}(T,P^o)$ with other terms in Eq. (2.6), the chemical potentials of the As_2 and As_4 molecules, $\mu_{As_2(Gas)}$ and $\mu_{As_4(Gas)}$, were evaluated as a function of T and partial P. In this study, the As vapor was considered to be a vapor mixture consisting of As_2 and As_4 molecules in equilibrium:

$$\mu_{As(Gas)} = \frac{1}{2}\mu_{As_2(Gas)} = \frac{1}{4}\mu_{As_4(Gas)}, \tag{2.11}$$

$$P_{As} = P_{As_2} + P_{As_4}, \tag{2.12}$$

where, $\mu_{As(Gas)}$, $\mu_{As_2(Gas)}$, and $\mu_{As_4(Gas)}$ are the chemical potentials of the As vapor mixture in equilibrium, As_2, and As_4, respectively; and P_{As}, P_{As_2}, and P_{As_4} indicate the total As pressure, partial pressures of As_2 and As_4, respectively. The two partial pressures in equilibrium were obtained by solving Eq. (2.11) and (2.12) at a

given T and P_{As}, and are shown in Fig. 2.6. As a result, the T–P dependent chemical potential of the As vapor in equilibrium between As_2 and As_4 could be evaluated as presented in Fig. 2.7, which acts as the surrounding vapor potential of GaAs.

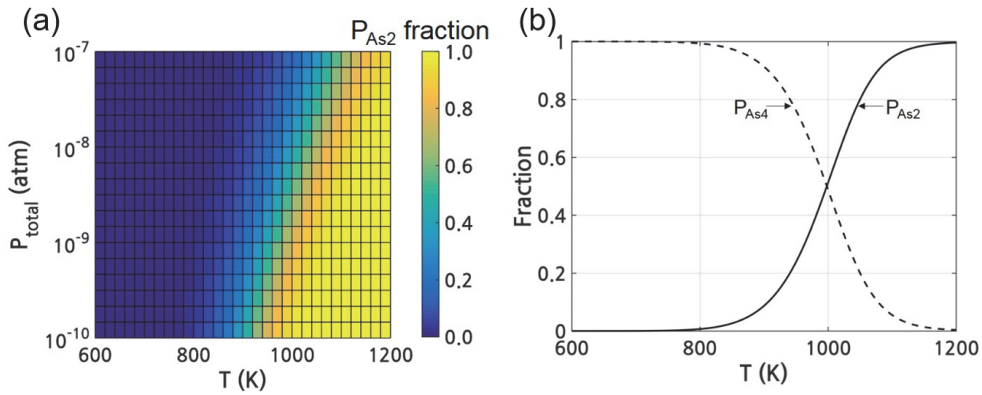

Figure 2.6 (a) Equilibrium fraction of P_{As_2} as a function of T and P_{total} $(= P_{As_2} + P_{As_4})$. (b) Fractions of P_{As_2} and P_{As_4} as a function of T at fixed P_{total} of 4×10^{-9} atm.

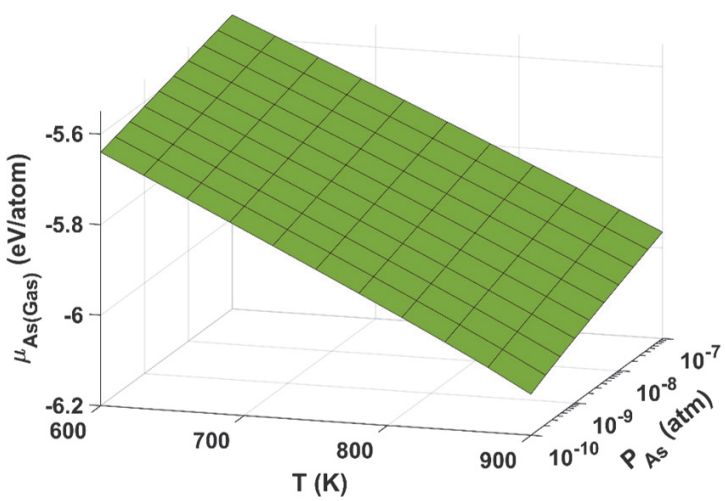

Figure 2.7 Chemical potential of a gas mixture consisting of As_2 and As_4 molecules in equilibrium.

2.3.3 Thermodynamic equilibrium for surface

The $\mu_{Ga(GaAs)}$ and $\mu_{As(GaAs)}$ in Eq. (2.3) and (2.4) can be varied depending on the surrounding conditions, but the variation is limited by the following constraints:

$$\mu_{Ga(GaAs)} + \mu_{As(GaAs)} = \mu_{GaAs(bulk)}, \tag{2.13}$$

$$\mu_{Ga(GaAs)} \leq \mu_{Ga(bulk)} \ \ and \ \ \mu_{As(GaAs)} \leq \mu_{As(bulk)}, \tag{2.14}$$

where $\mu_{GaAs(bulk)}$, $\mu_{Ga(bulk)}$, and $\mu_{As(bulk)}$ are the chemical potentials of the most stable bulk phases of GaAs, Ga, and As, respectively. The corresponding phases are ZB, orthorhombic, and rhombohedral structures for GaAs, Ga, and As, respectively. In thermodynamic equilibrium, the condition of Eq. (2.13) must be fulfilled; Eq. (2.14) is stable condition against decompositions because otherwise the decomposition from GaAs to the elemental phase would occur. By the substitution of Eq. (2.13) into Eq. (2.3) and (2.4), each equation is rearranged as a function of $\mu_{As(GaAs)}$:

$$\gamma_H + \alpha = \frac{\left(E_{surf}^{elec}\right) - N_{Ga}(\mu_{GaAs(bulk)}) - (N_{As} - N_{Ga})(\mu_{As(GaAs)})}{2A}, \tag{2.15}$$

$$\gamma^{elec} = \frac{\left(E_{surf}^{elec}\right) - N_{Ga}(\mu_{GaAs(bulk)}) - (N_{As} - N_{Ga})(\mu_{As(GaAs)})}{A} - (\gamma_H + \alpha). \tag{2.16}$$

Therefore, γ^{elec} of reconstruction is generally given as a function of $\mu_{As(GaAs)}$ and the dependency is determined by the degree of stoichiometry imbalance, $N_{Ga} - N_{As}$, of reconstruction being considered. Figure 2.8 shows examples on the surface energy of several surfaces. The slope in this figure is proportional to the $N_{Ga} - N_{As}$, the excess number of Ga atoms compared to the As atoms in the reconstruction: the positive (negative) slope indicates the number of Ga (As) atoms is greater than that of As (Ga) atoms in the reconstruction. The constrained range of x-axis, $\mu_{As(GaAs)}$, is determined by the conditions under which GaAs compound is thermodynamically

stable, which is given by the substitution of Eq. (2.13) into Eq. (2.14):

$$\mu_{GaAs(bulk)} - \mu_{Ga(bulk)} < \mu_{As(GaAs)} < \mu_{As(bulk)}. \quad (2.17)$$

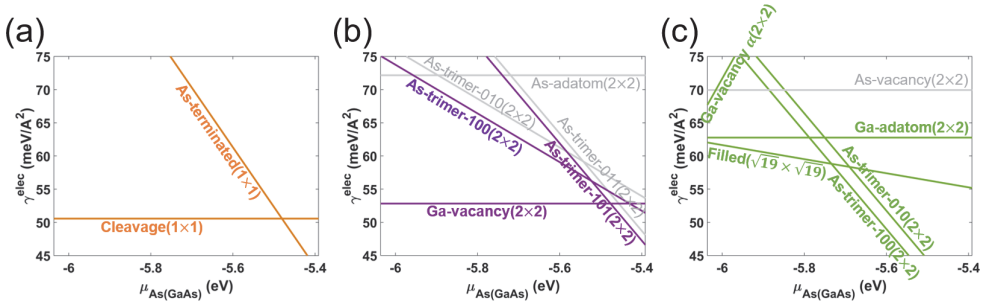

Figure 2.8 Calculated electronic surface energy of GaAs (a) (110), (b) (111)A, and (c) (111)B surfaces as a function of $\mu_{As(GaAs)}$. The stable reconstructions with low electronic surface energy are highlighted for each surface.

In real situation, the GaAs surface is in contact with a given As atmosphere, whose change in the thermodynamic potential is caused by the change in T and P_{As} as represented in Fig. 2.7. By assuming the chemical equilibrium between the surface and surrounding gas (Fig. 2.9), $\gamma^{elec}(\mu_{As(GaAs)})$ in Fig. 2.8 can be converted to $\gamma^{elec}(T, P_{As})$ as in Fig. 2.10. This dependency, originated from the chemical potential of reservoir and the stoichiometry imbalance of reconstruction, is called implicit T–P dependence [25]. It is notable that the conversion from $\mu_{As(GaAs)}$ dependence to T–P dependence makes it practical to directly compare the calculation data with the experimental observations.

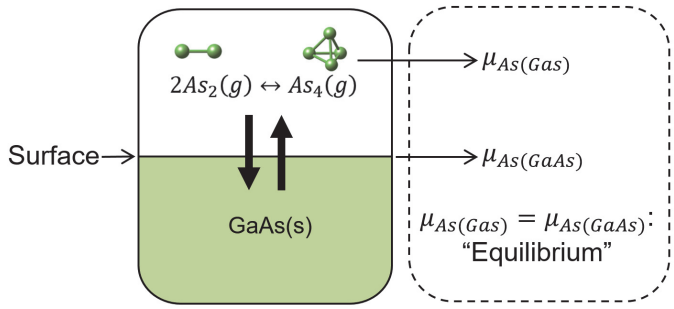

Figure 2.9 Schematic of equilibrium condition that the chemical potential of As in ZB-GaAs is equal to that of As in vapor phase. The As in vapor phase was considered to be a gas mixture consisting of As_2 and As_4 molecules in equilibrium.

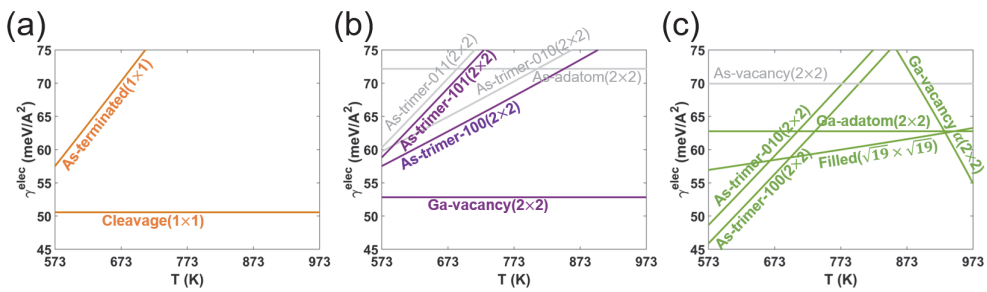

Figure 2.10 Electronic surface energy of GaAs (a) (110), (b) (111)A, and (c) (111)B surfaces as a function of T at fixed P_{As} of 3×10^{-9} atm.

2.3.4 Effects of surface vibration

The calculation explained so far was performed under the assumption that the contribution to the surface energy coming from surface vibration is negligible. However, the differences in the bonding geometries and stoichiometry of various surface reconstructions are non-trivial, which might induce the different T dependence of the various surface reconstructions. This dependency, originated from the vibrational entropy of surface atoms, is called explicit T dependence [25]. In fact, it has been reported that the vibrational entropy of the surface atoms plays a key role

in energetic calculation for some materials [26,27]. Therefore, effects of the surface vibration on surface energy must be treated carefully.

In surface vibration calculations, the surface atoms of reconstruction were considered to be coupled harmonic oscillators. These atoms were displaced from their equilibrium positions by finite distance (we confirmed that the displacements by 0.01 and 0.015 Å give the same phonon DOS), and the resulting forces were used to make Born-von Karman force constants and dynamical matrix on the corresponding surface BZ. The eigen-frequencies of surface phonon modes at 21×21 k-points, sampled at equal intervals on the 2-dimensional BZ, were inserted into Eq. (2.5) to evaluate the vibrational free energy of surface reconstructions (F_{surf}^{vib}). The surface phonon DOSs were plotted by smearing the frequencies by the Gaussian smearing method (σ=0.1). Similar to Eq. (2.16), the vibrational free energy difference between surface and bulk is given by:

$$\Delta\gamma^{vib} = \frac{\left(F_{surf}^{vib}\right) - N_{Ga}\left(F_{GaAs(bulk)}^{vib}\right) - (N_{As} - N_{Ga})\left(F_{As(GaAs)}^{vib}\right)}{A}, \quad (2.18)$$

where $\Delta\gamma^{vib}$ is the vibrational contribution to surface energy; and $F_{GaAs(bulk)}^{vib}$ and $F_{As(GaAs)}^{vib}$ are the vibrational free energies of ZB-GaAs and As in ZB-GaAs, respectively.

As an example, Fig. 2.11(a) shows the surface phonon DOSs of GaAs (100) β2(2×4) calculated by the finite displace method conducted for atoms at top several layers: from the topmost layer to the top four layers. The corresponding surface phonon DOSs and bulk phonon DOS in Fig. 2.3 were utilized to evaluate F_{surf}^{vib}, $F_{GaAs(bulk)}^{vib}$, and $F_{As(GaAs)}^{vib}$ in Eq. (2.18) using Eq. (2.5). Figure 2.11(b) shows the resulting vibrational contribution to surface energy and the vibrational surface

energy ($\Delta\gamma^{vib}$) is confirmed to be converged when the atoms at the top three layers or more layers are considered in the surface phonon calculation. This is because the bonding state and vibration of the atoms at deeper than the top three layers are almost identical to those of the atoms in bulk state as shown in the atomic structure in Fig. 2.11(a).

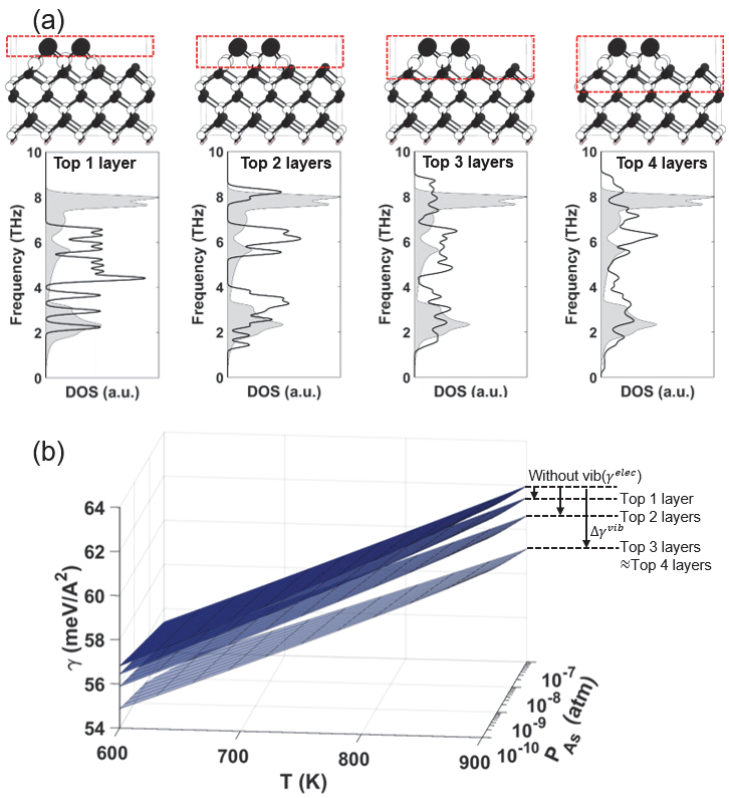

Figure 2.11 (a) Surface phonon DOS (black line) of the GaAs (100) β2(2×4) reconstruction obtained by displacement of the atoms at the uppermost layer, up to the 2nd layer, up to the 3rd layer, and up to the 4th layer from the uppermost layer, compared with the bulk phonon DOS of ZB-GaAs (shaded area). The range of layers where the displacement is allowed is denoted by dashed red box. (b) Surface energies contributed by the electronic and vibrational terms ($\gamma = \gamma^{elec} + \Delta\gamma^{vib}$) of GaAs (100) β2(2×4).

Therefore, in this dissertation, all of the surface phonons were obtained by finite displacement of the atoms at top three layers. Figure 2.12 shows the sum of the electronic surface energy (γ^{elec}) in Fig. 2.10 and the vibrational surface energy ($\Delta\gamma^{vib}$). Compared with Fig. 2.10, the surface energy is lowered by 5~10 meV/Å^2 by the vibrational contribution and the amount of the decrease is different for each reconstruction. This is because the surface phonon and its difference with the bulk phonon are various, caused by the different bonding state of each reconstruction. The corresponding surface phonon DOSs as well as atomic structures of the reconstructions will be explained at relevant point in this dissertation.

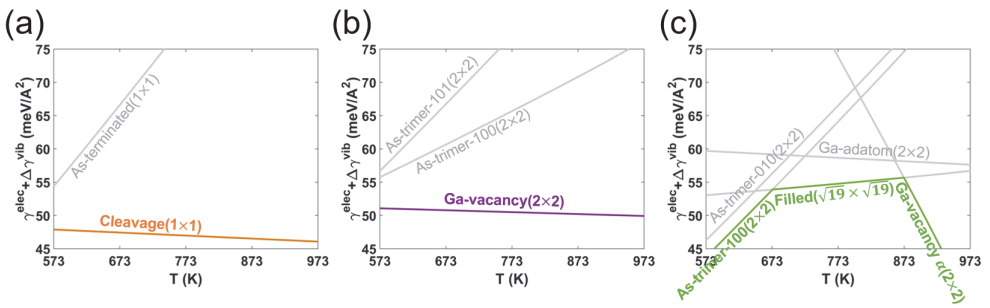

Figure 2.12 Calculated total surface energy of GaAs (a) (110), (b) (111)A, and (c) (111)B surfaces as a function of T at fixed P_{As} of 3×10^{-9} atm. The lowest surface energy line is highlighted along the most stable reconstructions for each surface.

2.4. Equilibrium crystal shape (ECS)

2.4.1 Wulff construction

On the basis of the anisotropic surface energy, the faceted morphology is generally formed as the consequence of minimizing the sum of the exposed surface energy.

This energy-minimized shape in homogeneous environments is referred to as ECS or Wulff shape and determined by the Wulff construction theory [28]. The Wulff construction rule is schematically shown in Fig. 2.13. The generation of the Wulff shape starts with γ-plot: a set of radial vector whose distance from a fixed point (called Wulff point) is proportional to the corresponding surface energy, $\gamma_{\hat{n}_i}\hat{n}_i$. Then, planes perpendicular to the radial vectors are drawn for each orientation $\hat{n}_i$. This planes divide space and the convex envelope of this plot corresponds to the Wulff shape. There are several freely available programs to display the Wulff shape for a given set of surface energy: Wulffman [29], Wulffmaker [30], and SOWOS [31].

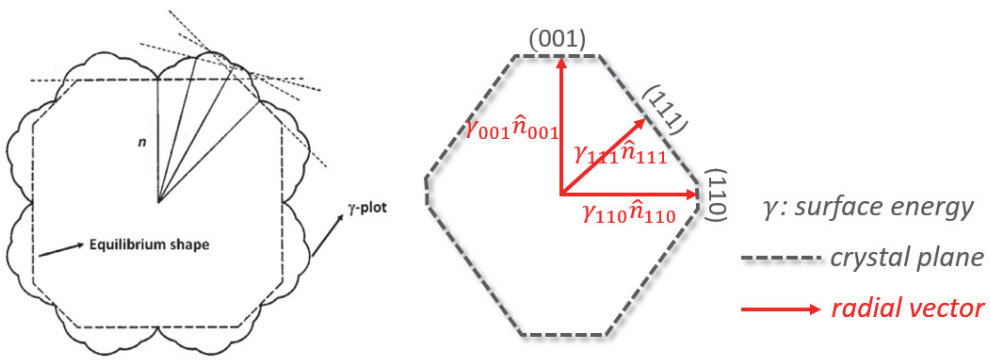

Figure 2.13 Schematic of Wulff construction.

2.5. Anisotropic growth kinetics

2.5.1 Direction dependent nucleation

When the equilibrium condition is not reached, the anisotropic growth rate becomes a key factor that determines the crystal morphology and the surface with slower growth rate tends to be more exposed. The growth rate along each crystallographic direction can be inferred by nucleation rate:

$$\dot{N}_{n|Surf}(T,P) = \dot{C}(Surf,T,P) \cdot \exp\left(-\frac{\Delta G^*_{sn}(Surf,T,P)}{k_B T}\right), \quad (2.19)$$

where $\dot{N}_{n|Surf}(T,P)$ is nucleation rate on a given surface orientation; $\dot{C}(Surf,T,P)$ is pre-exponential factor which is related to the rate of source supply; and $\Delta G^*_{sn}(Surf,T,P)$ is the nucleation barrier. As denoted in Eq. (2.19), all the terms are affected by the surface orientation and T–P conditions. For example, the rate of source supply on each surface is determined by the combination of vapor phase adsorption and diffusion on the surface.

2.5.2 Adsorption and desorption

In the vapor-phase growth techniques, the supplied vapor sources are adsorbed to surface and desorbed from the surface repeatedly before the incorporation of sources into nucleus. Between the competitive adsorption and desorption, an element might prefers to be adsorbed onto the surface if the chemical potential of the adsorbed state is lower than that of vapor phase. Figure 2.14 schematically illustrates the criteria for whether the adsorption or desorption is more preferred.

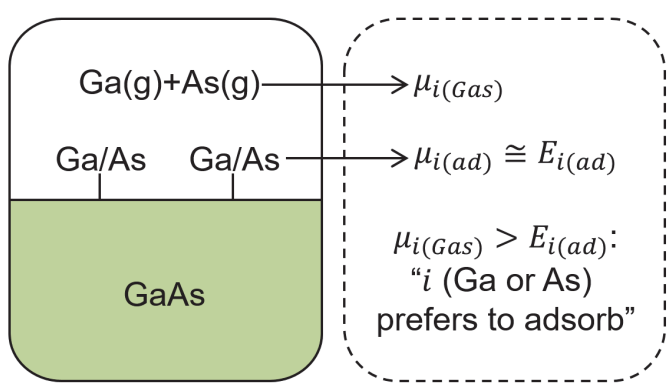

Figure 2.14 Schematic to determine the adsorption-desorption boundary for Ga or As atom. If the chemical potential of the adsorbed state is lower than that of vapor phase, the adsorption might be favorable to occur.

2.5.3 Gibbs free energy for nucleation

Figure 2.15 depicts the situation that a nucleus is formed on an arbitrary crystal surface. The change in Gibbs free energy by the formation of the nucleus is written as:

$$\Delta G_{sn} = V\Delta\mu_{sn} + Ph\gamma_{sn(side)} + A(\gamma_{cn(top)} + \gamma_{sn(top)} - \gamma_{sc(top)}), \quad (2.20)$$

where V, P, h, and A indicate volume, perimeter length, height, and top surface area of the nucleus, respectively; $\Delta\mu_{sn}$ is the change in chemical potential per volume by the incorporation of sources into nucleus; $\gamma_{sn(side)}$ is the side surface energy between source and nucleus (sn); $\gamma_{cn(top)}$ and $\gamma_{sn(top)}$ are the top interface (surface) energy between crystal and nucleus (cn), and between source and nucleus (sn), respectively, which are generated by the formation of the nucleus; and $\gamma_{sc(top)}$ is the top surface energy between source and crystal (sc), which disappears by the nucleation. Note that the nucleus geometry in Fig. 2.15 is just schematic illustration and the shape of the nucleus may be different for each surface direction.

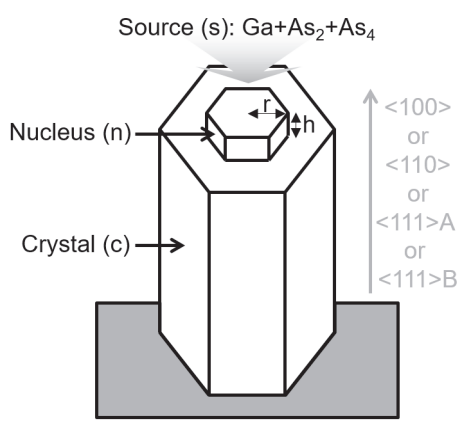

Figure 2.15 Schematic of the nucleus (n) formation by incorporation of the sources (s) on crystal (c) surface growing along arbitrary directions.

2.6. Bibliography

[1] D. Sholl and J. A. Steckel, *Density Functional Theory: A Practical Introduction*, John Wiley & Sons, 2011.

[2] F. Giustino, *Materials Modelling Using Density Functional Theory: Properties and Predictions*, Oxford University Press, 2014.

[3] W. Kohn and L. J. Sham, Self-Consistent Equations Including Exchange and Correlation Effects, *Phys. Rev.*, **140**, A1133, (1965).

[4] P. Hohenberg and W. Kohn, Inhomogeneous Electron Gas, *Phys. Rev.*, **136**, B864, (1964).

[5] L. Schimka, J. Harl, A. Stroppa, A. Grüneis, M. Marsman, F. Mittendorfer and G. Kresse, Accurate Surface and Adsorption Energies from Many-Body Perturbation Theory, *Nat. Mater.*, **9**, 741-744, (2010).

[6] D. M. Ceperley and B. Alder, Ground State of the Electron Gas by a Stochastic Method, *Phys. Rev. Lett.*, **45**, 566, (1980).

[7] J. P. Perdew and A. Zunger, Self-Interaction Correction to Density-Functional Approximations for Many-Electron Systems, *Phys. Rev. B*, **23**, 5048, (1981).

[8] P. E. Blöchl, Projector Augmented-Wave Method, *Phys. Rev. B*, **50**, 17953, (1994).

[9] G. Kresse and D. Joubert, From Ultrasoft Pseudopotentials to the Projector Augmented-Wave Method, *Phys. Rev. B*, **59**, 1758, (1999).

[10] G. Kresse and J. Hafner, Ab Initio Molecular Dynamics for Liquid Metals, *Phys. Rev. B*, **47**, 558, (1993).

[11] G. Kresse and J. Hafner, Ab Initio Molecular-Dynamics Simulation of the Liquid-Metal–Amorphous-Semiconductor Transition in Germanium, *Phys. Rev. B*, **49**, 14251, (1994).

[12] G. Kresse and J. Furthmüller, Efficiency of Ab-Initio Total Energy Calculations for Metals and Semiconductors Using a Plane-Wave Basis Set, *Comput. Mater. Sci.*, **6**, 15-50, (1996).

[13] G. Kresse and J. Furthmüller, Efficient Iterative Schemes for Ab Initio Total-Energy Calculations Using a Plane-Wave Basis Set, *Phys. Rev. B*, **54**, 11169, (1996).

[14] J. Neugebauer and M. Scheffler, Adsorbate-Substrate and Adsorbate-Adsorbate Interactions of Na and K Adlayers on Al (111), *Phys. Rev. B*, **46**, 16067, (1992).

[15] T. Ito, Simple Criterion for Wurtzite-Zinc-Blende Polytypism in Semiconductors, *Jpn. J. Appl. Phys.*, **37**, L1217, (1998).

[16] D. Woolf, D. Westwood and R. Williams, The Homoepitaxial Growth of GaAs (111)A and (111)B by Molecular Beam Epitaxy: An Investigation of the Temperature-Dependent Surface Reconstructions and Bulk Electrical Conductivity Transitions, *Semicond. Sci. Technol.*, **8**, 1075, (1993).

[17] M. de la Mata, R. R. Zamani, S. Martí-Sánchez, M. Eickhoff, Q. Xiong, A. Fontcuberta i Morral, P. Caroff and J. Arbiol, The Role of Polarity in Non-Planar Semiconductor Nanostructures, *Nano Lett.*, **19**, 3396-3408, (2019).

[18] N. Moll, A. Kley, E. Pehlke and M. Scheffler, GaAs Equilibrium Crystal Shape from First Principles, *Phys. Rev. B*, **54**, 8844, (1996).

[19] S. Zhang and S.-H. Wei, Surface Energy and the Common Dangling Bond Rule for Semiconductors, *Phys. Rev. Lett.*, **92**, 086102, (2004).

[20] K. Reuter, C. Stampf and M. Scheffler, in *Handbook of Materials Modeling*, Springer, 2005, pp. 149-194.

[21] J. Rogal and K. Reuter, *Ab Initio* Atomistic Thermodynamics for Surfaces: A Primer, in *Experiment, Modeling and Simulation of Gas-Surface Interactions for Reactive Flows in Flghts*, RTO-AVT-VKI Lecture Series, 6-10 fevrier, 2006, pp. 2-1 – 2-18.

[22] A. Togo and I. Tanaka, First Principles Phonon Calculations in Materials Science, *Scr. Mater.*, **108**, 1-5, (2015).

[23] M. Chase, NIST-JANAF Thermochemical Tables 4th Ed, *J. Phys. Chem. Ref. Data*, 1529-1564, (1998).

[24] D. A. McQuarrie, *Statistical Mechanics*, University Science Books, California, 2000.

[25] M. Valtiner, M. Todorova, G. Grundmeier and J. Neugebauer, Temperature Stabilized Surface Reconstructions at Polar ZnO (0001), *Phys. Rev. Lett.*, **103**, 065502, (2009).

[26] S. Wippermann and W. G. Schmidt, Entropy Explains Metal-Insulator Transition of the Si (111)-In Nanowire Array, *Phys. Rev. Lett.*, **105**, 126102, (2010).

[27] P. Kempisty and Y. Kangawa, Evolution of the Free Energy of the GaN (0001) Surface Based on First-Principles Phonon Calculations, *Phys. Rev. B*, **100**, 085304, (2019).

[28] G. Wulff, *Z. Kristallogr.*, **34**, 449-530, (1901).

[29] A. R. Roosen, R. P. McCormack and W. C. Carter, Wulffman: A Tool for the Calculation and Display of Crystal Shapes, *Comput. Mater. Sci.*, **11**, 16-26, (1998).

[30] R. V. Zucker, D. Chatain, U. Dahmen, S. Hagège and W. C. Carter, New Software Tools for the Calculation and Display of Isolated and Attached Interfacial-Energy Minimizing Particle Shapes, *J. Mater. Sci.*, **47**, 8290-8302, (2012).

[31] D. Scopece, Sowos: An Open-Source Program for the Three-Dimensional Wulff Construction, *J. Appl. Crystallogr.*, **46**, 811-816, (2013).

Chapter 3. Surface reconstructions of GaAs (100)

3.1. Introduction

The atomic structure of the compound semiconductor surface, especially after reconstruction, has important effects on the material growth. While there are numerous experimental techniques to probe the surface structures, surface energy and reconstruction have been difficult to be identified, and hence further theoretical studies on surface reconstruction are necessary to promote the clear understanding of the development of such subtle surface structures. In this chapter, the T–P dependent variation in surface reconstruction of GaAs (100) will be clarified based on DFT calculation. It should be noted that the surface energy and existence probability of various reconstructions are predicted as a function of T and P, not as a function of the chemical potential [1]. This highly facilitates the direct comparison with the experiments. By taking into account the effects of vibrational and configurational entropy, which has been commonly neglected in conventional *ab initio* calculations, the improved prediction can be achieved showing notable agreement with the previous experimental observations.

3.1.1. Dependence on temperature and pressure conditions

Surface reconstruction occurs to minimize the surface energy by altering its bonding configurations of a specific crystallographic plane. In particular, III-V semiconductors show inherently complicated surface reconstructions which are variable depending on T–P conditions. Previous experimental studies on GaAs (100) observed the reversible changes in the dominant reconstruction using reflection high-

energy electron diffraction (RHEED) and scanning tunneling microscopy (STM): c(4×4) ⇆ (2×4) ⇆ (4×2), where the right-hand directions correspond to an increase in T or a decrease in P [2,3].

3.1.2. Candidate structures of reconstructions

In order to find the stable reconstructions and corresponding surface energies of GaAs (100), various reconstructions reported in previous studies [4-7] were referred. Figure 3.1 shows the top view of the considered reconstructions with primitive (1×1) as-cleaved surface. In this figure, different periodicity is distinguished by different shaded colors. For the c(4×4) reconstructions, not only the homodimers consisting of the six As atoms, c(4×4) As6, but also the heterodimer configurations were considered following the previous studies [8-10]. All the possible heterodimer configurations were constructed by replacing one to six As atoms at the top layer with Ga atoms, but only the structures having the lowest surface energy for a given surface composition are displayed in Fig. 3.1.

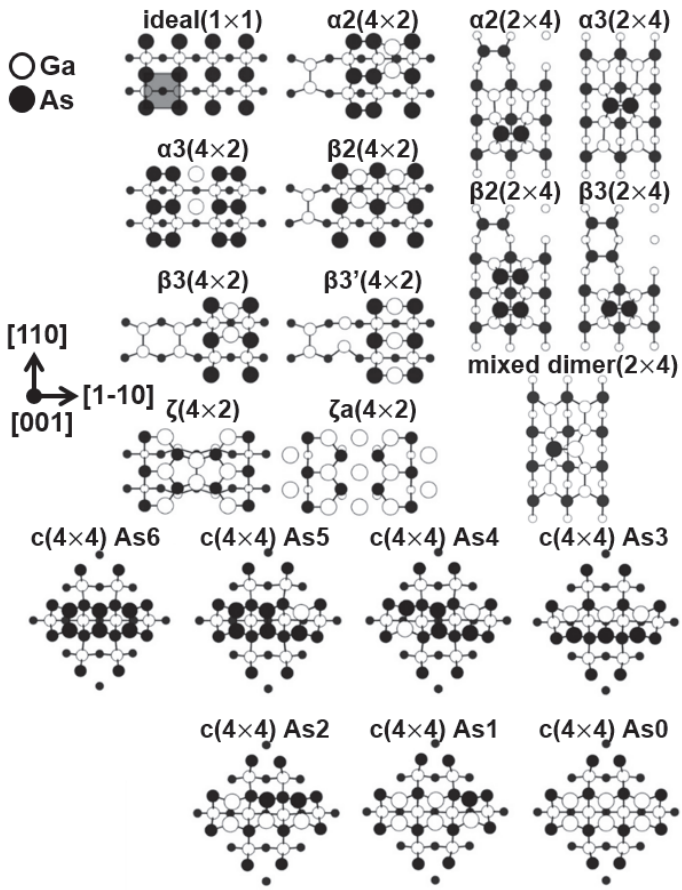

Figure 3.1 Top view of the atomic structures of GaAs (100) reconstructions. All the surface areas correspond to the surface unit cell, except the ideal(1×1), whose surface unit cell sizes are indicated by the dark gray square. The largest circles indicate the atoms at the topmost layer.

3.2. Surface phase diagram

3.2.1. Electronic surface energy

The electronic surface energy (γ^{elec}) of each reconstruction in Fig. 3.1 was calculated using the slab method described in section 2.2.1 and Eq. (2.13)-(2.16) in

section 2.3.3. The results are shown in Fig. 3.2(a) in which the stable reconstructions with low surface energy are highlighted by several colors. It should be noted that the range of x-axis, $\mu_{As(GaAs)}$, is limited by Eq. (2.17) and the slope of each surface energy line is proportional to the excess number of Ga atoms compared to As atoms in the structure, as presented in Eq. (2.16). Therefore, the fact that the slope of the most stable reconstruction changes from positive to negative signs as $\mu_{As(GaAs)}$ increases shows a consensus with the general conjecture that the reconstruction with more excess As atoms is more stable as $\mu_{As(GaAs)}$ increases. Under the Ga-rich condition (*i.e.*, low $\mu_{As(GaAs)}$ region), ζ(4×2) with a positive slope is identified as the reconstruction with the lowest surface energy. On the other hand, under the As-rich condition (*i.e.*, high $\mu_{As(GaAs)}$ region), c(4×4) As6 with a negative slope is the most stable. The reconstruction of β2(2×4) becomes stable in the middle range of $\mu_{As(GaAs)}$.

In order to make a T–P surface phase diagram of the GaAs (100), $\mu_{As(GaAs)}$ should be converted to a function of T and P, which is certainly achievable by the assumption of the chemical equilibrium between the surface and surrounding gas, $\mu_{As(GaAs)} = \mu_{As(Gas)}$, as depicted in Fig. 2.9. Accordingly, $\gamma^{elec}(\mu_{As(GaAs)})$ in Fig. 3.2(a) was converted to $\gamma^{elec}(T, P_{As})$ as shown in Fig. 3.2(b) using the method described in section 2.3.3 and the evaluated value of $\mu_{As(Gas)}(T, P_{As})$ in section 2.3.2. It is worth emphasizing that the conditions of high T and low P_{As} correspond to the low chemical potential of As. Therefore, the changes in stable reconstructions with increasing As chemical potential correspond to those with decreasing T and increasing P_{As}.

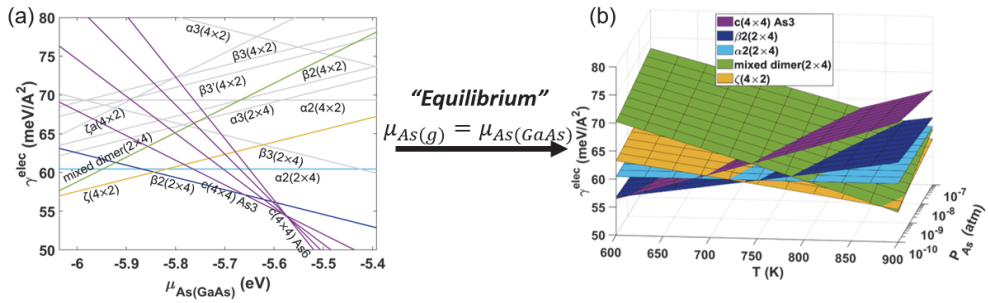

Figure 3.2 (a) Electronic surface energy of GaAs (100) reconstructions as a function of chemical potential of As in ZB-GaAs. (b) The surface energy converted to the function of T and P.

3.2.2. Vibrational entropy contribution

In addition to the electronic surface energy, the difference in vibrational free energy between surface and bulk was calculated using the method described in section 2.3.4. Figure 3.3(a) shows the evaluated total surface energy including both the electronic and vibrational contributions, $\gamma = \gamma^{elec} + \Delta\gamma^{vib}$. Compared to Fig. 3.2(b), the surface energies of the reconstructions were entirely lowered by different amounts, which is caused by the different bonding state of each reconstruction. From this figure, the most stable reconstruction under a given T–P condition can be identified and Fig. 3.3(b) shows the resulting surface phase diagram of GaAs (100). The experimental conditions where the reconstruction transitions from c(4×4) to (2×4) and from (2×4) to (4×2) occurred are indicated by the triangular and circular marks, respectively. The closeness between the experimental points and theoretical transition lines shows the validity of our calculations.

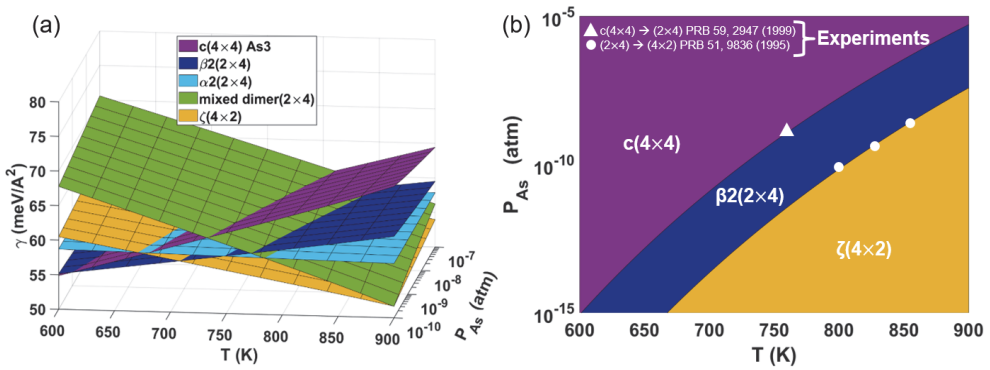

Figure 3.3 (a) Total surface energy ($\gamma = \gamma^{elec} + \Delta\gamma^{vib}$) of GaAs (100) reconstructions as a function of T and P, and (b) surface phase diagram of GaAs (100). The experimental T–P conditions where reconstruction transitions from c(4×4) to (2×4) and from (2×4) to (4×2) were observed are indicated by the triangular and circular marks, respectively, for comparison.

3.2.3. Configurational entropy contribution

Around transition T–P conditions in which there is little energy difference between two or more surface reconstructions, the coexistence of multiple reconstructions was observed: mixture of c(4×4) with various types of dimers under low T condition [3,11], that of c(4×4) with (2×4) [3], and that of (2×4) with (4×2) [2]. The observed mixed or coexisting phases are originated from the configurational entropy [12,13] and reflect the fact that a real situation is not the ground state but ensemble of possible configurations with statistical probability. At a given T and P, the probability of filling area (A) with reconstruction i (c_i) can be predicted by the partition function Z [12,13]:

$$Z = \sum_i Z_i = \sum_i g_i \exp\left(-\frac{\gamma_i(T,P)A}{k_B T}\right), \quad (3.1)$$

$$g_i = \frac{\sigma_{(1\times1)}}{\sigma_{(n\times m)}} n_i m_i, \quad (3.2)$$

$$c_i = \frac{Z_i}{Z} \; where \; i \in \{reconstructions\}, \tag{3.3}$$

where γ_i is the surface energy of reconstruction i; g_i is the degeneracy factor related to the surface symmetry; n_i and m_i indicate cell sizes of reconstruction i(n×m); and $\sigma_{(n\times m)}$ is the number of symmetry operation of reconstruction i(n×m) as summarized in Table 3.1.

The values of γ_i in Eq. (3.1) were already calculated as a function of T and P, and thus it was possible to predict the T–P dependent c_i. Figure 3.4(a) shows the probability obtained from the electronic surface energy (γ^{elec}) of GaAs (100) as a function of T at a fixed P_{As} of 4×10^{-9} atm. On the other hand, Fig. 3.4(b) shows the result from the total surface energy ($\gamma = \gamma^{elec} + \Delta\gamma^{vib}$). As mentioned above, various configurations of homodimer and heterodimers exist in c(4×4) symmetry. The total sum of the probability of all c(4×4) configurations is denoted as 'c(4×4) all' in Fig. 3.4. The separated probability contributions from each c(4×4) configuration are represented in the lower panel of Fig. 3.4. These clearly demonstrate that the c(4×4) heterodimers enhance the existence probability of c(4×4) at low T region and show the transition of the dominant surface structures: c(4×4) with various configurations → mixture of c(4×4) with (2×4) → (2×4) → mixture of (2×4) with (4×2) → (4×2) as T increases. In the case that the surface vibration effects were considered, the transition T where the existence probability of two different reconstructions becomes similar (~ 0.5) is predicted to be 760–790 K for the transition from c(4×4) to (2×4) and ~850 K for the transition from (2×4) to (4×2), respectively. The overall calculations show remarkable agreement with the previous experimental observations carried out under common MBE condition (~4×10^{-9} atm): coexistence of c(4×4) with various types of dimers at T lower than 760 K [3,11], that

of c(4×4) with (2×4) at around 760 K [3], and that of (2×4) with (4×2) at around 850 K [2].

Table 3.1 Two-dimensional symmetry group (2SG), the number of symmetry operations ($\sigma_{(n\times m)}$), and degeneracy factor (g_i) for the various reconstructions of GaAs (100). For the c(4×4) heterodimers, the configuration having the lowest surface energy at each surface composition is underlined and represented in Fig. 3.1.

Reconstruction	2SG	σ	$\frac{g}{\sigma_{(1\times1)}}$	Reconstruction	2SG	σ	$\frac{g}{\sigma_{(1\times1)}}$
α2(4×2)	p1	1	8	ζa(2×4)	pmm	4	2
α3(4×2)	pmm	4	2	α2(2×4)	p1	1	8
β2(4×2)	pm	2	4	α3(2×4)	pmm	4	2
β3(4×2)	pm	2	4	β2(2×4)	pm	2	4
β3'(4×2)	p1	1	8	β3(2×4)	pm	2	4
ζ(4×2)	pmm	4	2	mixed dimer(2×4)	pm	2	4
c(4×4) As5 (I)	cmm	8	2	c(4×4) As3 (IV)	p1	2	8
c(4×4) As5 (II)	p1	2	8	c(4×4) As3 (V)	p1	2	8
c(4×4) As5 (II)	cm	4	4	c(4×4) As3 (VI)	p1	2	8
<u>c(4×4) As4 (I)</u>	p2	4	4	c(4×4) As2 (I)	p2	4	4
c(4×4) As4 (II)	p1	2	8	c(4×4) As2 (II)	p1	2	8
c(4×4) As4 (III)	cm	4	4	c(4×4) As2 (III)	cm	4	4
c(4×4) As4 (IV)	p1	2	8	<u>c(4×4) As2 (IV)</u>	p1	2	8
c(4×4) As4 (V)	cm	4	4	c(4×4) As2 (V)	cm	4	4
c(4×4) As4 (VI)	cmm	8	2	c(4×4) As2 (VI)	cmm	8	2
<u>c(4×4) As3 (I)</u>	cm	4	4	<u>c(4×4) As1 (I)</u>	p1	2	8
c(4×4) As3 (II)	p1	2	8	c(4×4) As1 (II)	cm	4	4
c(4×4) As3 (III)	cm	4	4	<u>c(4×4) As0</u>	cmm	8	2

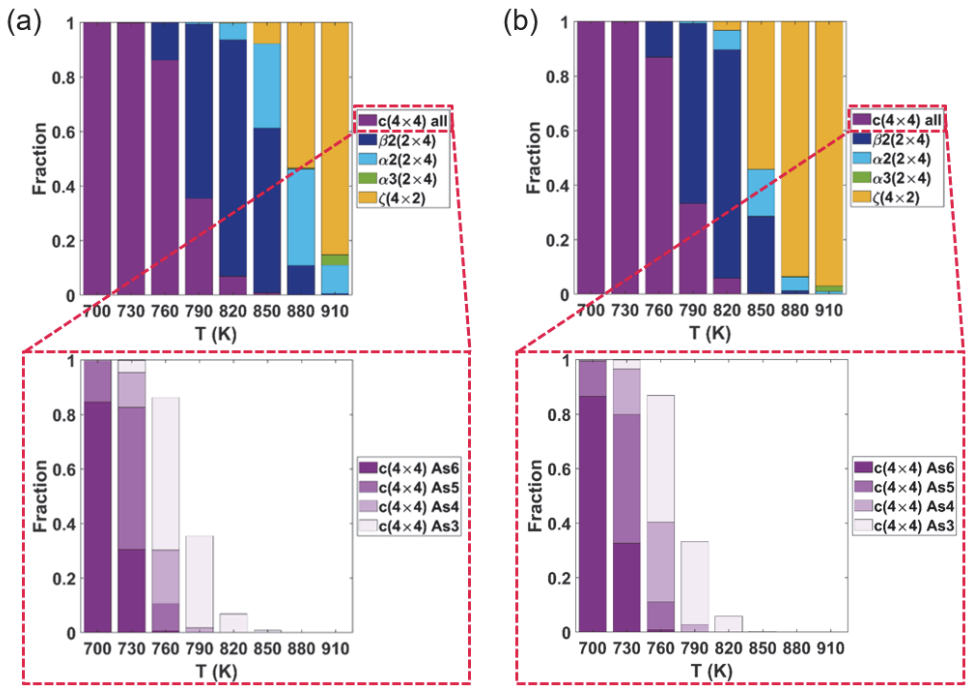

Figure 3.4 Existence probability of each reconstruction evaluated from (a) electronic surface energy (γ^{elec}) and (b) total surface energy ($\gamma = \gamma^{elec} + \Delta\gamma^{vib}$) of GaAs (100) reconstructions as a function of T at a fixed P_{As} of 4×10^{-9} atm.

3.3 Conclusion

Starting from conventional surface energy calculation as a function of chemical potential, the surface energy was converted to functions of T and P_{As} by the assumption that the GaAs surface is in equilibrium with the surrounding gas mixture consisting of As_2 and As_4 molecules. Then, vibrational surface energy was evaluated by the difference in vibrational free energy between surface and bulk and additionally included to obtain total surface energy ($\gamma = \gamma^{elec} + \Delta\gamma^{vib}$). This total surface energy of GaAs (100) reconstructions was used to evaluate the existence probability of each reconstruction by consideration of configurational entropy. By

the consideration of both vibrational and configurational entropy within the *ab initio* thermodynamics, the coexistence and the probability change of the various reconstructions were successfully predicted under arbitrarily given T–P conditions. This kind of prediction enabled us to directly compare the calculations with experiments, and was well matched with the previous experimental observations.

3.4 Bibliography

[1] I. W. Yeu, J. Park, G. Han, C. S. Hwang and J.-H. Choi, Surface Reconstruction of InAs (001) Depending on the Pressure and Temperature Examined by Density Functional Thermodynamics, *Sci. Rep.*, **7**, 10691, (2017).

[2] H. Yamaguchi and Y. Horikoshi, Surface Structure Transitions on InAs and GaAs (001) Surfaces, *Phys. Rev. B*, **51**, 9836, (1995).

[3] G. Bell, J. Belk, C. McConville and T. Jones, Species Intermixing and Phase Transitions on the Reconstructed (001) Surfaces of GaAs and InAs, *Phys. Rev. B*, **59**, 2947, (1999).

[4] N. Moll, A. Kley, E. Pehlke and M. Scheffler, GaAs Equilibrium Crystal Shape from First Principles, *Phys. Rev. B*, **54**, 8844, (1996).

[5] W. Schmidt, III-V Compound Semiconductor (001) Surfaces, *Appl. Phys. A*, **75**, 89-99, (2002).

[6] J. Lång, M. Punkkinen, P. Laukkanen, M. Kuzmin, V. Tuominen, M. Pessa, M. Guina, I. Väyrynen, K. Kokko and B. Johansson, Ab Initio and Scanning Tunneling Microscopy Study of an Indium-Terminated GaAs (100) Surface:

an Indium-Induced Surface Reconstruction Change in the c(8×2) Structure, *Phys. Rev. B*, **81**, 245305, (2010).

[7] C. Ratsch, W. Barvosa-Carter, F. Grosse, J. Owen and J. Zinck, Surface Reconstructions for InAs (001) Studied with Density-Functional Theory and STM, *Phys. Rev. B*, **62**, R7719, (2000).

[8] A. Ohtake, J. Nakamura, S. Tsukamoto, N. Koguchi and A. Natori, New Structure Model for the GaAs (001)−c(4×4) Surface, *Phys. Rev. Lett.*, **89**, 206102, (2002).

[9] A. Ohtake and N. Koguchi, Two Types of Structures for the GaAs (001)-c(4×4) Surface, *Appl. Phys. Lett.*, **83**, 5193-5195, (2003).

[10] A. Ohtake, P. Kocán, J. Nakamura, A. Natori and N. Koguchi, Kinetics in Surface Reconstructions on GaAs (001), *Phys. Rev. Lett.*, **92**, 236105, (2004).

[11] A. Avery, D. Homes, J. Sudijono, T. Jones and B. Joyce, The As-Terminated Reconstructions Formed by GaAs (001): A Scanning Tunnelling Microscopy Study of the (2×4) and c(4×4) Surfaces, *Surf. Sci.*, **323**, 91-101, (1995).

[12] E. Penev, P. Kratzer and M. Scheffler, Atomic Structure of the GaAs (001)−c(4×4) Surface: First-Principles Evidence for Diversity of Heterodimer Motifs, *Phys. Rev. Lett.*, **93**, 146102, (2004).

[13] O. Romanyuk, F. Grosse, A. Proessdorf, W. Braun and H. Riechert, Stabilization of Semiconductor Surface Reconstructions by Configurational Entropy, *Phys. Rev. B*, **82**, 125315, (2010).

Chapter 4. Equilibrium crystal shapes of GaAs

4.1. Introduction

Depending on substrate orientation and T–P conditions of vapor-phase growth techniques, such as SA-MBE and SA-MOVPE, the changes in crystal morphology occur [1-3]. Many experiments have been carried out to tailor the crystal morphology by controlling the growth conditions. However, the control of the morphology has been attempted by heuristic approaches. To obtain III-V crystals in highly controlled manner, the interrelationship between the growth conditions and the crystal morphology has to be theoretically elucidated. Despite the crucial role of the surface energy and its anisotropy, a way of theoretically predicting the T–P dependent surface energy and crystal shape has yet to be developed [4-8]. This is because the conventional DFT calculations give us surface energy and following ECS as a function of chemical potential [9-11]. In this chapter, the changes in surface energy of several low-index surfaces and ECS were predicted as a function of the practical experimental variables of T and P by extending the method applied to GaAs (100) in chapter 3 to other surfaces. It enabled us to promote direct comparison of the calculated ECSs with experimentally grown shapes. In addition, a new (111)B reconstruction which is stabilized at high T by high entropy was proposed. The energetic and dynamical stability of this reconstruction were thoroughly confirmed and a correspondence between the calculated ECSs and experimental shapes was achieved only when both the new reconstruction and vibrational surface energy were considered [12]. The correspondence between ECSs and experimental shapes implies that the previous growth experiments were performed under conditions close

to equilibrium. It also emphasizes that the inclusion of the surface vibration effects is crucial for the materials exposing various surfaces with different bonding states, and that the suggested new (111)B reconstruction is highly probable to exist.

4.1.1. Dependence on temperature and pressure conditions

When epitaxial growth of GaAs is conducted on GaAs or Si (100) substrate by the SA methods, the faceted crystal shapes are formed, which are mainly composed of several low-index surfaces: (100), (110), (111)A, and (111)B. The portion of each surface in the faceted morphology depends on T–P conditions. Experimentally, the crystal shapes with high fraction of (111)B facets were observed under low T conditions, while the symmetric morphologies showing similar surface area of (111)A and (111)B were formed under high T conditions of SA-MOVPE [1,2]. The main discrepancy between previous theoretical predictions on the GaAs ECS and experimental shapes is the existence of (111)B facets at high T. Under As-rich conditions corresponding to low T and high P, all the four considered surfaces were calculated to be exposed in the theoretical ECSs [9] in agreement with the experimental observations [1]. However, the previous theoretical works reported the absence of the (111)B facets under Ga-rich conditions [9], showing inconsistency with the experimental shapes exposing similar area of (111)A and (111)B facets.

4.1.2. Candidate structures of reconstructions

The discrepancy between the calculated ECSs and experimental shapes was previously attributed to the lack of computational capability to get surface energy of ($\sqrt{19}\times\sqrt{19}$) reconstruction of the (111)B surface, which was observed to be stable

under high T conditions [13-15]. Calculation for such large size reconstruction was beyond the computational capability at the time that such theoretical works were conducted. In this study, all of the recently proposed structures, which were not considered in the previous works, were calculated including (113)A and (113)B as well as (111)B ($\sqrt{19}\times\sqrt{19}$) reconstructions. Figure 4.1 shows the atomic structures of all the considered reconstructions, which were generated by referring to the previous reports for each surface: (100) [9,16,17], (110) [9], (111)A [9,18], (111)B [9,18,19], (113)A [20-22], and (113)B [20,21,23].

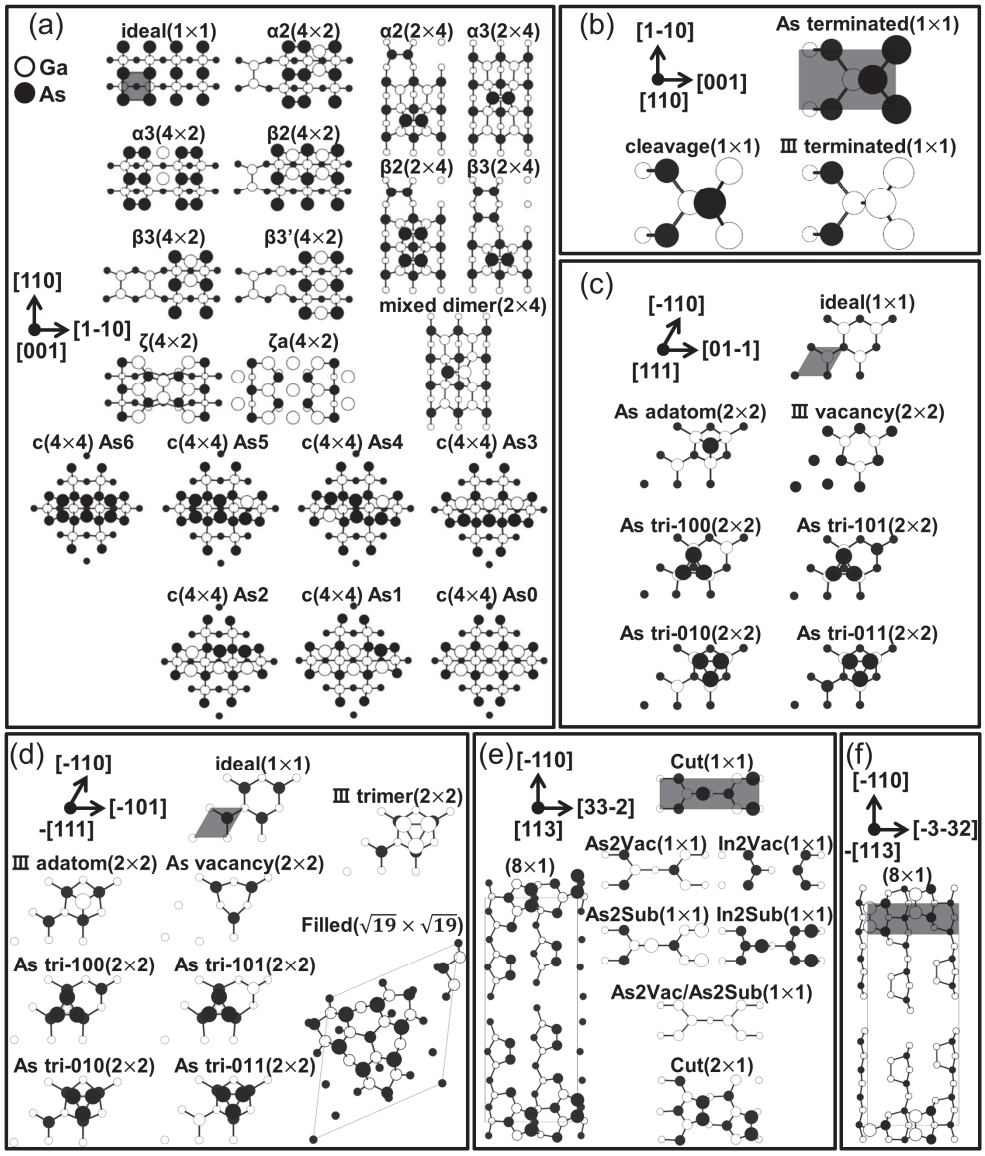

Figure 4.1 Top view of the atomic structures of GaAs (a) (100), (b) (110), (c) (111)A, (d) (111)B, (e) (113)A, and (f) (113)B reconstructions. All the surface areas correspond to the surface unit cell, except the ideal(1×1), whose surface unit cell sizes are indicated by shaded gray areas. The largest circles indicate the atoms at the topmost layer.

4.2. T–P variation of crystal shape

4.2.1. Equilibrium crystal shape by electronic surface energy

The electronic surface energies (γ^{elec}) of the reconstructions in Fig. 4.1 are shown in Fig. 4.2 as a function of As chemical potential ($\mu_{As(GaAs)}$). As the chemical potential changes, the surface reconstruction of each surface orientation will be changed to the one with the minimum surface energy. Figure 4.3 shows the corresponding minimum surface energies connecting the most stable reconstruction for each surface. In this figure, the point where the slope of the line changes corresponds to the transition point of the reconstruction. In addition, the experimentally relevant growth conditions are indicated as the shaded gray area and a T–P condition (973 K, 10^{-3} atm), the highest value of As chemical potential among the experimental conditions, is denoted [1,2,4]. It should be noted that the typical experimental conditions of GaAs growth are within Ga-rich conditions.

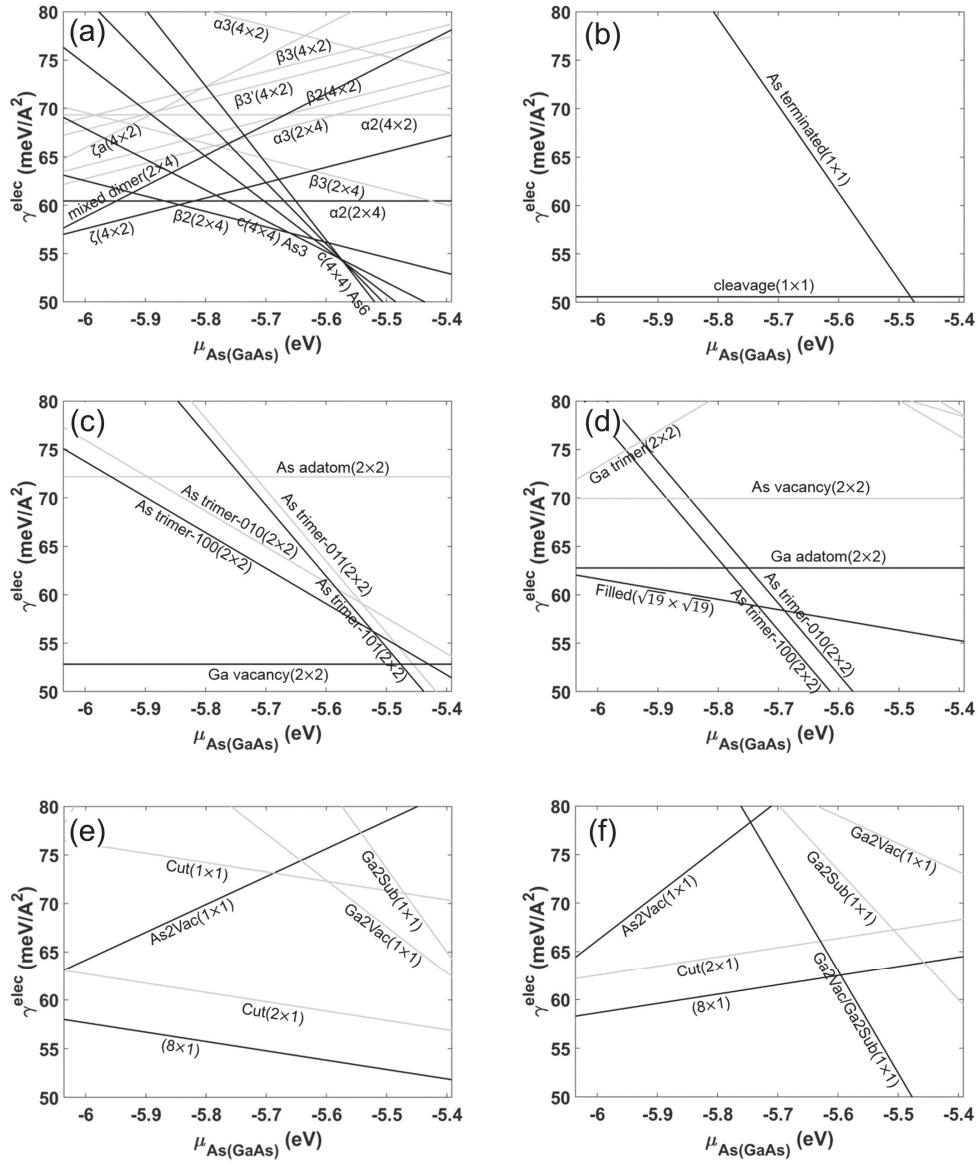

Figure 4.2 Calculated electronic surface energies of GaAs (a) (100), (b) (110), (c) (111)A, (d) (111)B, (e) (113)A, and (f) (113)B. For each surface, the reconstructions with low surface energy are highlighted by bold lines.

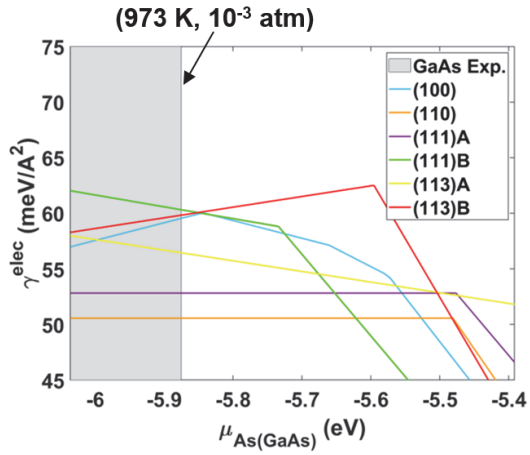

Figure 4.3 Calculated minimum surface energies of GaAs for the several low-index surfaces. The shaded area corresponds to the experimentally relevant growth conditions.

Such as the conversion from As chemical potential to T–P we did for GaAs (100) in chapter 3 by the assumption of the chemical equilibrium between the surface and surrounding gas ($\mu_{As(GaAs)} = \mu_{As(Gas)}$), $\gamma^{elec}(\mu_{As(GaAs)})$ in Fig. 4.3 was also converted to $\gamma^{elec}(T, P_{As})$ using the method described in section 2.3.3 and the evaluated value of $\mu_{As(Gas)}(T, P_{As})$ in section 2.3.2. From the calculated $\gamma^{elec}(T, P_{As})$ for each surface orientation, the variation in ECS as a function of T and P_{As} was obtained through Wulff construction theory [24]. The simple explanation about the theory is described in section 2.4.1 and we used Wulffman among the available Wulff construction programs (Wulffman [25], Wulffmaker [26], and SOWOS [27]) to display the Wulff shape (*i.e.*, ECS).

Figure 4.4 shows the calculated ECSs of GaAs in the range of T and P_{As} belonging to the shaded area in Fig. 4.3. They are mainly composed of (100), (110), (111)A, and (113)A facets, with a small portion of (113)B facets. In contrast, the

experimentally observed shapes of GaAs were composed of (100), (110), (111)A, and (111)B facets exposing similar area of (111)A and (111)B [1,2]. Although this study calculated electronic surface energies (γ^{elec}) of more reconstructions compared to the previous theoretical work [9], including (111)B (√19×√19), (113)A, and (113)B, the discrepancy between calculations and the experiments remains unsolved. Therefore, surface vibration effects were additionally considered, as discussed in next section.

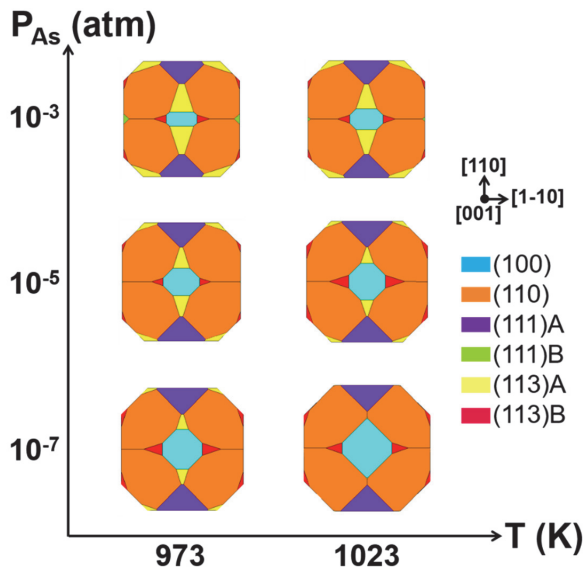

Figure 4.4 Top view of GaAs ECSs along the [001] direction constructed from electronic surface energy (γ^{elec}) around experimental growth conditions.

4.2.2. Vibrational entropy contribution

The surface vibration for the ECS prediction might be more crucial than reconstruction prediction of a single surface, because the significantly different bonding geometry of each surface can cause the highly anisotropic vibrational effects. As we did for GaAs (100) in section 3.2.2, the difference in vibrational free energy

between surface and bulk was calculated using the method described in section 2.3.4. By extending the calculation to the other surfaces, the effects of the surface vibration on the anisotropic surface energy were considered. Figure 4.5(b) shows the minimum total surface energies ($\gamma = \gamma^{elec} + \Delta\gamma^{vib}$) evaluated for each surface. Since the phonon calculation for surface requires lots of computational cost, the vibrational surface energy was evaluated only for the reconstructions with low electronic surface energy as indicated by the bold lines in Fig. 4.2.

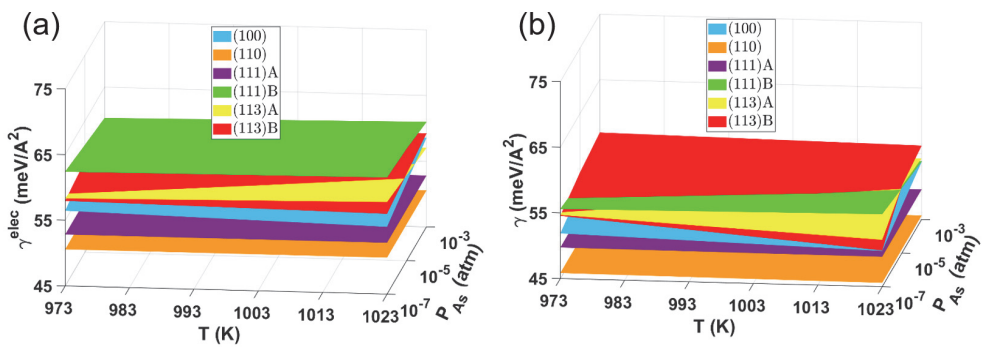

Figure 4.5 (a) Calculated electronic surface energies (γ^{elec}) and (b) total surface energies ($\gamma = \gamma^{elec} + \Delta\gamma^{vib}$) of GaAs for the several low-index surfaces as a function of T and P_{As}.

Using the total surface energies, the T–P dependent variation in ECS was again obtained as shown in Fig. 4.6. The morphology difference between Fig. 4.4 and 4.6 implies the anisotropic effects of the surface vibration on the surface energy ($\Delta\gamma^{vib}$). Compared to Fig. 4.4, the area of (113)A surfaces (yellow) is reduced, which agrees better with the experimental shapes [1,2]. Nevertheless, the (111)B facets are still not exposed in the GaAs ECSs, remaining inconsistency with the experimental shapes exposing similar area of (111)A and (111)B facets.

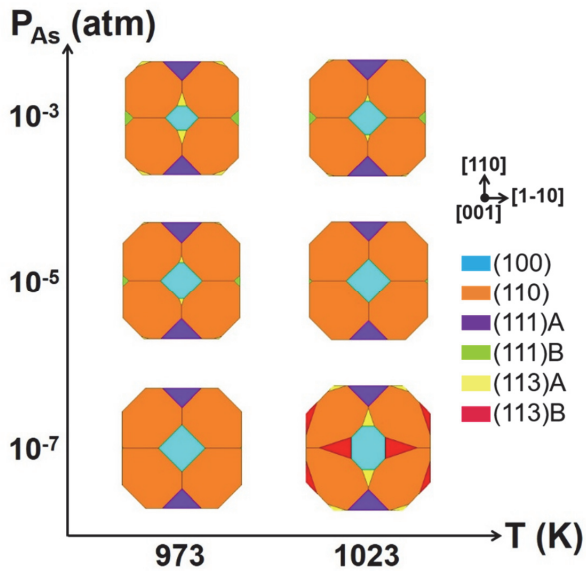

Figure 4.6 Top view of GaAs ECSs along the [001] direction constructed from total surface energy ($\gamma = \gamma^{elec} + \Delta\gamma^{vib}$) around experimental growth conditions.

4.2.3. A new (111)B reconstruction at high T

The discrepancy between the calculated ECSs and experimental shapes is likely to be caused by one of the two possibilities: (i) the equilibrium was not reached in the growth experiments and the experimental shapes were determined by kinetics rather than thermodynamics; (ii) there is an unknown reconstruction on (111)B surface whose surface energy is lower than the already known reconstructions (Fig. 4.1). In this study, we checked the second possibility by evaluating various types of new reconstruction on the (111)B surface. As a result, a new (111)B reconstruction, Ga-vacancy α(2×2), was proposed as the stable one under high T conditions.

This reconstruction was made from the substitution of the uppermost As atoms in (111)B As vacancy(2×2) by Ga atoms, as shown in Fig. 4.7(a). After the relaxation calculation is finished, the height of the Ga atoms at the uppermost layer became

identical to that of the Ga atoms at the 2nd layer. The corresponding bond lengths, denoted in Fig. 4.7(a), are almost comparable to the bond lengths of the bulk Ga in orthorhombic phase (2.45-2.73 Å) calculated under the same calculation conditions. The idea of this new reconstruction is based on the general tendency that a reconstruction having a large number of Ga atoms tends to be favorable under Ga-rich conditions, and vice versa. The dynamical stability of the (111)B Ga vacancy α(2×2) was also confirmed by the absence of any negative frequency in the band structure (Fig. 4.7(b)) and DOS (Fig. 4.7(c)) in the surface phonon. It should be noted that the frequency of the surface phonon (black lines) is significantly lower than that of the bulk phonon (shaded gray area), presumably due to the weak bonding between Ga atoms on the surface. The surface phonon mode at the $\bar{\Gamma}$ point with the highest frequency (the red circle in Fig. 4.7(b), 6.38 THz) is represented by red-blue arrows for the atoms at the uppermost layer.

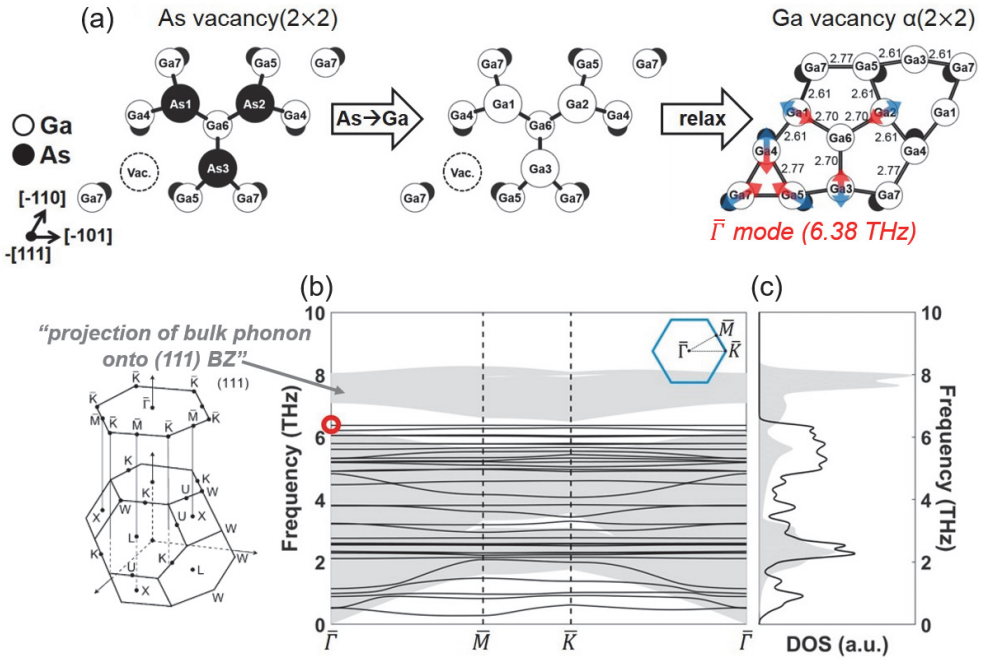

Figure 4.7 (a) Atomic structure of (111)B Ga-vacancy α(2×2). The red-blue arrows for the atoms at the uppermost layer denote the surface phonon mode at the $\bar{\Gamma}$ point with the highest frequency. (b) Band structure and (c) DOS of surface phonon of the (111)B Ga-vacancy α(2×2) (black line), with the projection of bulk phonon of ZB-GaAs onto the 2D Brillouin zone (shaded gray area).

In addition to the dynamical stability, the energetic stability of the (111)B Ga vacancy α(2×2) reconstruction was confirmed by surface energy calculations. In fact, the surface energy of Ga vacancy α(2×2) was predicted to be higher than that of Filled(√19×√19) when considering only the electronic surface energy (γ^{elec}) as shown in Fig. 4.8(b). However, dramatic changes in the order of surface energy occur when considering the total surface energy ($\gamma = \gamma^{elec} + \Delta\gamma^{vib}$) as clarified in comparison between Fig. 4.8(c) and 4.8(d). Figure 4.8(d) confirms that the Ga vacancy α(2×2) reconstruction is energetically stable in the T and P_{As} range of

interest (high T) on the (111)B surface. This is because the amount of surface energy reduction by the vibrational surface energy ($\Delta\gamma^{vib}$) of the Ga vacancy α(2×2) is much larger than that of the other (111)B reconstructions. This is presumably originated from the lower frequency of the surface vibration resulting from the weak bonding between Ga atoms in the Ga vacancy α(2×2) reconstruction. Figure 4.8(a) clearly shows that phonon frequency of the Ga vacancy α(2×2) is much lower than that of the other (111)B reconstructions as well as bulk ZB-GaAs (shaded gray area). These calculation results are consistent with the previous experimental studies observing the high T transition from (√19×√19) on the GaAs (111)B surface through RHEED [14] and STM [15]. In addition, the tendency for the surface structure with electronically weak bonding to become stable under a high T condition was also reported in the previous calculation for a different material system, which was called subtle interplay between electronic energy and vibrational entropy [28].

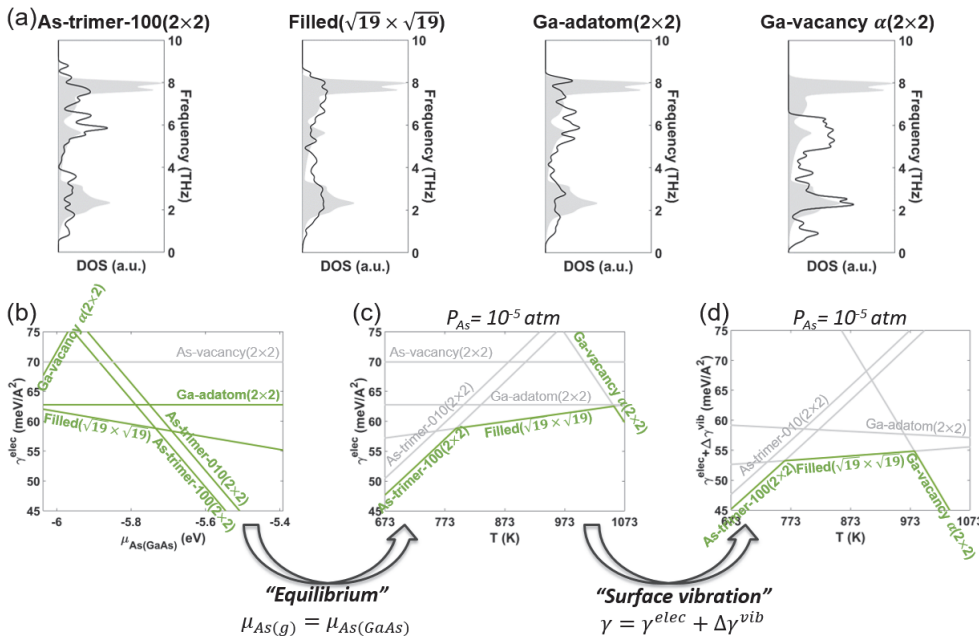

Figure 4.8 (a) Surface phonon DOS of GaAs (111)B reconstructions (black lines) having low surface energy. Bulk phonon of ZB-GaAs is represented as shaded area for comparison. (b) Electronic surface energies (γ^{elec}) of the (111)B reconstructions as a function of As chemical potential. The reconstructions with low surface energy are highlighted by green bold lines. (c) The electronic and (d) total surface energies ($\gamma = \gamma^{elec} + \Delta\gamma^{vib}$) as a function of T at a fixed P_{As} of 10^{-5} atm. The reconstructions with the lowest surface energy are highlighted by green bold lines.

Including both the surface vibration effects and the new (111)B Ga vacancy α(2×2), the T–P dependent variation in ECS was finally constructed as shown in Fig. 4.9. The large reduction of (111)B surface energy by the new reconstruction contributes to the obvious existence of the (111)B facets. The exposure of (111)B facets in the ECS under high T (*i.e.*, Ga-rich) conditions is well matched with the experimental shapes of GaAs [1,2]. The correspondence between the calculated ECS

and the experimental shapes implies that the equilibrium is reached in the previous growth experiments. It is notable that the correspondence was achieved only when both the new reconstruction and vibrational surface energy were considered, as shown in Fig. 4.10 where the variation in ECS is represented with respect to the changes in calculation method at a fixed T of 1023 K and P_{As} of 10^{-5} atm.

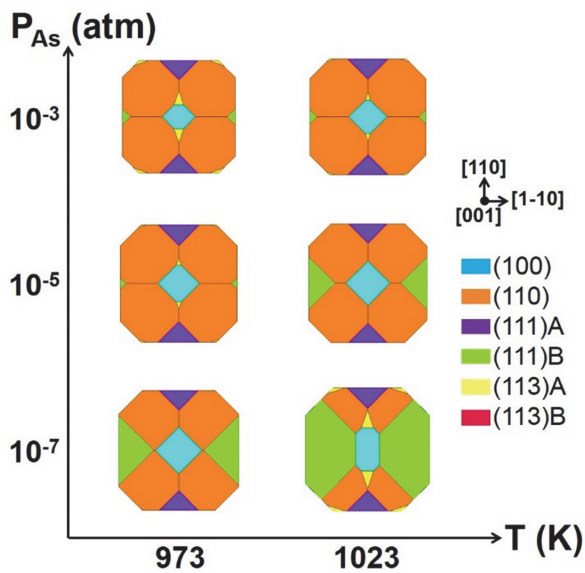

Figure 4.9 After consideration of (111)B Ga-vacancy α(2×2) reconstruction, top view of GaAs ECSs along the [001] direction constructed from total surface energy ($\gamma = \gamma^{elec} + \Delta\gamma^{vib}$) around experimental growth conditions.

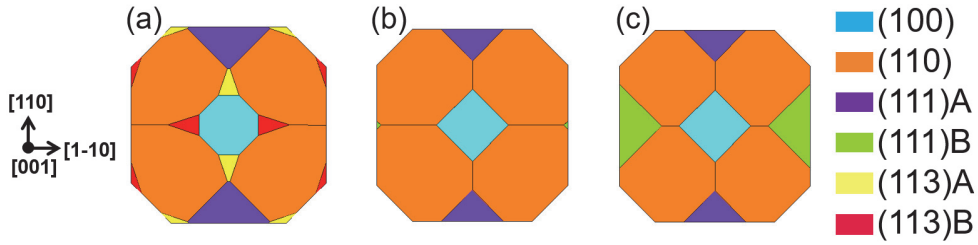

Figure 4.10 Changes in calculated ECS of GaAs at a fixed T of 1023 K and P_{As} of 10^{-5} atm. Top view of the ECS constructed from (a) electronic surface energy (γ^{elec}), (b) total surface energy ($\gamma = \gamma^{elec} + \Delta\gamma^{vib}$), and (c) the total surface energy after consideration of (111)B Ga-vacancy α(2×2).

4.3 Conclusion

In this chapter, the ECS of GaAs was predicted as a function of T and P_{As} by expanding the method applied to GaAs (100) surface to other low-index surfaces: (110), (111)A, (111)B, (113)A, and (113)B. The anisotropic vibration effects were investigated by showing the significant dependence of vibrational surface energy on the surface reconstruction and orientation. This leads to the large difference between ECS prediction from electronic surface energy and that from total surface energy including both the electronic and vibrational contributions. In particular, a new (111)B reconstruction, Ga vacancy α(2×2), was proposed to be stabilized at high T by high vibrational entropy. The dynamical and energetic stability of this reconstruction was confirmed. Both the new reconstruction and vibrational surface energy contributed to the significant reduction of (111)B surface energy, leading to the ECS prediction in agreement with the experimental shapes exposing similar area of (111)A and (111)B facets.

4.4 Bibliography

[1] K. Ikejiri, J. Noborisaka, S. Hara, J. Motohisa and T. Fukui, Mechanism of Catalyst-Free Growth of GaAs Nanowires by Selective Area MOVPE, *J. Cryst. Growth*, **298**, 616-619, (2007).

[2] K. Tomioka, K. Ikejiri, T. Tanaka, J. Motohisa, S. Hara, K. Hiruma and T. Fukui, Selective-Area Growth of III-V Nanowires and Their Applications, *J. Mater. Res.*, **26**, 2127-2141, (2011).

[3] C. Renard, N. Cherkashin, A. Jaffre, T. Molière, G. Hallais, L. Vincent, J. Alvarez, D. Mencaraglia, A. Michel and D. Bouchier, Growth of High Quality Micrometer Scale GaAs/Si Crystals from (001) Si Nano-Areas in SiO2, *J. Cryst. Growth*, **401**, 554-558, (2014).

[4] P.-S. Wong, B. Liang, R. Molecke, J. Tatebayashi and D. L. Huffaker, Controlled Formation and Dynamic Wulff Simulation of Equilibrium Crystal Shapes of GaAs Pyramidal Structures on Nanopatterned Substrates, *Cryst. Growth Des.*, **10**, 2509-2514, (2010).

[5] S. Lee and S. Brueck, Equilibrium Crystal Shape of GaAs in Nanoscale Patterned Growth, *J. Appl. Phys.*, **96**, 1214-1218, (2004).

[6] J. Andrés, L. Gracia, A. F. Gouveia, M. M. Ferrer and E. Longo, Effects of Surface Stability on the Morphological Transformation of Metals and Metal Oxides as Investigated by First-Principles Calculations, *Nanotechnology*, **26**, 405703, (2015).

[7] H. Li, L. Geelhaar, H. Riechert and C. Draxl, Computing Equilibrium Shapes of Wurtzite Crystals: The Example of GaN, *Phys. Rev. Lett.*, **115**, 085503, (2015).

[8] Y. Meng, X.-W. Liu, M. Bai, W.-P. Guo, D.-B. Cao, Y. Yang, Y.-W. Li and X.-D. Wen, Prediction on Morphologies and Phase Equilibrium Diagram of Iron Oxides Nanoparticles, *Appl. Surf. Sci.*, **480**, 478-486, (2019).

[9] N. Moll, A. Kley, E. Pehlke and M. Scheffler, GaAs Equilibrium Crystal Shape from First Principles, *Phys. Rev. B*, **54**, 8844, (1996).

[10] N. Moll, M. Scheffler and E. Pehlke, Influence of Surface Stress on the Equilibrium Shape of Strained Quantum Dots, *Phys. Rev. B*, **58**, 4566, (1998).

[11] Q. Liu, N. Moll, M. Scheffler and E. Pehlke, Equilibrium Shapes and Energies of Coherent Strained InP Islands, *Phys. Rev. B*, **60**, 17008, (1999).

[12] I. W. Yeu, G. Han, J. Park, C. S. Hwang and J.-H. Choi, Equilibrium Crystal Shape of GaAs and InAs Considering Surface Vibration and New (111)B Reconstruction: Ab-Initio Thermodynamics, *Sci. Rep.*, **9**, 1127, (2019).

[13] D. Woolf, D. Westwood and R. Williams, The Homoepitaxial Growth of GaAs (111)A and (111)B by Molecular Beam Epitaxy: An Investigation of the Temperature-Dependent Surface Reconstructions and Bulk Electrical Conductivity Transitions, *Semicond. Sci. Technol.*, **8**, 1075, (1993).

[14] D. Woolf, D. Westwood and R. Williams, Surface Reconstructions of GaAs (111)A and (111)B: A Static Surface Phase Study by Reflection High-Energy Electron Diffraction, *Appl. Phys. Lett.*, **62**, 1370-1372, (1993).

[15] J. Thornton, D. Woolf and P. Weightman, Reconstructions of the GaAs (111)B Surface, *Appl. Surf. Sci.*, **123**, 115-119, (1998).

[16] I. W. Yeu, J. Park, G. Han, C. S. Hwang and J.-H. Choi, Surface Reconstruction of InAs (001) Depending on the Pressure and Temperature

Examined by Density Functional Thermodynamics, *Sci. Rep.*, **7**, 1-13, (2017).

[17] W. Schmidt, III-V Compound Semiconductor (001) Surfaces, *Appl. Phys. A*, **75**, 89-99, (2002).

[18] O. Romanyuk, F. Grosse, A. Proessdorf, W. Braun and H. Riechert, Stabilization of Semiconductor Surface Reconstructions by Configurational Entropy, *Phys. Rev. B*, **82**, 125315, (2010).

[19] H. Koga, Structure of GaAs (1^{-} 1^{-} 1^{-}) under Ga-Rich Conditions: A $\sqrt{19}\times\sqrt{19}$ Reconstruction Model, *Phys. Rev. B*, **82**, 113301, (2010).

[20] A. Jenichen and C. Engler, Reconstructions and Surface Facets of the GaAs (112)A and (112)B Surfaces: First-Principles DFT Supercell Calculations, *Surf. Sci.*, **608**, 204-211, (2013).

[21] C. Setzer, J. Platen, W. Ranke and K. Jacobi, Low Energy Electron Diffraction and Photoelectron Spectroscopy Study of GaAs (113)A and (113)B Surfaces Prepared by Molecular Beam Epitaxy and by Ion Bombardment and Annealing, *Surf. Sci.*, **419**, 291-302, (1999).

[22] J. Platen, A. Kley, C. Setzer, K. Jacobi, P. Ruggerone and M. Scheffler, The Importance of High-Index Surfaces for the Morphology of GaAs Quantum Dots, *J. Appl. Phys.*, **85**, 3597-3601, (1999).

[23] J. Marquez, L. Geelhaar and K. Jacobi, Atomic Structure of the GaAs (1^{-} 1^{-} 3^{-})B (8×1) Surface Reconstruction, *Phys. Rev. B*, **62**, 9969, (2000).

[24] G. Wulff, On the Question of Speed of Growth and Dissolution of Crystal Surfaces, *Z. Kristallogr*, **34**, 449, (1901).

[25] A. R. Roosen, R. P. McCormack and W. C. Carter, Wulffman: A Tool for the Calculation and Display of Crystal Shapes, *Comput. Mater. Sci.*, **11**, 16-26, (1998).

[26] R. V. Zucker, D. Chatain, U. Dahmen, S. Hagège and W. C. Carter, New Software Tools for the Calculation and Display of Isolated and Attached Interfacial-Energy Minimizing Particle Shapes, *J. Mater. Sci.*, **47**, 8290-8302, (2012).

[27] D. Scopece, Sowos: An Open-Source Program for the Three-Dimensional Wulff Construction, *J. Appl. Crystallogr.*, **46**, 811-816, (2013).

[28] S. Wippermann and W. G. Schmidt, Entropy Explains Metal-Insulator Transition of the Si (111)-In Nanowire Array, *Phys. Rev. Lett.*, **105**, 126102, (2010).

Chapter 5. Nanowire growth of GaAs

5.1. Introduction

Over the past decades, the III-V semiconductor NWs have attracted substantial attention as an ideal system for the growth mechanism study [1-3] and electronic-photonic device applications [4-6]. Therefore, extensive experiments have been attempted to grow high-quality III-V NWs using vapor-phase growth techniques, which have shown promising developments by careful control of the growth variables: growth mode, growth conditions of T and P, and substrate orientation. It has been found that under narrow T–P range, the unidirectional growth along a certain crystallographic direction (<111>B for GaAs) is induced [7-15], and that the involvement of stacking-fault (SF) and polytypism in the grown NW depends on the T–P conditions [16-18]. Nevertheless, the effects of the growth variables have not yet been fully elucidated and the lack of atomic-scale understanding deters the precise control of the NW growth.

In this chapter, an *ab initio* approaches will be provided to take a step forward in the theoretical modeling on the growth of GaAs NWs. In order to understand the effects of growth conditions and directions, we investigated the vapor-phase growth kinetics under arbitrary T–P conditions by combining the atomic-scale calculation with the stochastic growth model. Considering the entropy contribution and the electronic energy, the change in Gibbs free energy, composed of the chemical potential and surface energy, was evaluated at each stage of adsorption, nucleation, and growth as a function of T and P. It enabled us to predict the T–P dependent variation in nucleation rate along different crystallographic directions with possible

stacking sequences: ZB, SF, twin (TW), and WZ. As a result, the reason why the unidirectional growth of GaAs happens only along one specific direction, <111>B, was demonstrated as the excessive source supply to (111)B surface induced by preferential adsorption under narrow T–P conditions [19]. In addition, the intriguing asymmetry (polarity) in stacking behavior during the growth along the two opposite polar directions, <111>A and <111>B, and its dependence on growth condition were fundamentally elucidated, showing a perfect agreement with experimental observations [20].

The proposed *ab initio* approaches are truly independent of any empirical data, bridging the gap between atomic-scale static calculation and kinetic growth process under arbitrary vapor-phase conditions. Therefore, it will contribute to the nanoscale growth of various materials, including other III-V and II-VI NWs and two-dimensional materials, where the precise control of the growth and stacking sequence is important for their properties.

5.1.1. Growth methods of nanowire

Various methods have been exploited to promote the unidirectional growth of GaAs. The Au-catalyzed vapor-liquid-solid (VLS) method [7,8] has been most widely used for the synthesis of NWs, which promotes the axial growth rate by using a metal catalyst (usually Au) that fosters both the adsorption (gathering the vapor sources) and nucleation (incorporation into GaAs). The oxide-assisted growth (OAG) method [9] is based on suppressing the growth rate along the lateral directions by covering the GaAs core with a Ga_2O_3 oxide shell. In the SA epitaxy methods, the growth modes are divided into two distinctive methods depending on the As/Ga ratio

[21]: (i) when an effective As/Ga ratio is lower than 1, the excess Ga atoms are accumulated on the surface, leading to the formation of liquid Ga droplets, and the NW growth proceeds through the VLS mechanism (called self-catalyzed or Ga-assisted growth); (ii) when an effective As/Ga ratio is higher than 1, on the other hand, the liquid droplets no longer remain and the NW growth proceeds through the non-catalytic facet-driven method (or called vapor-solid, VS). Since the As element is much more volatile than the Ga element, the effective As/Ga ratio of 1 is generally achieved at an actual As/Ga ratio higher than 10. Among the various growth methods of NW, we are going to focus on the VS growth of GaAs NWs.

5.1.2. Anisotropic growth and preferential nucleation

While all of the above-mentioned methods have been shown to produce GaAs NWs, it has proven challenging to successfully remove the liquid phase catalysts or surface oxide layer without damaging the GaAs NWs in VLS or OAG, respectively. Therefore, the VS growth has been expected to be a promising way to form sharp heterostructures excluding an unintentional incorporation of foreign impurities [22,23]. The vapor-phase growth techniques of SA-MBE and SA-MOVPE have been utilized to induce the VS growth of GaAs NWs.

However, there are constraints in growth directions and T–P conditions to realize the NW growth by the VS method. It has been reported that the GaAs NWs prefer to grow along the <111>B direction under limited T–P conditions [11-15]. The GaAs NWs did not grow under too low T and high P conditions, while the unidirectional growth along the <111>B was promoted when T increases and P decreases [13,14]. Meanwhile, certain reconstruction changes of the (111)B surface have been

suggested to be relevant to the suppression and enhancement of the unidirectional growth along the <111>B direction. That is, As-trimer(2×2) reconstruction, which is stable under low T and high P conditions, was related to the suppressed growth rate along the <111>B direction, while (√19×√19) reconstruction, which is stable under high T and low P conditions, was expected to enhance the axial growth rate [15,17]. However, there has been lack of satisfactory explanation about the interrelationship between the surface reconstruction and the unidirectional VS growth.

The mechanism can be estimated to be the formation of facets depending on the growth conditions, which induces the difference in relative growth rate along the different crystallographic surfaces. In particular, the preferential nucleation at one interface was proposed as the general mechanism that describes why NWs grow faster along one direction than along the others [24]. Therefore, the orientation-dependent nucleation rate, written in Eq. (2.19) in section 2.5.1, is likely to be a key factor to elucidate why the unidirectional growth happens along the <111>B direction under the constrained T–P conditions. The nucleation rate is specifically determined by two terms: the rate of source supply onto each surface and nucleation barrier on each surface. Both of them depend on T–P dependent surface structures. In section 5.2, we will demonstrate the fundamental mechanism behind the constrained growth of the VS NWs, by showing that the preferential adsorption of As atoms occurs on the (111)B surface at narrow range of T–P conditions, leading to relatively high rate of source supply and nucleation on the (111)B surface.

5.1.3. Asymmetric stacking along polar direction

Suppressing the formation of the stacking defects, such as SF, TW, and even

secondary phase of WZ, has remained as a challenging task in the NW growth of ZB III-V [3,25]. These defects are particularly harmful in III-V NWs, because SF-induced TW and ZB-WZ polytypism degrade the carrier mobility and optical response [26,27]. To eliminate the involvement of SF and polytypism, considerable experiments have been performed by manipulating the growth conditions and substrate orientation; the density of the stacking defects has been reported to decrease by increasing T [16-18] and decreasing P [18] as well as by changing the growth direction from <111>B to <111>A [28,29] for GaAs NWs grown by the SA epitaxy method. However, the mechanism behind such heuristic findings has not yet been fully understood.

In particular, the asymmetric stacking along the two opposite polar directions, <111>A and <111>B, is an intriguing and unique property of III-V NWs compared to the group IV NWs with diamond cubic structure (centrosymmetric $Fd\bar{3}m$). The crystallographic origin is that both the ZB ($F\bar{4}3m$) and WZ ($P6_3mc$) structures of GaAs are non-centrosymmetric and the common growth directions, <111> of ZB and <0001> of WZ, are polar. The NWs grown along A- (cationic) and B- (anionic) polar directions are referred to as <111>A (A-polar) and <111>B (B-polar) NWs, respectively [10,28]. Here, for ZB-GaAs, the <111>A NW will be briefly represented as ANW, where the growing surface corresponds to the (111)A (*i.e.*, Ga-terminated (111), $(1\bar{1}\bar{1})$, $(\bar{1}1\bar{1})$, and $(\bar{1}\bar{1}1)$), while the <111>B NW will be represented as BNW exposing (111)B (*i.e.*, As-terminated $(\bar{1}\bar{1}\bar{1})$, $(\bar{1}11)$, $(1\bar{1}1)$, and $(11\bar{1})$) as the growing surface.

In the previous theoretical approaches, the formation of polytypism in GaAs NWs was explained in terms of the energetics of fully formed NWs [30,31]: the formation

of secondary WZ segments in ZB NWs was attributed to the corresponding small radius having high surface-to-volume ratio and lower surface energy of WZ compared to ZB [32]. However, this thermodynamic model cannot explain the experimentally observed difference in SF density between the GaAs ANWs and BNWs [28,29]. Given that the growth directions of the ANW and BNW are just opposite each other, there is no reason for the total energy of the SF-embedded NW to depend on the growth direction, either <111>A or <111>B. This is because the usual stacking fault energy does not reflect the polarity dependence, hence is identical for both the ANW and BNW.

The critical limitations in the previous thermodynamic approaches imply that a different point of view is necessary to explain the different stacking behavior of ANW and BNW. We started this research from the intuitions: (i) kinetic aspects must be a dominant factor of the defect formation; (ii) the determination of stacking sequence must be accidentally and stochastically determined during the adsorption-nucleation-growth kinetic processes; (iii) the difference in reconstruction structure between (111)A and (111)B surfaces is likely to play a critical role, resulting in the asymmetric stacking behavior. In section 5.3, the mechanism on the asymmetric stacking behavior and its dependence on growth conditions will be discussed, by calculating the T–P dependent nucleation rate with possible stacking sequences (ZB, SF, TW, and WZ) for the ANW and BNW. The dependence of stacking formation on the T–P conditions and growth directions, predicted from *ab initio* calculations, was directly comparable to the experimental observations and showed remarkable correspondence with the experimental results.

5.2. Anisotropic adsorption and growth

In this section, the mechanism of the facet-driven VS growth of GaAs BNWs will be theoretically investigated by verifying how the relative growth rate of (111)B surface overwhelms those of the other surfaces in a certain T–P range. Specifically, how the nucleation rate on (111)B surface is much faster than that on the other surfaces will be discussed.

5.2.1. Preferential nucleation and nanowire growth

In order to demonstrate the preferential nucleation on one specific surface, the high rate of source supply, $\dot{C}(Surf, T, P)$ in Eq. (2.19), or the low nucleation barrier, $\Delta G_{sn}^{*}(Surf, T, P)$ in Eq. (2.19), must be verified on the surface. As will be shown in section 5.3, there is no difference in nucleation barrier between the ANW and BNW. Therefore, it can be inferred that the preferential nucleation on the (111)B surface is caused by the extremely high rate of source supply on the (111)B surface. In particular, for the facet-driven VS growth, the way to supply Ga and As sources to each surface is the vapor phase adsorption. Therefore, the formation of facets and the changes in surface reconstruction, caused by the changes in T–P, govern the anisotropic source supply onto each surface.

5.2.2. Adsorption on surface reconstruction

First, the stable reconstructions under the experimentally relevant conditions were identified for the several low-index surfaces. The surface energy of the various reconstructions was calculated as a function of T and P_{As} following the methods described in chapter 3 and 4. Figure 5.1(a) and (b) show the minimum surface

energies of the low-index surfaces including (100), (110), (111)A, and (111)B at fixed P_{As} of 4×10^{-9} and 10^{-5} atm, respectively. Each P_{As} corresponds to the common pressure exploited in the MBE and MOVPE experiments and the shaded gray areas correspond to the T range under which the vapor-phase growth of GaAs has been conducted. In the figure, the corresponding reconstructions are also denoted along with the lowest surface energy lines for each surface. Note that the (113)A and (113)B surfaces were not considered here because their facets do not appear in the ECSs as confirmed in chapter 4.

Figure 5.1 indicates that the reconstruction changes occurs only for the (111)B surface within the experimentally relevant T window. This implies that the (111)B surface is the most feasible origin of the experimental observations, the T–P dependent growth and no growth of GaAs BNWs. It is notable that previous reports suggested that the As-trimer(2×2) (at low T and high P) and the filled(√19×√19) reconstructions (at high T and low P) contribute to the suppressed and enhanced growth rate along the <111>B direction, respectively [15,17]. In contrast, according to this calculation results, the As-trimer(2×2) is stable at substantially lower T than the experimentally relevant T range. In fact, the reconstruction might not have been formed on the (111)B surface in the previous experiments. Instead, the filled(√19×√19) and Ga-vacancy α(2×2) reconstructions are likely to be the actual surface structures that is relevant to the GaAs BNW growth.

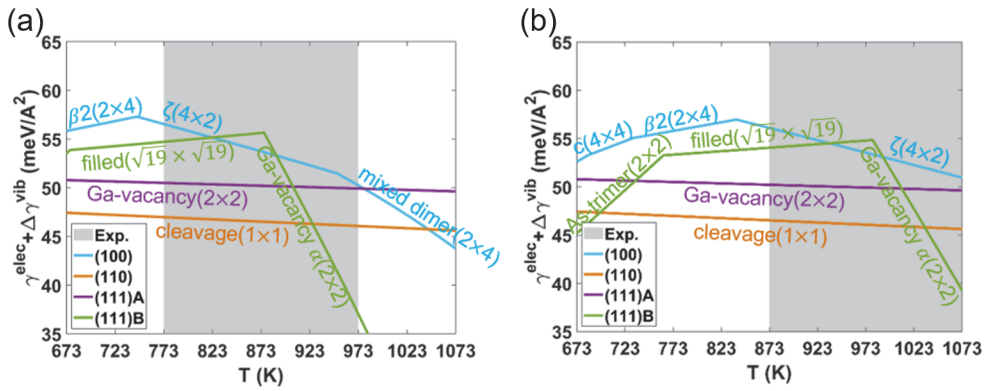

Figure 5.1 Calculated minimum surface energies including both the electronic and vibrational terms ($\gamma = \gamma^{elec} + \Delta\gamma^{vib}$) of GaAs (100), (110), (111)A, and (111)B surfaces. The results are presented as a function of T at fixed P_{As} of (a) 4×10^{-9} and (b) 10^{-5} atm, which correspond to the common P of MBE and MOVPE experiments, respectively. The shaded gray areas correspond to the experimentally relevant conditions and the reconstructions with the lowest energy are denoted for each surface.

As next step, the adsorption energy was evaluated on the stable reconstructions. Figure 5.2 shows the atomic structures of the most stable reconstructions in the range of the shaded areas in Fig. 5.1. The most stable reconstructions were considered as adsorbent to the incoming adsorbates. The symmetrically inequivalent sites on the stable reconstructions, denoted in Fig. 5.2, were selected as possible adsorption sites. Then, the energy of an adsorbed atom at each adsorption site was calculated using the following equation in the case of the Ga adsorption on (100) surface as an example:

$$E_{Ga(ad)}^{(100)} = E_{surf\cdot Ga}^{(100)} - E_{surf}^{(100)}, \tag{5.1}$$

where, $E_{surf\cdot Ga}^{(100)}$ and $E_{surf}^{(100)}$ are the total energies of the (100) slab with and

without an adsorbed Ga atom, respectively. The energies of the Ga (As) atom adsorbed at each adsorption site were calculated using Eq. (5.1) and all the values are summarized in Table 5.1 (Table 5.2). In this tables, the lowest energy for each reconstruction is underlined and the corresponding site is likely to be the most probable adsorption site.

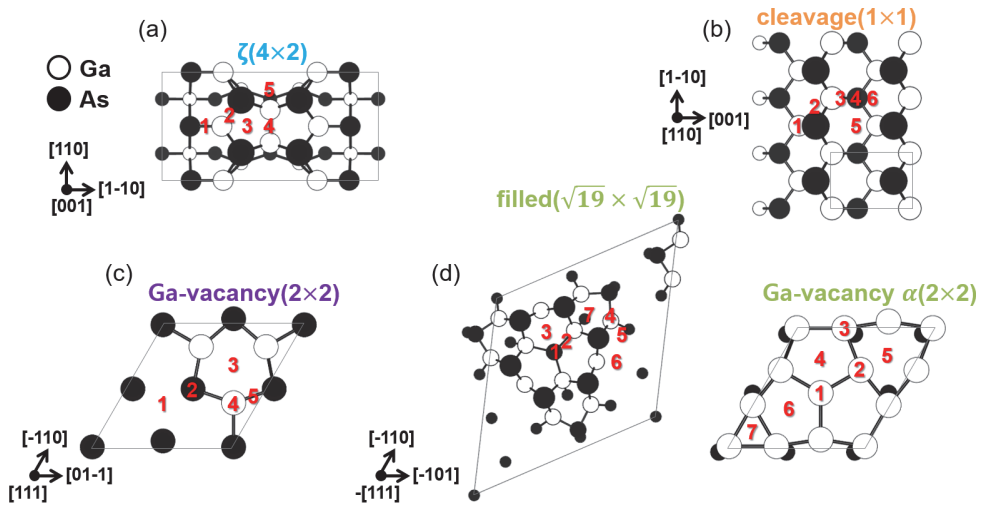

Figure 5.2 Top view of the atomic structures and considered adsorption sites on GaAs (a) (100) ζ(4×2); (b) (110) cleavage(1×1); (c) (111)A Ga-vacancy(2×2); and (d) (111)B filled(√19×√19) and Ga-vacancy α(2×2) reconstructions. All of the presented surface areas correspond to the reconstructed unit cell, except for the (110) cleavage(1×1), whose unit cell (marked by gray rectangle at the right bottom corner) was enlarged in order to obtain sufficient in-plane distance between the same adsorbed atom in different periodic cells.

Table 5.1 Energies of a Ga atom adsorbed at the sites indicated in Fig. 5.2. The lowest energy is underlined for each reconstruction.

		$E_{Ga(ad)}$ (eV) for each site						
		1	**2**	**3**	**4**	**5**	**6**	**7**
(100)	ζ(4×2)	<u>-2.55</u>	-2.16	-2.16	-2.15	-2.53		
(110)	cleavage (1×1)	-2.61	-2.16	<u>-2.74</u>	-2.73	-2.61	-2.73	
(111)A	Ga-vacancy (2×2)	<u>-2.59</u>	-2.24	-2.24	-2.25	-2.25		
(111)B	filled (√19×√19)	-2.59	-2.59	-2.57	-2.72	<u>-3.08</u>	-3.06	-2.72
(111)B	Ga-vacancy α(2×2)	<u>-3.33</u>	<u>-3.33</u>	<u>-3.33</u>	-3.31	-3.04	-3.31	-3.02

Table 5.2 Energies of an As atom adsorbed at the sites indicated in Fig. 5.2. The lowest energy is underlined for each reconstruction.

		$E_{As(ad)}$ (eV) for each site						
		1	**2**	**3**	**4**	**5**	**6**	**7**
(100)	ζ(4×2)	<u>-3.79</u>	-3.63	-3.56	-3.22	-3.63		
(110)	cleavage (1×1)	<u>-4.16</u>	-3.42	-4.07	-3.73	<u>-4.16</u>	-3.73	
(111)A	Ga-vacancy (2×2)	-3.40	-3.85	-3.76	<u>-4.24</u>	-4.14		
(111)B	filled (√19×√19)	-4.40	<u>-4.41</u>	<u>-4.41</u>	-3.72	-4.15	-4.24	-4.06
(111)B	Ga-vacancy α(2×2)	-5.76	-5.46	<u>-6.03</u>	-5.57	-5.46	-5.59	-5.80

5.2.3. Preferential adsorption on (111)B surface

Finally, the anisotropic adsorption behavior was discussed in terms of the adsorption difference between different surfaces in contact with the same reference state, the surrounding vapor environment. The vapor environment was assumed to be composed of Ga(g), As_2(g), and As_4(g) in accordance with the practical conditions in MBE and MOVPE systems for the GaAs growth. Its adsorption-desorption behavior, whether adsorption or desorption is more preferred, was determined by the criteria depicted in Fig. 2.14 in section 2.5.2. Since an element prefers to move from a higher chemical potential to a smaller chemical potential system, the adsorption will be preferred if the chemical potential of vapor phase is higher than that of adsorbed state. In the case of the Ga adsorption on (100) surface as an example, the adsorption might be favorable if $E_{Ga(ad)}^{(100)}$ is lower than $\mu_{Ga(Gas)}$.

By combining the variation in the stable reconstructions (Fig. 5.1) and the lowest energy of a Ga atom adsorbed on each reconstruction (Table 5.1), the variation of the minimum energy of an adsorbed Ga atom ($E_{Ga(ad)}$) was evaluated as a function of T at a fixed P_{As} of 10^{-5} atm, as shown in Fig. 5.3(a). The reason why only the (111)B surface (green line) shows the abrupt change is due to the reconstruction change from filled($\sqrt{19}\times\sqrt{19}$) to Ga-vacancy α(2×2). In this figure, the chemical potentials of Ga in gas phase ($\mu_{Ga(Gas)}$), calculated using the method described in section 2.3.2, are represented by black solid lines. The P_{Ga} was set to be 10~100 times lower than the P_{As} because the usual As/Ga ratio is much higher than 10 during the VS growth of GaAs. Note that the energy of Ga adsorbed on (111)B surface is lower than $\mu_{Ga(Gas)}$ throughout most of the T range considered. Therefore, over the entire T–P ranges,

the Ga atoms in the vapor will prefer to be adsorbed on the (111)B surface. This will, in turn, enhance the growth along the <111>B direction, *i.e.*, the BNW growth.

While the Ga adsorption on (100) and (111)A surfaces is expected to be unfavorable, the chance of such adsorption on (110) surface cannot be ignored. This is consistent with the previous reports that the Ga atom can be supplied to (111)B surface from not only the direct adsorption on the (111)B surface but also the surface diffusion through (110) sidewalls of NWs [8,14,21]. In contrast, the sidewall diffusion is not expectable for As atom.

Figure 5.3(b) shows the minimum energy of an adsorbed As atom ($E_{As(ad)}$) for each surface, along with its chemical potential in the gas phase ($\mu_{As(Gas)}$) as a function of T at a fixed P_{As} of 10^{-5} atm. In stark contrast to Ga element, most of the $\mu_{As(Gas)}$ was lower than the $E_{As(ad)}$, suggesting that the As adsorption on the crystal facets will be much more difficult than the Ga adsorption. This is consistent with the much higher vapor pressure of As than Ga. In addition, these results coincide with the previous experimental findings that the surface diffusion through (110) sidewalls of NWs is almost improbable for As element [8,14,21]. According to Fig. 5.3(b), this is because the As adsorption on (110) surface leads to a large energy increase so the diffusion length of As on the (110) is very short. Nevertheless, there is a relatively narrow T range (980~1018 K) in which the As adsorption on the (111)B surface is expected to be favorable. Considering that the adsorption on the other surfaces is not preferred and the direct adsorption is the only way to supply As atom to the (111)B surface, the exclusively large amount of As sources will be provided on the (111)B surface in the narrow T range.

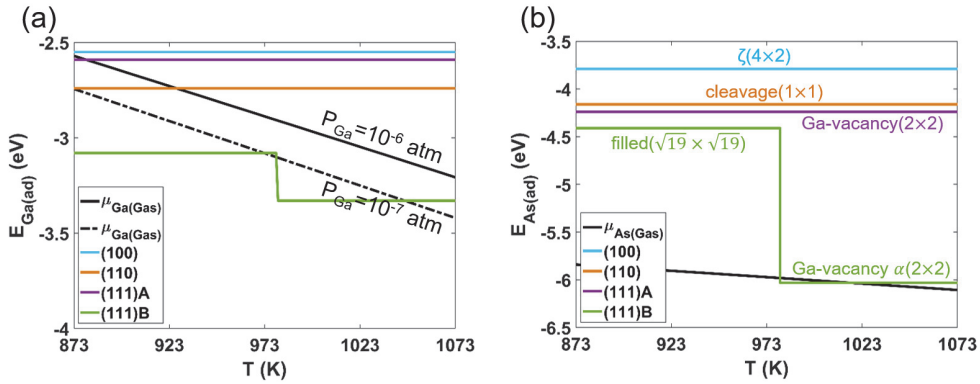

Figure 5.3 Calculated minimum energies of (a) Ga and (b) As atom adsorbed on each surface and its chemical potential in gas phase as a function of T at a fixed P_{As} of 10^{-5} atm. For the chemical potential of Ga in gas phase, 10~100 times lower values of P_{Ga} compared to the P_{As} were used. Note that the abrupt change of the (111)B surface is due to the reconstruction change as denoted.

Figure 5.3(b) implies that the As adsorption on the (111)B surface becomes preferred as the stable reconstruction changes from filled(√19×√19) to Ga-vacancy α(2×2). However, the As adsorption start to be desorbed again when T exceeds a critical point. This boundary conditions imposed on As element may be highly relevant to the peculiar VS growth behavior: the unidirectional growth of GaAs did not happen under SA-MOVPE conditions of either too low T (below 873 K) or too high T (above 1073 K) [13,14,17]. Accordingly, all the T–P range at which $E_{As(ad)}^{(111)B}$ is lower than $\mu_{As(Gas)}$ was evaluated and presented as green area in Fig. 5.4(a).

Under the T–P conditions indicated by the green area, the exclusive source supply on the (111)B surface will be achieved, leading to the extremely high rate of nucleation on the (111)B surface compared to the other surfaces. Therefore, these limited T–P conditions will correspond to the conditions under which the

unidirectional growth along the <111>B direction is induced as schematically depicted in Fig. 5.4(b). For verification, the previous VS growth conditions of the GaAs BNWs using SA-MOVPE [11-15,17,18] and SA-MBE [21,33] are also indicated in Fig. 5.4(a) by the blue and red rectangular areas, respectively. The experimental conditions for the successful growth of GaAs BNWs, marked by (O) in the index column, are around 973~1023 K for SA-MOVPE and ~903 K for SA-MBE, which are located within the green area. On the other hand, the experimental conditions under which GaAs BNWs failed to grow, marked by (X) in the index column, are confirmed to be far out of the calculated range. The correspondence between the theoretically predicted T–P range and the experimental growth conditions confirms that the unidirectional growth, allowed along the <111>B direction under the limited T–P conditions, is caused by anisotropic source supply onto each surface.

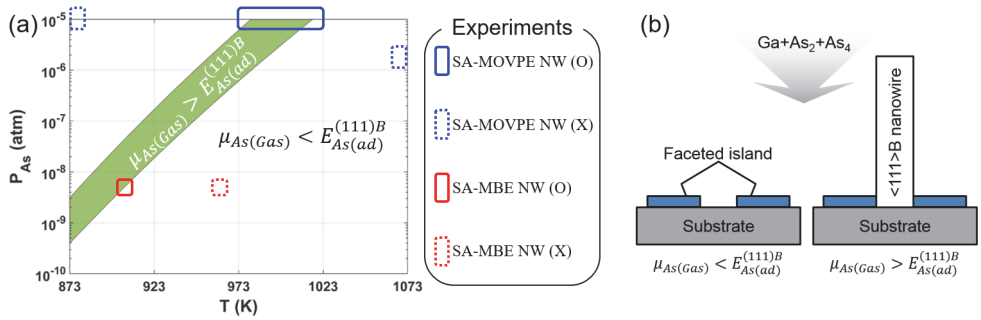

Figure 5.4 (a) Calculated T–P range in which the As adsorption on (111)B surface is exclusively favorable (green area). The rectangular area surrounded by the solid line represents the experimental conditions for the successful growth of GaAs NWs, while the rectangular area surrounded by the dashed lines represents the experimental conditions under which GaAs BNWs failed to grow, by non-catalytic VS methods: SA-MOVPE (blue) and SA-MBE (red). (b) Schematic depiction of the criteria for whether the NW grows or not.

5.3 Asymmetric nucleation and stacking sequence

5.3.1. Nucleation and growth model

As confirmed by the *in situ* transmission electron microscopy (TEM) observations on GaAs VLS NW [34,35] and tungsten oxide VS NW [36], the NW growth proceeds through layer-by-layer mechanism initiated by a nucleus on each layer (*i.e.*, birth and spread). Figure 5.5 schematically depicts the repetitive growth processes: nucleation and process. After the preferential adsorption (section 5.2) on the growing crystal (c) surface, the adsorbed source (s) will be incorporated into a nucleus (n) to promote the unidirectional growth, as described in terms of the preferential interface nucleation [24]. The following propagation stage is just propagation of the stacking

sequence that was determined during the nucleation stage. Therefore, it is reasonable to assume that the stacking sequence of each layer in NWs is determined during the nucleation stage.

The NWs grown by the SA epitaxy tend to generate hexagonal cross-section with {110} side facets [13,15,17,37] as shown in Fig. 5.5. Therefore, the form of the crystal and nucleus was set to the hexagonal prism composed of (111)A or (111)B top surface and {110} side surfaces of the ZB structure: 'volume (V)', 'perimeter length (P)', and 'top surface area (A)' terms in the change in Gibbs free energy (that is, Eq. (2.20) in section 2.5.3) were set to $\frac{6\sqrt{3}}{4}r^2h$, $6rh$, and $\frac{6\sqrt{3}}{4}r^2$, respectively; $\gamma_{(top)}$ was given by the surface energy of either (111)A or (111)B; and $\gamma_{(side)}$ was given by the surface energy of (110). In addition, according to the layer-by-layer mechanism, the height (h) of the nucleus was assumed to be one Ga–As bilayer thickness along the <111> direction, 3.24 Å.

Nucleation can occur on the top surface without SF and on the top surface with SF, distinguished by nucleation-I and nucleation-II in Fig. 5.5, respectively. It should be noted that the change in Gibbs free energy by the formation of a nucleus, ΔG_{sn} in Eq. (2.20), depends on $\gamma_{sc(top)}$ of the previously formed layers. This means that nucleation on the current layer highly depends on the surface structure of the previously formed underlying layer. Therefore, the situation will be different between the nucleation-I and nucleation-II, and each nucleation will be separately investigated in the following sections.

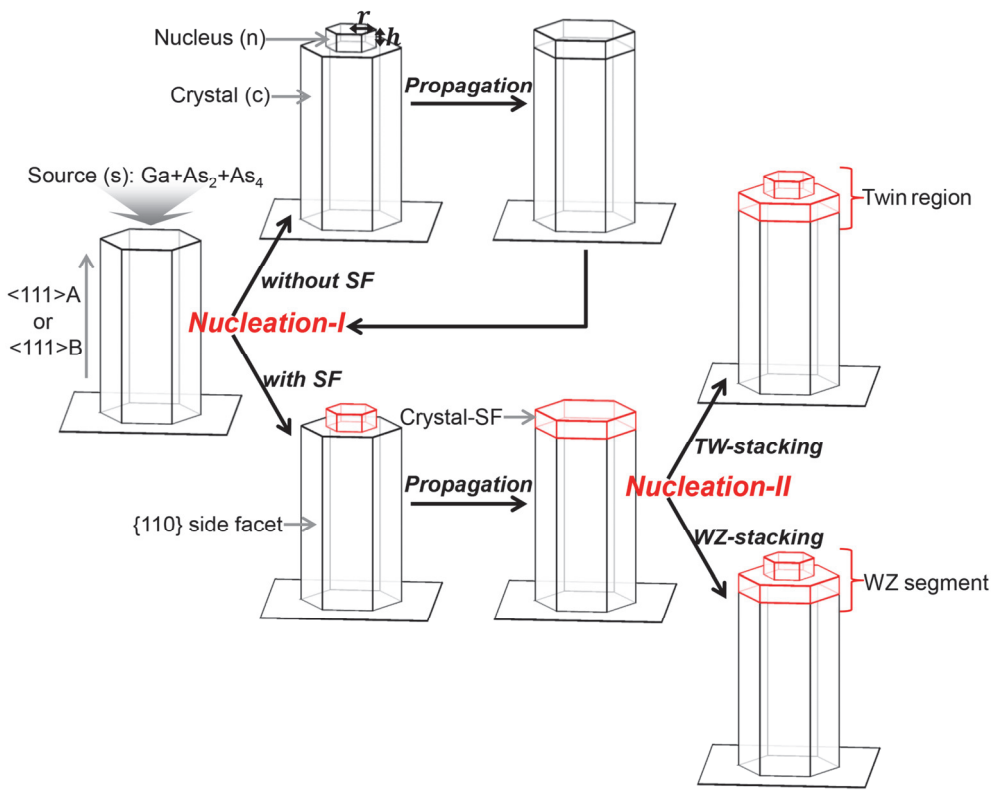

Figure 5.5 Schematic of the nanowire growth processes for the facet-driven VS method.

5.3.2. Nucleation I: zinc-blende vs. stacking-fault

Figure 5.6 shows the procedure to evaluate ΔG_{sn} for the simplest case, nucleation-I-w/o-SF in the upper panel of Fig. 5.5: a nucleus without SF is formed on the crystal surface without SF. In this case, the top surfaces before and after the nucleation are identical, which means that the third term in Eq. (2.20), the change in top surface energy, is zero. The values of the other terms, the change in chemical potential by the incorporation of sources into the nucleus, $\Delta\mu_{sn}$, and the appearing side surface energy, $\gamma_{sn(110)}$, were obtained as a function of T and P_{As} (= P_{As2}+P_{As4}) by calculating the T–P dependent chemical potential and surface energy.

Figure 5.6(a) shows the calculated chemical potentials of the nucleus ($\mu_{n(GaAs)}$) and sources ($\mu_{s(Ga)}$ and $\mu_{s(As)}$) in the most stable phase under the relevant T at a fixed P_{As} of 3×10^{-9} atm: ZB for n(GaAs), orthorhombic for s(Ga), and gas mixture consisting of As_2 and As_4 molecules for s(As), respectively. The methods to calculate the chemical potential of solid and vapor phases are described in section 2.3.1 and 2.3.2, respectively. These values were used to obtain the T–P dependent incorporation energy, $\Delta\mu_{sn} = \mu_{n(GaAs)} - \mu_{s(Ga)} - \mu_{s(As)}$, as shown in Fig. 5.6(b). The decrease in $\Delta\mu_{sn}$ with decreasing T indicates that the driving force for nucleation becomes stronger as T decreases. Figure 5.6(c) shows the minimum total surface energies for the (110), (111)A and (111)B surfaces calculated by using the method described in section 2.3.3 and 2.3.4. Figure 5.6(d) shows the calculated ΔG_{sn} (thick black curve) in Eq. (2.20) as a function of the nucleus radius (r) at fixed T of 913 K and P_{As} of 3×10^{-9} atm, which is the common growth condition of GaAs using MBE [21,28]. The gray line with negative values corresponds to the first term in Eq. (2.20), which acts as the driving force for nucleation, while the orange line with positive values corresponds to the second term in Eq. (2.20), which acts as the energy cost for nucleation. It is notable that the nucleation barrier, $\Delta G^*_{sn(ZB)}$, becomes twice for the nucleus of two bilayers (h= 6.48 Å), implying that nucleation with more than one bilayer is almost improbable.

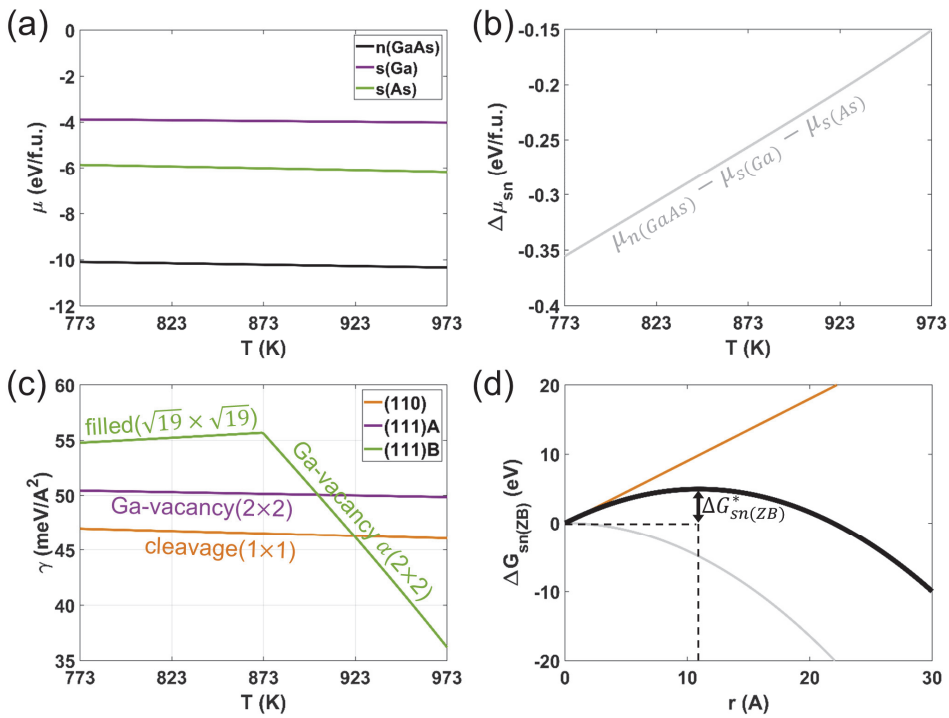

Figure 5.6 (a) Chemical potentials of GaAs nucleus (n), Ga source (s), As source (s), and (b) the change in chemical potential by the incorporation of sources into the nucleus as a function of T at a fixed P_{As} (= P_{As2}+P_{As4}) of 3×10^{-9} atm. (c) Total surface energy ($\gamma = \gamma^{elec} + \Delta\gamma^{vib}$) of the most stable reconstructions as a function of T at a fixed P_{As} of 3×10^{-9} atm. (d) The change in Gibbs free energy by the nucleation-I-w/o-SF (thick black curve) as a function of nucleus radius at fixed T of 913 K and P_{As} of 3×10^{-9} atm. The gray and orange lines denote the first and second terms in Eq. (2.20), respectively.

On the other hand, if an SF accidentally forms at the top surface during growth, nucleation-I-w/-SF in the lower panel of Fig. 5.5, there will be additional energy for the change in top surface energy, the third term in Eq. (2.20). That is, the top surface energy after the nucleation, $\gamma_{cn(111)} + \gamma_{sn(111)}$, is not equal to, but might be higher

than, the top surface energy before the nucleation, $\gamma_{sc(111)}$. To estimate the amount of the additional energy cost, reconstructed structures without and with SF on the top layer were generated. From now on, the T range where the Ga-vacancy α(2×2) is the most stable reconstruction of the (111)B surface will be focused on, because the study in section 5.2 confirmed that BNWs start to grow when the stable reconstruction of (111)B is Ga-vacancy α(2×2).

Figure 5.7(a) and (b) reveal the side views of the reconstructions without and with SF, respectively, for the GaAs ANW and BNW. Three types of stacking sequence along the <111> direction of the ZB structure are represented by the notation {'a', 'b', 'c'} for Ga atoms, and {'A', 'B', 'C'} for As atoms. The stacking sequence of ANW is denoted from left to right, while that of BNW is denoted from right to left, to emphasize that <111>B is the opposite direction of <111>A. The stacking sequence of ANW with nucleus having no SF (ANW-ZB) is presented by (···aAbBcCa)Ab, and the counterpart of BNW (BNW-ZB) is presented by Ca(AbBcCaA···), as shown in Fig. 5.7(a). The two characters outside of the parentheses, 'Ab' in ANW-ZB and 'Ca' in BNW-ZB, correspond to the topmost stacking sequence of the nucleus bilayer, respectively.

In this regard, the stacking sequence of ANW with nucleus having SF (ANW-SF) is presented by (···aAbBcCa)Ac, and that of BNW (BNW-SF) is presented by Ba(AbBcCaA···), as shown in Fig. 5.7(b). The atoms located in the faulted stacking sequence are highlighted by red color. Figure 5.7(c) shows the top views of the topmost Ga–As bilayer for the (111)A Ga-vacancy(2×2) without and with SF, while Fig. 5.7(d) shows those for the (111)B Ga-vacancy α(2×2) without and with SF. The Ga-vacant site is indicated by the blue arrow for each reconstruction. It should be

noted that the positions of {'a', 'b', 'c'} and {'A', 'B', 'C'} notations in Fig. 5.7 correspond to the ideal bulk positions, while the open and closed circles correspond to the reconstructed positions of Ga and As atoms, respectively. Therefore, the slight mismatches between the notations and the circles show the reconstruction and relaxation of the surface atoms.

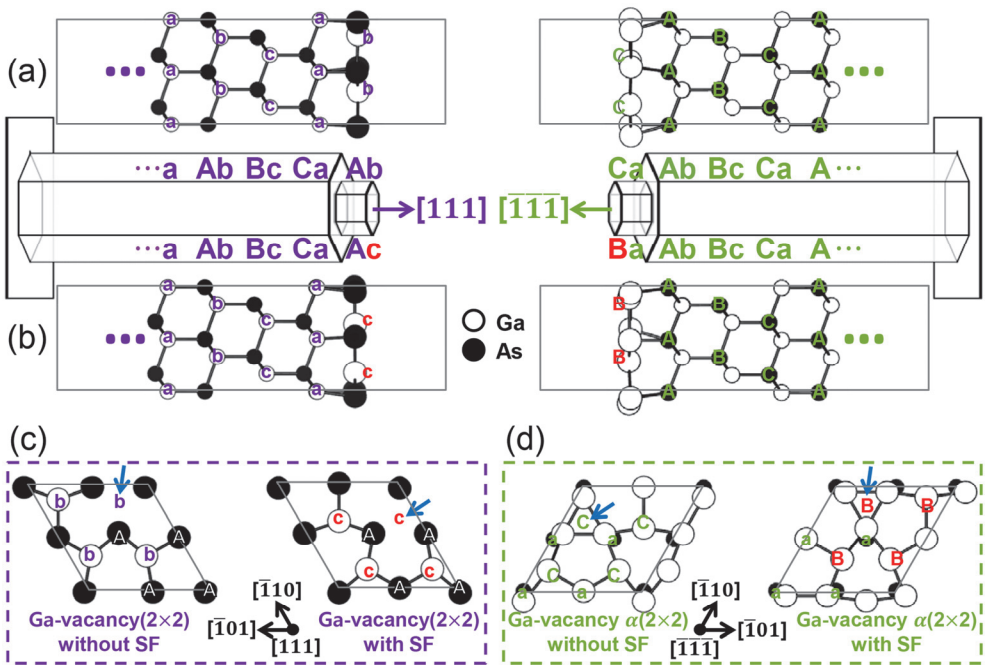

Figure 5.7 Side views of GaAs (111)A Ga-vacancy(2×2) (left) and (111)B Ga-vacancy α(2×2) (right) (a) without, and (b) with SF at the topmost layer. (c) Top views of (111)A Ga-vacancy(2×2), and (d) (111)B Ga-vacancy α(2×2) reconstructions without, and with SF. The {'a', 'b', 'c'} notations for Ga atoms and {'A', 'B', 'C'} notations for As atoms correspond to the ideal bulk positions. In the top view, only the atoms at the topmost bilayer are presented, and a vacant site is denoted by the blue arrow.

The total surface energies, $\gamma = \gamma^{elec} + \Delta\gamma^{vib}$, of the four reconstructions in Fig.

5.7 were calculated as a function of T at a fixed P_{As} of 3×10^{-9} atm as shown in Fig. 5.8(a). Figure 5.9 shows the surface phonon DOSs of the corresponding reconstructions along with the bulk phonon DOS of ZB-GaAs. As expected, the surface energy with SF is higher than that without SF for both the (111)A and (111)B surfaces. It should be noted that the amount of surface energy increase by SF, $\Delta\gamma_{SF}$ in Fig. 5.8(b), is precisely identical to the third term in Eq. (2.20), the change in top surface energy during the nucleation-I-w/-SF.

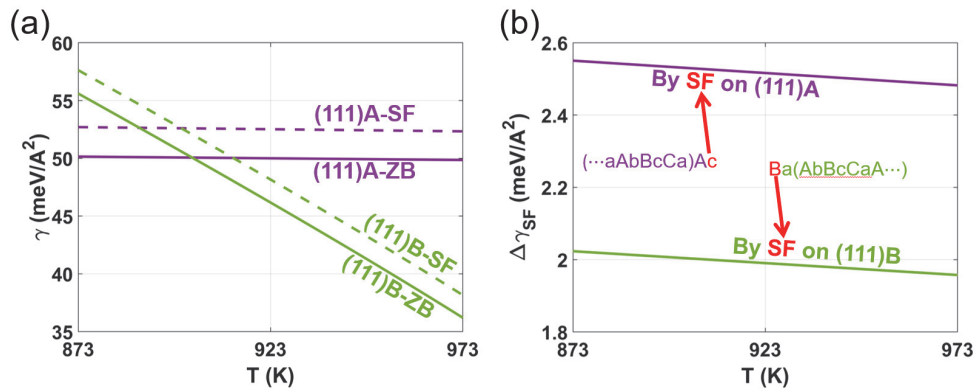

Figure 5.8 (a) Total surface energy ($\gamma = \gamma^{elec} + \Delta\gamma^{vib}$) of (111)A Ga-vacancy(2×2) (purple line) and (111)B Ga-vacancy α(2×2) (green line) without (solid line), and with (dashed line) SF. (b) The amount of surface energy increase by the SF formation at a fixed P_{As} of 3×10^{-9} atm.

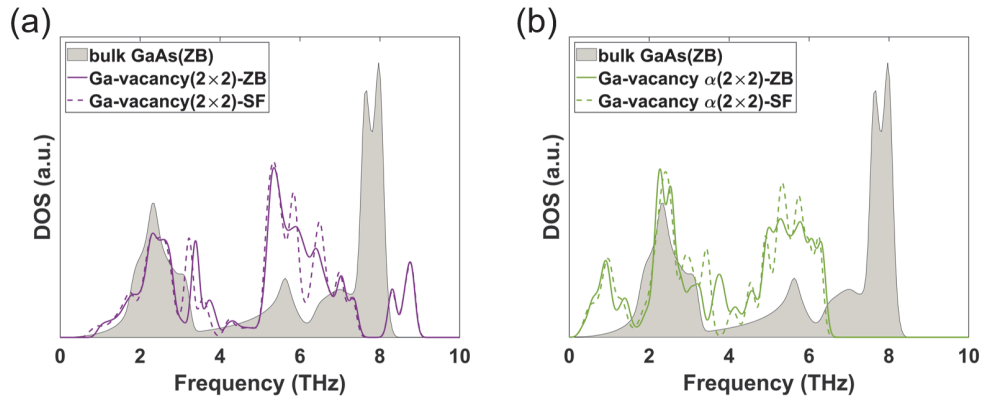

Figure 5.9 Surface phonon DOSs of (a) (111)A Ga-vacancy(2×2) and (b) (111)B Ga-vacancy α(2×2) without (solid line), and with (dashed line) SF. The shaded area corresponds to the bulk phonon DOS of ZB-GaAs.

Figure 5.10(a) shows the change in Gibbs free energy for ANW-SF (purple line) and BNW-SF (green line) in comparison with that for ANW-ZB and BNW-ZB (solid black line) at T of 913 K and P_{As} of 3×10^{-9} atm. Since the T-dependent $\Delta\mu_{sn}$, $\gamma_{sn(110)}$, and $(\gamma_{cn(111)} + \gamma_{sn(111)} - \gamma_{sc(111)})$ values were already obtained in Fig. 5.6(b), (c), and 5.8(b), respectively, the critical radius (r^*) and nucleation barrier (ΔG_{sn}^*) could be obtained under arbitrary T conditions, as shown in Fig. 5.10(b) and (c). These results demonstrate that as T increases, the r^* and ΔG_{sn}^* increase, which indicates that nucleation becomes difficult. In addition, it is notable that the r^* of ANW-SF is larger than that of BNW-SF and the corresponding ΔG_{sn}^* is also higher for ANW-SF than for BNW-SF due to the higher energy cost shown in Fig. 5.8(b).

Using the calculated nucleation barriers, the formation probability of SF sequence ($P_{n(SF)}$) was estimated by the ratio of the nucleation rate between SF- and ZB-stacking:

$$P_{n(SF)} = \frac{\dot{N}_{(SF)}}{\dot{N}_{(SF)}+\dot{N}_{(ZB)}} = \frac{\dot{C}\cdot\exp\left(-\frac{\Delta G^*_{sn(SF)}}{k_B T}\right)}{\dot{C}\cdot\exp\left(-\frac{\Delta G^*_{sn(SF)}}{k_B T}\right)+\dot{C}\cdot\exp\left(-\frac{\Delta G^*_{sn(ZB)}}{k_B T}\right)}, \quad (5.2)$$

where $\dot{N}_{(SF)}$ and $\dot{N}_{(ZB)}$ are the nucleation rate, Eq. (2.19), with SF- and ZB-stacking sequences, respectively; and $\Delta G^*_{sn(SF)}$ and $\Delta G^*_{sn(ZB)}$ are the nucleation barrier for SF- and ZB-stacking, respectively. The rate of source supply ($\dot{C}$) is determined by the surface orientation and regardless of the stacking sequence in the nucleus. Therefore, all the pre-exponential factors in Eq. (5.2) can be eliminated when calculating $P_{n(SF)}$ for each surface.

The corresponding $P_{n(SF)}$ is much lower for the growth along <111>A than along <111>B, as shown in Fig. 5.10(d). This prediction agrees well with the experimental observations about the polarity dependent stacking that the presence of SF-induced TW in BNWs is largely reduced in ANWs [28,29]. It should be also noted that $P_{n(SF)}$ decreases as T increases, even though thermal energy in Eq. (5.2) increases. This is because the ΔG^*_{sn} difference between SF- and ZB-stacking becomes larger with increasing T, as shown in Fig. 5.10(c). It clearly explains why the SF density decreases by increasing T [16-18] in the facet-driven VS growth.

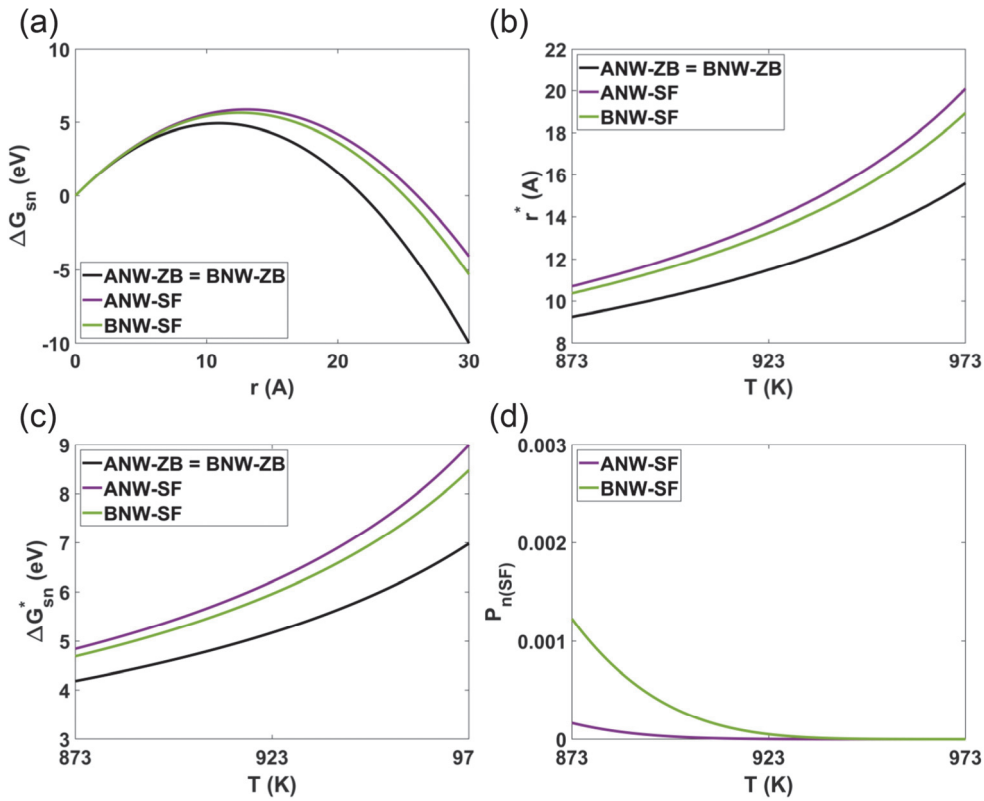

Figure 5.10 (a) Change in Gibbs free energy by the nucleation-I-w/o-SF (black line) and nucleation-I-w/-SF (purple and green lines correspond to the growth along <111>A and <111>B, respectively) at T of 913 K and P_{As} of 3×10^{-9} atm. Corresponding (b) critical radius of nucleus (r^*), (c) nucleation barrier (ΔG_{sn}^*), and (d) formation probability of SF ($P_{n(SF)}$) as a function of T at P_{As} of 3×10^{-9} atm.

As the surface reconstruction was important for determining the growth direction of the NW (section 5.2) and the ECS (chapter 4), it plays a critical role even for nucleation. Figure 5.11(a)-(d) shows the atomic structures without reconstruction corresponding to those with reconstruction in Fig. 5.7(a)-(d). The surface energy without reconstruction is much higher than that with reconstruction by more than 40 meV/Å^2, as shown in Fig. 5.11(e). This implies that the nucleation is likely to proceed

through the lower barrier path by transiently forming reconstruction on the top surface of a nucleus. In addition, $\Delta\gamma_{SF}$ for (111)B is larger than that for (111)A if the surface reconstruction is not considered, as shown in Fig. 5.11(f). This is contrary to the results in Fig. 5.8(b), leading to inconsistent calculations with experiments. It should be pointed out that the estimated size of the top surface area, using the r^* ($\cong$ 12 Å) of Fig. 5.10(b), is comparable to the area of 28 (1×1) primitive cells of (111) surface, which is sufficient to accommodate the (2×2) reconstruction.

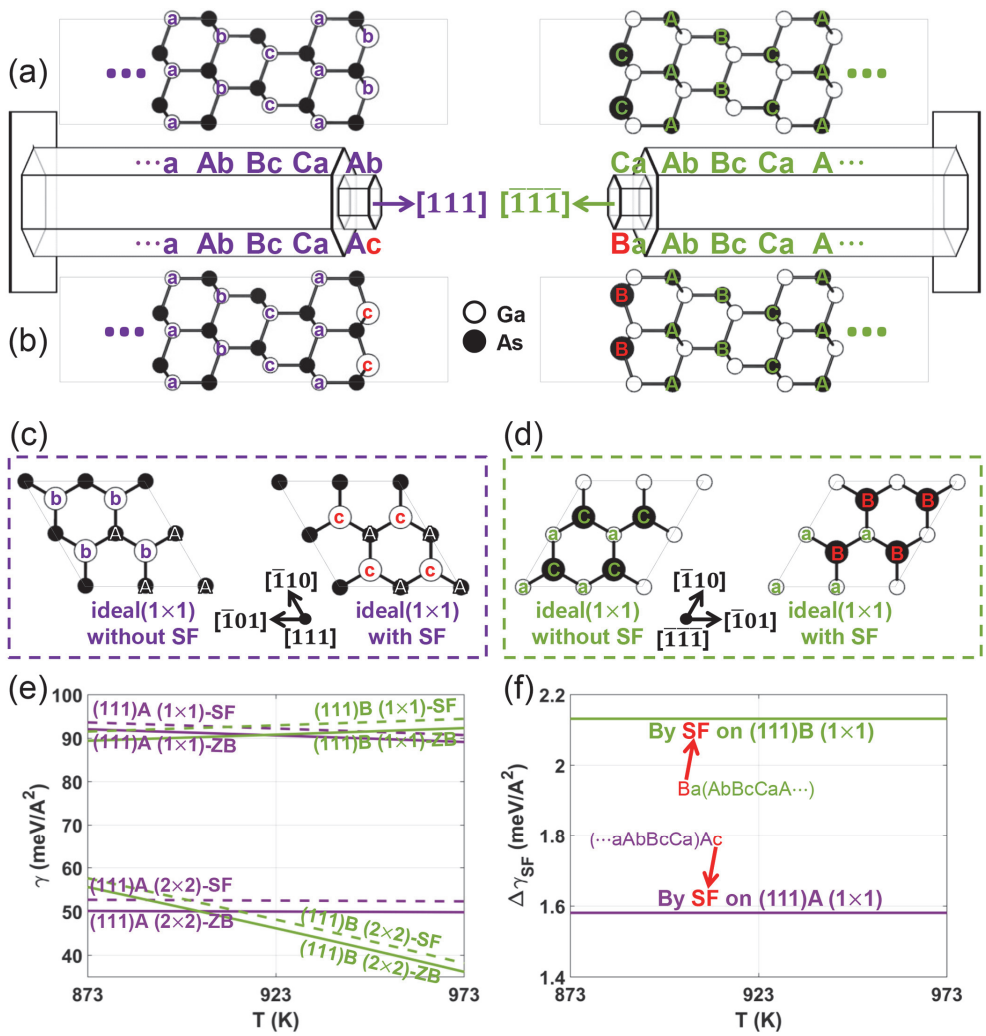

Figure 5.11 Side views of unreconstructed GaAs (111)A and (111)B surfaces (a) without, and (b) with SF at the topmost layer. (c) Top views of the unreconstructed (111)A and (d) (111)B surfaces without, and with SF. Corresponding (e) total surface energy ($\gamma = \gamma^{elec} + \Delta\gamma^{vib}$) at P_{As} of 3×10^{-9} atm without (solid line), and with (dashed line) SF. For comparison, the surface energy of (2×2) reconstructions is also presented, which is identical to Fig. 5.8. (f) The amount of surface energy increase by SF in the unreconstructed (111)A and (111)B surfaces.

5.3.3. Nucleation II: twin vs. wurtzite

Once a nucleus without SF is formed having a larger radius than r^*, it propagates across the top surface and repeats the same process in the next layer, as shown in the upper panel of Fig. 5.5, *i.e.*, (···aAbBcCa)Ab will proceed to (···aAbBcCaAb) and (···aAbBcCaAb)Bc for ANW-ZB, while Ca(AbBcCaA···) will proceed to (CaAbBcCaA···) and Bc(CaAbBcCaA···) for BNW-ZB. On the other hand, once a nucleus with SF is accidentally formed having a larger radius than r^*, the nucleus quickly propagates across the top surface resulting in a SF layer at the top of NW, *i.e.*, (···aAbBcCa)Ac proceeds to (···aAbBcCaAc) for ANW-SF and Ba(AbBcCaA···) proceeds to (BaAbBcCaA···) for BNW-SF. Then, the further growth proceeds by the nucleation-II as shown in the lower right panel of Fig. 5.5: nucleation on the crystal surface with SF. When one Ga–As bilayer is added onto the crystal surface with SF, the top surface of the nucleus has two possibilities of stacking sequences: TW- and WZ-stacking. The TW-stacking sequence of ANW-TW is (···aAbBcCaAc)Cb and that of BNW-TW is Cb(BaAbBcCaA···), as shown in Fig. 5.12(a). On the other hand, the WZ-stacking of ANW-WZ is (···aAbBcCaAc)Ca and that of BNW-WZ is Ab(BaAbBcCaA···), as shown in Fig. 5.12(b).

As for the nucleation-I, the total surface energies, $\gamma = \gamma^{elec} + \Delta\gamma^{vib}$, of the reconstructions having TW- and WZ-stacking sequences were calculated as shown in Fig. 5.12(c). The surface phonon DOSs of the corresponding reconstructions are shown in Fig. 5.13. Figure 5.12(d) shows the amount of surface energy increase by TW- and WZ-stacking regarding to the reconstruction with ZB-stacking, as denoted as $\Delta\gamma_{TW}$ and $\Delta\gamma_{WZ}$, respectively. The notations in Fig. 5.12(d) highlight the TW plane by the dashed red line, and the WZ-stacking region by the dashed red rectangle.

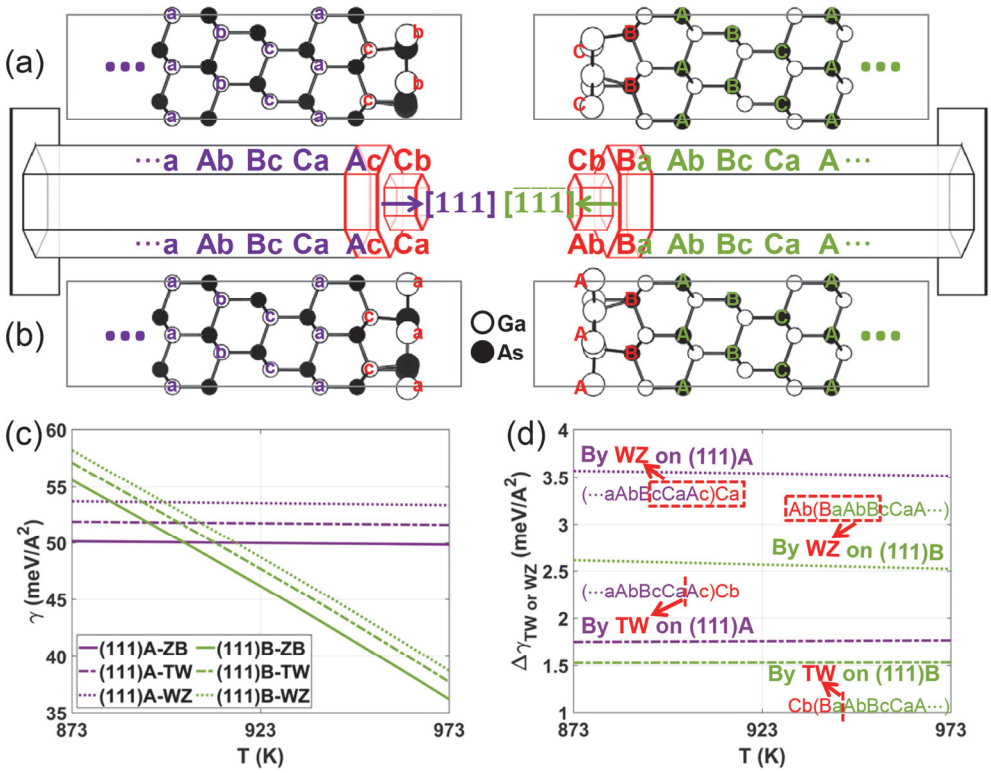

Figure 5.12 Side views of GaAs (111)A Ga-vacancy(2×2) and (111)B Ga-vacancy α(2×2) having (a) TW-, and (b) WZ-stacking sequences. Corresponding (c) total surface energy ($\gamma = \gamma^{elec} + \Delta\gamma^{vib}$) of TW- and WZ-stacking in comparison with that of ZB-stacking. (d) The amount of surface energy increase by each stacking with respect to the surface energy of ZB-stacking at P_{As} of 3×10^{-9} atm.

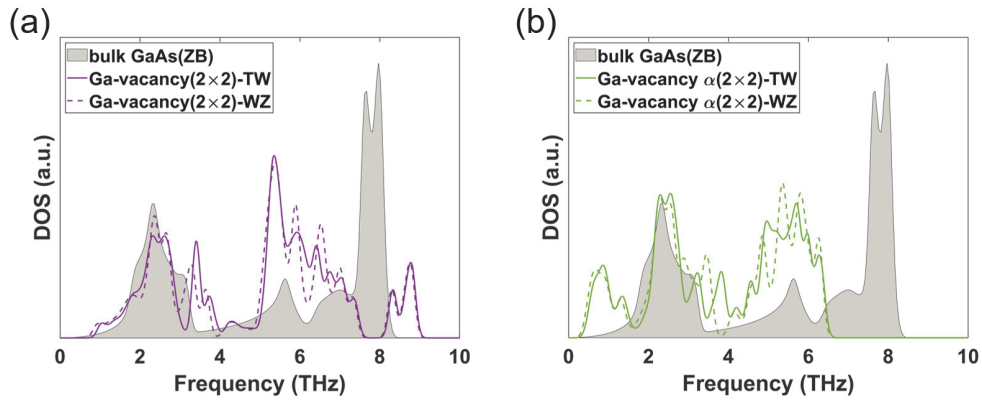

Figure 5.13 Surface phonon DOSs of (a) (111)A Ga-vacancy(2×2) and (b) (111)B Ga-vacancy α(2×2) with TW- (solid line), and WZ- (dashed line) stacking at the topmost layers. The shaded area corresponds to the bulk phonon DOS of ZB-GaAs.

It should be noted that the nucleus in ANW-WZ and BNW-WZ is no longer ZB phase. Therefore, when calculating the change in Gibbs free energy for the nucleation with WZ-stacking, the values of volume incorporation energy and side surface energy were evaluated using WZ phase: the change in chemical potential by the incorporation of sources into WZ-GaAs rather than ZB-GaAs; and the change in side surface energy by the formation of WZ$\{11\bar{2}0\}$ side facets rather than ZB$\{110\}$. Figure 5.14 shows the calculated values of the WZ phase, along with the corresponding values of the ZB phase for comparison. For the remaining third term in Eq. (2.20), the T-dependent change in top surface energy was obtained, by using the surface energy of the underlying SF-stacking (before the nucleation-II) and that of the topmost TW- and WZ-stacking (after the nucleation-II).

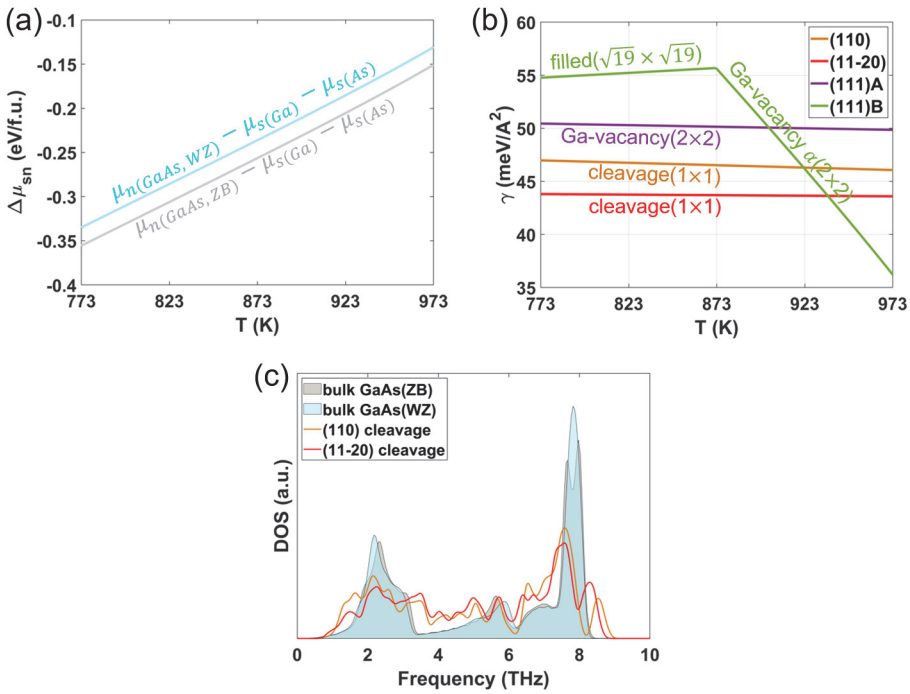

Figure 5.14 (a) Change in chemical potential by the incorporation of sources into the nucleus of ZB (gray) and WZ phase (sky blue). (b) Total surface energy ($\gamma = \gamma^{elec} + \Delta\gamma^{vib}$) of the most stable reconstructions including WZ ($11\bar{2}0$) cleavage as a function of T at a fixed P_{As} of 3×10^{-9} atm. (c) Surface phonon DOSs of (110) cleavage (dark yellow line) and ($11\,\bar{2}\,0$) cleavage (red line). The shaded area corresponds to the bulk phonon DOSs of ZB (gray) and WZ (sky blue).

Figure 5.15(a) shows the change in Gibbs free energy by the formation of a nucleus with TW- and WZ-stacking in ANW and BNW at 913 K and P_{As} of 3×10^{-9} atm, which is comparable to Fig. 5.10(a). Both the critical radius of the nucleus in Fig. 5.15(b) and the nucleation barrier in Fig. 5.15(c) are larger for WZ-stacking than TW-stacking, regardless of the NW growth direction. Figure 5.15(d) shows the formation probability of WZ-stacking compared to TW-stacking, ($P_{n(WZ)}$), which

was obtained by changing the terms in Eq. (5.2) from $\Delta G^*_{sn(SF)}$ to $\Delta G^*_{sn(WZ)}$, and from $\Delta G^*_{sn(ZB)}$ to $\Delta G^*_{sn(TW)}$, respectively. Since the difference between $\Delta G^*_{sn(WZ)}$ and $\Delta G^*_{sn(TW)}$ is lower in BNW than in ANW, as shown in Fig. 5.15(c), the $P_{n(WZ)}$ during nucleation-II is predicted to be higher in BNW than in ANW. This prediction is well-matched with the experimental observation that the local WZ segment is easily observed in BNW, while a continuous WZ section is never observed in ANW for GaAs NWs grown by SA-MBE at 913 K [28].

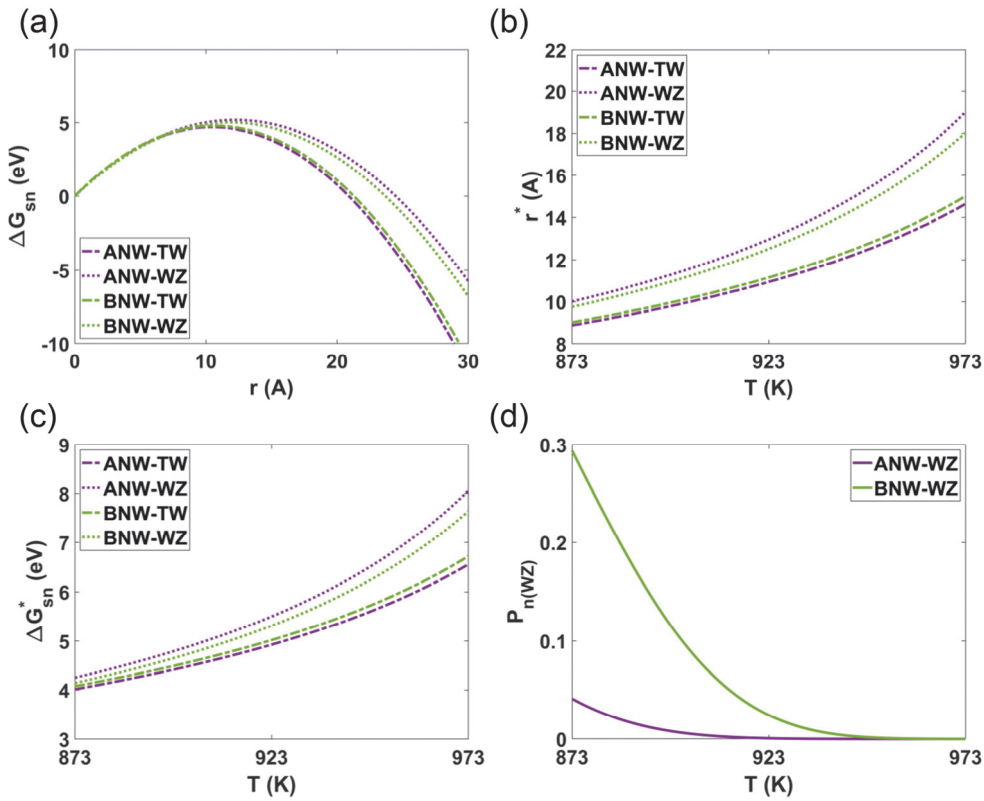

Figure 5.15 (a) Change in Gibbs free energy by the nucleation-II-TW (dashed line) and nucleation-II-WZ (dotted line) for the growth along <111>A (purple line) and <111>B (green line) at T of 913 K and P_{As} of 3×10^{-9} atm. Corresponding (b) critical radius of nucleus (r^*), (c) nucleation barrier (ΔG_{sn}^*), and (d) formation probability of WZ-stacking ($P_{n(WZ)}$) as a function of T at P_{As} of 3×10^{-9} atm.

So far, the calculation results are presented only at the fixed P_{As} of 3×10^{-9} atm, which corresponds to the common MBE conditions. Since the T–P dependent terms in Eq. (2.20), *e.g.*, $\Delta\mu_{sn}(T,P)$ and $\gamma(T,P)$, can be calculated by the same method, such prediction can be extended to any pressure. Figure 5.16(a) and (b) show the results for $P_{n(SF)}$ (extension of Fig. 5.10(d)), and $P_{n(WZ)}$ (extension of Fig. 5.15(d)), respectively, as a contour plot. The dark gray area corresponds to the

conditions under which filled(√19×√19) reconstruction is more stable than Ga-vacancy α(2×2) on the (111)B surface. Under this T–P condition, the GaAs BNW growth is not expected to occur as discussed in section 5.2. Previous experimental works reported SF density of 0.03 and 0.006 (= 3.24 Å/531 Å, where 531 Å is the average SF-free length) at 1,063 [16] and 1,123 K [17], respectively, measured by TEM for GaAs BNWs grown by SA-MOCVD (P_{As} ~10^{-5} atm). These experimental values, indicated by circular and square marks in Fig. 5.16(a), respectively, are very close to the prediction on $P_{n(SF)}$.

The overall prediction clearly demonstrates that the density of SF-induced TW and secondary WZ phase in GaAs <111> NWs can be reduced by more than one order by switching the polarity from the BNW to ANW. The prediction also suggests an alternative way that the planar defects may be suppressed by using higher T or lower P than the common growth conditions of MBE or MOCVD. However, there will be a limitation for increasing T or decreasing P, since the driving force becomes weaker and the nucleation barrier along the <111> direction becomes higher, as shown in Fig. 5.6(b), 5.10(c), and 5.15(c). This may cause the preferential nucleation along the <111> direction to no longer occur. Furthermore, increasing T or decreasing P lowers the chemical potential of the vapor phase, which can result in the decomposition of the solid into vapor under extreme conditions. In fact, there are some reports that GaAs NWs do not grow above 1,073 K by the SA-MOCVD method [14,15,17].

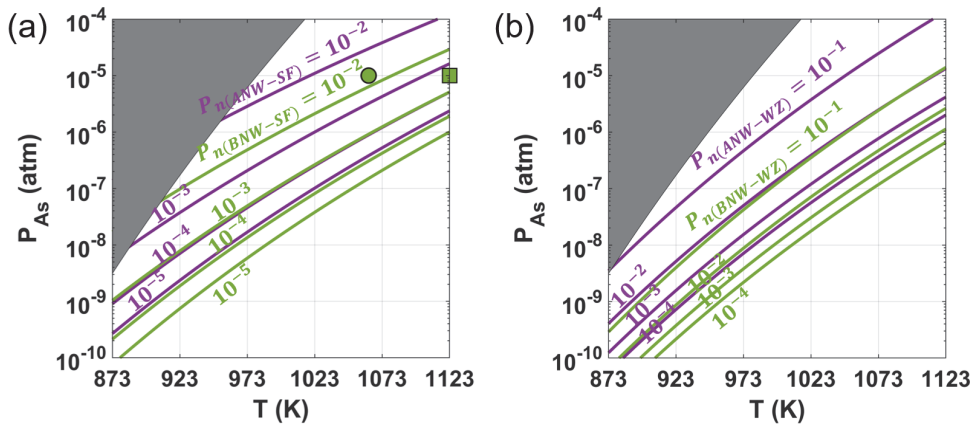

Figure 5.16 Contour plot on the formation probability of (a) SF-stacking ($P_{n(SF)}$) during nucleation-I, and (b) WZ-stacking ($P_{n(WZ)}$) during nucleation-II. The dark gray area corresponds to the T–P conditions, where filled(√19×√19) reconstruction is more stable than Ga-vacancy α(2×2) on (111)B surface. The green circular and square marks correspond to the SA-MOCVD conditions (~10^{-5} atm) of previous experiments, in which the SF density of GaAs BNWs grown at 1,063 and 1,123 K was statistically measured to be 0.03 and 0.006, respectively, by TEM.

5.4 Conclusion

In this chapter, the modeling of GaAs NW growth was carried out by focusing on the nucleation kinetics during the facet-driven VS growth processes: the repetition of adsorption, nucleation, and propagation. All the anisotropic interactions between vapor sources and solid surfaces were identified to be highly related to the reconstruction change. At the first part, the reason why the unidirectional growth is allowed only along <111>B direction in the limited T–P conditions was explained, by showing the difference in nucleation rate among the different crystallographic directions. It was found that the Ga adsorption on is favorable in most of the

experimentally relevant T–P range, while the As adsorption is preferred in the limited T–P range on the (111)B surface. The exclusive source supply onto the (111)B surface results in the preferential nucleation and NW growth along the <111>B direction. At the second part, the dependence of nucleation with various stacking sequences on T, P, and polarity was predicted. By comparing the nucleation rate and the formation probability of ZB-, SF-, TW-, and WZ-stacking between ANW and BNW, the effects of T–P growth conditions and polarity direction on each stacking sequence were quantitatively explained at the atomic-scale. As a result, the formation probabilities of SF and secondary WZ were found to decrease with increasing T or decreasing P, which agreed well with available experiments. In addition, by showing that the formation probability of the stacking defects in the BNW is about ten times higher than that in the ANW, the intriguing asymmetric stacking behavior during the growth along the polar direction and its dependence on growth conditions were fundamentally elucidated.

5.5 Bibliography

[1] O. Supplie, O. Romanyuk, C. Koppka, M. Steidl, A. Nägelein, A. Paszuk, L. Winterfeld, A. Dobrich, P. Kleinschmidt and E. Runge, Metalorganic Vapor Phase Epitaxy of III–V-on-Silicon: Experiment and Theory, *Prog. Cryst. Growth Charact. Mater.*, **64**, 103-132, (2018).

[2] P. McIntyre and A. Fontcuberta i Morral, Semiconductor Nanowires: To Grow or Not to Grow?, *Mater. Today Nano*, **9**, 100058, (2020).

[3] L. Güniat, P. Caroff and A. Fontcuberta i Morral, Vapor Phase Growth of Semiconductor Nanowires: Key Developments and Open Questions, *Chem. Rev.*, **119**, 8958-8971, (2019).

[4] K. Tomioka and T. Fukui, Recent Progress in Integration of III–V Nanowire Transistors on Si Substrate by Selective-Area Growth, *J. Phys. D: Appl. Phys.*, **47**, 394001, (2014).

[5] E. Barrigón, M. Heurlin, Z. Bi, B. Monemar and L. Samuelson, Synthesis and Applications of III–V Nanowires, *Chem. Rev.*, **119**, 9170-9220, (2019).

[6] C. Jia, Z. Lin, Y. Huang and X. Duan, Nanowire Electronics: From Nanoscale to Macroscale, *Chem. Rev.*, **119**, 9074-9135, (2019).

[7] X. Duan and C. M. Lieber, General Synthesis of Compound Semiconductor Nanowires, *Adv. Mater.*, **12**, 298-302, (2000).

[8] J. Harmand, G. Patriarche, N. Péré-Laperne, M. Merat-Combes, L. Travers and F. Glas, Analysis of Vapor-Liquid-Solid Mechanism in Au-Assisted GaAs Nanowire Growth, *Appl. Phys. Lett.*, **87**, 203101, (2005).

[9] W. Shi, Y. Zheng, N. Wang, C. Lee and S. Lee, Oxide-Assisted Growth and Optical Characterization of Gallium-Arsenide Nanowires, *Appl. Phys. Lett.*, **78**, 3304-3306, (2001).

[10] M. de la Mata, R. R. Zamani, S. Martí-Sánchez, M. Eickhoff, Q. Xiong, A. Fontcuberta i Morral, P. Caroff and J. Arbiol, The Role of Polarity in Non-Planar Semiconductor Nanostructures, *Nano Lett.*, **19**, 3396-3408, (2019).

[11] J. Motohisa, J. Noborisaka, J. Takeda, M. Inari and T. Fukui, Catalyst-Free Selective-Area MOVPE of Semiconductor Nanowires on (111)B Oriented Substrates, *J. Cryst. Growth*, **272**, 180-185, (2004).

[12] J. Noborisaka, J. Motohisa and T. Fukui, Catalyst-Free Growth of GaAs Nanowires by Selective-Area Metalorganic Vapor-Phase Epitaxy, *Appl. Phys. Lett.*, **86**, 213102, (2005).

[13] K. Ikejiri, J. Noborisaka, S. Hara, J. Motohisa and T. Fukui, Mechanism of Catalyst-Free Growth of GaAs Nanowires by Selective Area MOVPE, *J. Cryst. Growth*, **298**, 616-619, (2007).

[14] K. Ikejiri, T. Sato, H. Yoshida, K. Hiruma, J. Motohisa, S. Hara and T. Fukui, Growth Characteristics of GaAs Nanowires Obtained by Selective Area Metal–Organic Vapour-Phase Epitaxy, *Nanotechnology*, **19**, 265604, (2008).

[15] K. Tomioka, K. Ikejiri, T. Tanaka, J. Motohisa, S. Hara, K. Hiruma and T. Fukui, Selective-Area Growth of III-V Nanowires and Their Applications, *J. Mater. Res.*, **26**, 2127-2141, (2011).

[16] J. N. Shapiro, A. Lin, C. Ratsch and D. Huffaker, Temperature Dependence of Stacking Faults in Catalyst-Free GaAs Nanopillars, *Nanotechnology*, **24**, 475601, (2013).

[17] M. Yao, C. Sheng, M. Ge, C.-Y. Chi, S. Cong, A. Nakano, P. D. Dapkus and C. Zhou, Facile Five-Step Heteroepitaxial Growth of GaAs Nanowires on Silicon Substrates and the Twin Formation Mechanism, *ACS Nano*, **10**, 2424-2435, (2016).

[18] H. Yoshida, K. Ikejiri, T. Sato, S. Hara, K. Hiruma, J. Motohisa and T. Fukui, Analysis of Twin Defects in GaAs Nanowires and Tetrahedra and Their Correlation to GaAs (111)B Surface Reconstructions in Selective-Area Metal Organic Vapour-Phase Epitaxy, *J. Cryst. Growth*, **312**, 52-57, (2009).

[19] I. W. Yeu, G. Han, J. Park, C. S. Hwang and J.-H. Choi, Theoretical Understanding of the Catalyst-Free Growth Mechanism of GaAs <111>B Nanowires, *Appl. Surf. Sci.*, **497**, 143740, (2019).

[20] I. W. Yeu, G. Han, C.S. Hwang and J.-H. Choi, An ab initio approach on the asymmetric stacking of GaAs <111> nanowires grown by a vapor–solid method, DOI: 10.1039/d0nr02010a, (2020).

[21] D. Rudolph, S. Hertenberger, S. Bolte, W. Paosangthong, D. e. Spirkoska, M. Döblinger, M. Bichler, J. J. Finley, G. Abstreiter and G. Koblmüller, Direct Observation of a Noncatalytic Growth Regime for GaAs Nanowires, *Nano Lett.*, **11**, 3848-3854, (2011).

[22] B. Mandl, J. Stangl, T. Mårtensson, A. Mikkelsen, J. Eriksson, L. S. Karlsson, G. Bauer, L. Samuelson and W. Seifert, Au-Free Epitaxial Growth of InAs Nanowires, *Nano Lett.*, **6**, 1817-1821, (2006).

[23] S. Breuer, C. Pfuller, T. Flissikowski, O. Brandt, H. T. Grahn, L. Geelhaar and H. Riechert, Suitability of Au-and Self-Assisted GaAs Nanowires for Optoelectronic Applications, *Nano Lett.*, **11**, 1276-1279, (2011).

[24] B. A. Wacaser, K. A. Dick, J. Johansson, M. T. Borgström, K. Deppert and L. Samuelson, Preferential Interface Nucleation: An Expansion of the VLS Growth Mechanism for Nanowires, *Adv. Mater.*, **21**, 153-165, (2009).

[25] E. Dimakis, J. Lähnemann, U. Jahn, S. Breuer, M. Hilse, L. Geelhaar and H. Riechert, Self-Assisted Nucleation and Vapor–Solid Growth of InAs Nanowires on Bare Si (111), *Cryst. Growth Des.*, **11**, 4001-4008, (2011).

[26] C. Thelander, P. Caroff, S. Plissard, A. W. Dey and K. A. Dick, Effects of Crystal Phase Mixing on the Electrical Properties of InAs Nanowires, *Nano Lett.*, **11**, 2424-2429, (2011).

[27] D. Pelati, G. Patriarche, O. Mauguin, L. Largeau, L. Travers, F. Brisset, F. Glas and F. Oehler, GaAs (111) Epilayers Grown by MBE on Ge (111): Twin Reduction and Polarity, *J. Cryst. Growth*, **519**, 84-90, (2019).

[28] M. Zamani, G. Tütüncüoglu, S. Martí-Sánchez, L. Francaviglia, L. Güniat, L. Ghisalberti, H. Potts, M. Friedl, E. Markov, W. Kim, J.-B. Leran, V. G. Dubrovskii, J. Arbiol and A. Fontcuberta i Morral, Optimizing the Yield of A-Polar GaAs Nanowires to Achieve Defect-Free Zinc Blende Structure and Enhanced Optical Functionality, *Nanoscale*, **10**, 17080-17091, (2018).

[29] D. Q. Tran, H. T. Pham, K. Higashimine, Y. Oshima and M. Akabori, Three−Dimensional Lattice Rotation in GaAs Nanowire Growth on Hydrogen−Silsesquioxane Covered GaAs (001) Using Molecular Beam Epitaxy, *Phys. E*, **99**, 58-62, (2018).

[30] T. Akiyama, K. Sano, K. Nakamura and T. Ito, An Empirical Potential Approach to Wurtzite–Zinc-Blende Polytypism in Group III–V Semiconductor Nanowires, *Jpn. J. Appl. Phys.*, **45**, L275-L278, (2006).

[31] V. Pankoke, P. Kratzer and S. Sakong, Calculation of the Diameter-Dependent Polytypism in GaAs Nanowires from an Atomic Motif Expansion of the Formation Energy, *Phys. Rev. B*, **84**, 075455, (2011).

[32] A. Jenichen, C. Engler and B. Rauschenbach, Comparison of Wurtzite and Zinc-Blende GaAs Surfaces as Possible Nanowire Side Walls: DFT Stability Calculations, *Surf. Sci.*, **613**, 74-79, (2013).

[33] P. Aseev, A. Fursina, F. Boekhout, F. Krizek, J. E. Sestoft, F. Borsoi, S. Heedt, G. Wang, L. Binci and S. Martí-Sánchez, Selectivity Map for Molecular Beam Epitaxy of Advanced III–V Quantum Nanowire Networks, *Nano Lett.*, **19**, 218-227, (2018).

[34] D. Jacobsson, F. Panciera, J. Tersoff, M. C. Reuter, S. Lehmann, S. Hofmann, K. A. Dick and F. M. Ross, Interface Dynamics and Crystal Phase Switching in GaAs Nanowires, *Nature*, **531**, 317-322, (2016).

[35] J.-C. Harmand, G. Patriarche, F. Glas, F. Panciera, I. Florea, J.-L. Maurice, L. Travers and Y. Ollivier, Atomic Step Flow on a Nanofacet, *Phys. Rev. Lett.*, **121**, 166101, (2018).

[36] Z. Zhang, Y. Wang, H. Li, W. Yuan, X. Zhang, C. Sun and Z. Zhang, Atomic-Scale Observation of Vapor–Solid Nanowire Growth Via Oscillatory Mass Transport, *ACS nano*, **10**, 763-769, (2016).

[37] T. Yamashita, T. Akiyama, K. Nakamura and T. Ito, Effects of Facet Orientation on Relative Stability between Zinc Blende and Wurtzite Structures in Group III–V Nanowires, *Jpn. J. Appl. Phys.*, **49**, 055003, (2010).

List of Publications

Refereed Journal Articles (SCI)

1. International

[1] Woongkyu Lee, Sijung Yoo, Kyung Jean Yoon, **In Won Yeu**, Hye Jung Chang, Jung-Hae Choi, Susanne Hoffmann-Eifert, Rainer Waser, and Cheol Seong Hwang*

"Resistance switching behavior of atomic layer deposited $SrTiO_3$ film through possible formation of $Sr_2Ti_6O_{13}$ or $Sr_1Ti_{11}O_{20}$ phases"

Sci. Rep. 6, 20550 (2016).

[2] **In Won Yeu**, Jaehong Park, Gyuseung Han, Cheol Seong Hwang, and Jung-Hae Choi*

"Surface reconstruction of InAs (001) depending on the pressure and temperature examined by density functional thermodynamics"

Sci. Rep. 7, 10691 (2017).

[3] **In Won Yeu**, Gyuseung Han, Jaehong Park, Cheol Seong Hwang, and Jung-Hae Choi*

"Equilibrium crystal shape of GaAs and InAs considering surface vibration and new (111)B reconstruction: ab-initio thermodynamics"

Sci. Rep. 9, 1127 (2019).

[4] Jaehong Park, **In Won Yeu**, Gyuseung Han, Cheol Seong Hwang, and Jung-Hae Choi*

"Role of the short-range order in amorphous oxide on MoS_2/a-SiO_2 and

MoS_2/a-HfO_2 interfaces"

Phys. Status Solidi B 256*,* 1900002 (2019).

[5] Jaehong Park, **In Won Yeu**, Gyuseung Han, Chaun Jang, Joon Young Kwak, Cheol Seong Hwang and Jung-Hae Choi*

"Optical Control of the Layer Degree of Freedom through Wannier-Stark States in Polar 3R MoS_2"

J. Phys. Condens. Matter 31*,* 315502 (2019).

[6] Younjin Jang†, **In Won Yeu†**, Jun Shik Kim, Jeong Hwan Han, Jung-Hae Choi*, and Cheol Seong Hwang* **(†: equal contribution)**

"Reduction of the Hysteresis Voltage in Atomic-layer-deposited p-Type SnO Thin-Film Transistors by Adopting Al_2O_3 Interfacial Layer"

Adv. Electron. Mater. 5*,* 1900371 (2019).

[7] **In Won Yeu**, Gyuseung Han, Jaehong Park, Cheol Seong Hwang, and Jung-Hae Choi*

"Theoretical understanding of the catalyst-free growth mechanism of GaAs <111>B nanowires"

Appl. Surf. Sci. 497*,* 143740 (2019).

[8] Jaehong Park, **In Won Yeu**, Gyuseung Han, Cheol Seong Hwang and Jung-Hae Choi*

"Ferroelectric switching in bilayer 3R MoS_2 via interlayer shear mode driven by nonlinear phononics"

Sci. Rep. 9*,* 14919 (2019).

[9] Kai Liu, **In Won Yeu**, Cheol Seong Hwang, and Jung-Hae Choi*

"Initial oxidation and surface stability diagram of Ge(100) as a function of

the temperature and oxygen partial pressure through ab-initio thermodynamics"

Phys. Scr. 95, 025701 (2020).

[10] **In Won Yeu**, Gyuseung Han, Cheol Seong Hwang, and Jung-Hae Choi "An ab initio approach on the asymmetric stacking of GaAs <111> nanowires grown by a vapor-solid method"

Nanoscale, DOI: 10.1039/D0NR02010A (2020).

Conferences

1. Domestic

[1] **In Won Yeu**, Cheol Seong Hwang, and Jung-Hae Choi "Surface structure and surface energies of InAs"

ESCW2015, Jun. 18-19 (2015), KIAS (고등과학원), Korea, Poster.

[2] **In Won Yeu**, Cheol Seong Hwang, and Jung-Hae Choi "Oxidation Study on the (100), (110) and (111) Surfaces of InAs by ab-initio Calculations"

The 23rd Korean Conference on Semiconductors (KCS 2016), Feb. 22-24 (2016), High1 resort, Korea, Oral.

[3] Jung-Hae Choi, **In Won Yeu**, Gyuseung Han, Krishnamohan Thekkepat, Mahesh Chandran, Seung-Cheol Lee, and Cheol Seong Hwang "Surface, adsorption/desorption and solid solution of III-V compound semiconductors; First principle studies"

한국세라믹학회 추계학술대회, Nov. 23-25 (2016), Seoul COEX, Korea, Invited.

[4] **In Won Yeu**, Cheol Seong Hwang, and Jung-Hae Choi
"DFT study on the clean-up mechanism of InGaAs(001) native oxides in atomic layer deposition"
The 24th Korean Conference on Semiconductors (KCS 2017), Feb. 13-15 (2017), 대명비발디파크, Korea, Oral.

[5] **In Won Yeu**, Cheol Seong Hwang, and Jung-Hae Choi
"Surface morphology of InAs considering entropy effects"
ESCW2017, Jun. 15-16 (2017), KIAS (고등과학원), Korea, Poster.

[6] **In Won Yeu**, Gyuseung Han, Cheol Seong Hwang, and Jung-Hae Choi
"Surface reconstruction and equilibrium shape of III-V compound semiconductors as a function of pressure and temperature by ab-initio thermodynamics"
The 25th Korean Conference on Semiconductors (KCS 2018), Feb. 5-7 (2018), High1 resort, Korea, Oral.

[7] Gyuseung Han, **In Won Yeu**, Mahesh Chandran, Seung-Cheol Lee, Cheol Seong Hwang, and Jung-Hae Choi
"Prediction of the atomic configuration and electronic properties of Ga(As,Sb) solid solution using cluster expansion method"
The 25th Korean Conference on Semiconductors (KCS 2018), Feb. 5-7 (2018), High1 resort, Korea, Oral.

[8] **In Won Yeu**, Gyuseung Han, Cheol Seong Hwang, and Jung-Hae Choi
"Equilibrium crystal shape of GaAs and InAs by ab-initio

thermodynamics"

ESCW2018, Jun. 21-22 (2018), KIAS (고등과학원), Korea, Poster.

[9] **In Won Yeu**, Gyuseung Han, Cheol Seong Hwang, and Jung-Hae Choi
"Effect of the two-dimensional strain on the equilibrium crystal shape of GaAs by ab-initio thermodynamics"
The 26th Korean Conference on Semiconductors (KCS 2019), Feb. 13-15 (2019), 웰리힐리파크, Korea, Oral.

[10] Younjin Jang, **In Won Yeu**, Jun Shik Kim, Jeong Hwan Han, Jung-Hae Choi and Cheol Seong Hwang
"Reduction of Hysteresis in p-Type Atomic Layer Deposited SnO Thin Film Transistors by Adopting Al_2O_3 Interfacial Layers"
The 26th Korean Conference on Semiconductors (KCS 2019), Feb. 13-15 (2019), 웰리힐리파크, Korea, Poster.

[11] Gyuseung Han, **In Won Yeu**, Seung-Cheol Lee, Cheol Seong Hwang, and Jung-Hae Choi
"Phase diagram of Ga(As,Sb) and (In,Ga)As by cluster expansion and DFT calculations"
The 26th Korean Conference on Semiconductors (KCS 2019), Feb. 13-15 (2019), 웰리힐리파크, Korea, Oral.

[12] **In Won Yeu**, Gyuseung Han, Cheol Seong Hwang, and Jung-Hae Choi
"Theoretical understanding on the growth and stacking-fault mechanism of GaAs nanowires grown by catalyst-free method"
ESCW2019, Jul. 4-5 (2019), KIAS (고등과학원), Korea, Poster.

[13] Gyuseung Han, **In Won Yeu**, Cheol Seong Hwang, and Jung-Hae Choi "Structure stability and dielectric constant of (Be,Mg)O solid solution" *ESCW2019,* Jul. 4-5 (2019), KIAS (고등과학원), Korea, Poster.

[14] **In Won Yeu**, Gyuseung Han, Cheol Seong Hwang, and Jung-Hae Choi "Atomistic Understanding on the Growth and Stacking-Fault of GaAs Nanowires Grown by Noncatalytic Method" *The 27th Korean Conference on Semiconductors (KCS 2020),* Feb. 12-14 (2020), High1 Resort, Korea, Poster.

[15] Gyuseung Han, **In Won Yeu**, Cheol Seong Hwang, and Jung-Hae Choi "Theoretical Understanding and Design of High Dielectric Constant (Be,Mg)O Solid Solution" *The 27th Korean Conference on Semiconductors (KCS 2020),* Feb. 12-14 (2020), High1 Resort, Korea, Oral.

[16] Kun Hee Ye, Gyuseung Han, **In Won Yeu**, Beom Yong Kim, Cheol Seong Hwang, and Jung-Hae Choi "First Principles Study on the Ferroelectricity in (AlN)m/(ScN)n Superlattices" *The 27th Korean Conference on Semiconductors (KCS 2020),* Feb. 12-14 (2020), High1 Resort, Korea, Poster.

[17] Younjin Jang, **In Won Yeu**, Jun Shik Kim, Sukin Kang, Yonghee Lee, Kwangmin Kim, Whayoung Kim, Jeong Hwan Han, Jung-Hae Choi, and Cheol Seong Hwang "Atomic-Layer-Deposited Tin Monoxide Channel for p-Type Oxide Thin-Film Transistors,"

The 27th Korean Conference on Semiconductors (KCS 2020), Feb. 12-14 (2020), High1 Resort, Korea, Poster.

2. International

[1] **In Won Yeu**, Cheol Seong Hwang, and Jung-Hae Choi
"Reconstruction structure of InAs surfaces and their effects on electronic structure"
Psi-K 2015, Sept. 6-10 (2015), Donostia/San Sebastian, Spain, Poster.

[2] **In Won Yeu**, Cheol Seong Hwang, and Jung-Hae Choi
"Oxygen Adsorption Behavior of InAs Nanowire by Ab-initio Calculations"
IUMRS-ICEM 2016, Jul. 4-8 (2016), Suntec City, Singapore, Oral.

[3] **In Won Yeu**, Gyuseung Han, Cheol Seong Hwang, and Jung-Hae Choi
"Surface phase diagram of GaAs(001) considering the vibrational thermal energy by ab-initio calculation"
IUMRS-ICEM 2018, Aug. 19-24 (2018), Daejon Convention Center, Korea, Oral.

[4] **In Won Yeu**, Gyuseung Han, Cheol Seong Hwang, and Jung-Hae Choi
"Vibrational effects on the surface energy of III-V compound semiconductors using ab-initio thermodynamics"
The 21st Asian Workhop on First-Principles Electronic Structure Calculations (Asian21), Oct. 29-31 (2018), KAIST, Daejeon, Korea, Poster.

[5] Gyuseung Han, **In Won Yeu**, Seung-Cheol Lee, Cheol Seong Hwang, and Jung-Hae Choi

"Phase diagram of Ga(As,Sb) and (In,Ga)As by cluster expansion and DFT calculations"

The 21st Asian Workhop on First-Principles Electronic Structure Calculations (Asian21), Oct. 29-31 (2018), KAIST, Daejeon, Korea, Poster.

[6] **In Won Yeu**, Gyuseung Han, Cheol Seong Hwang, and Jung-Hae Choi

"Equilibrium crystal shape of GaAs by ab-initio thermodynamics"

International Conference on Multiscale Materials Modeling (9th MMM2018), Oct. 28 - Nov. 2 (2018), Osaka International Convention Center, Osaka, Japan, Oral.

[7] **In Won Yeu**, Gyuseung Han, Cheol Seong Hwang, and Jung-Hae Choi

"Growth mechanism of III-V nanowires depending on the temperature and pressure: ab-initio thermodynamic study"

EuroCVD 22-Baltic ALD 16, Jun. 24-28 (2019), Luxexpo, Luxembourg, Poster.

[8] **In Won Yeu**, Gyuseung Han, Cheol Seong Hwang, and Jung-Hae Choi

"Prediction of the Surface Energy from the Robust Extraction of Local Energy via Atomic Neural Network"

The 5th International Conference on Molecular Simulation (ICMS 2019), Nov. 3-6 (2019), Jeju, Korea, Poster.

[9] Gyuseung Han, **In Won Yeu**, Seung-Cheol Lee, Cheol Seong Hwang, and Jung-Hae Choi

"Prediction of the Phase Diagram of III-V Compound Solid Solution under Biaxial Strain using Cluster Expansion and DFT Calculations"
The 5th International Conference on Molecular Simulation (ICMS 2019), Nov. 3-6 (2019), Jeju, Korea, Poster.

[10] **In Won Yeu**, Gyuseung Han, Cheol Seong Hwang, and Jung-Hae Choi
"Effects of growth condition on the anisotropic growth and stacking behavior of GaAs polar nanowires: ab initio thermodynamics"
The 18th International Nanotech Symposium & Exhibition (Nano Korea 2020), Jul. 1-3 (2020), KINTEX, Korea, Oral.

[11] Gyuseung Han, **In Won Yeu**, Kun Hee Ye, Seung-Cheol Lee, Seong Hwang, and Jung-Hae Choi
"Effects of composition and atomic configuration on the bandgap of Ga(As,Sb) solid solution using cluster expansion and ab initio thermodynamics"
The 18th International Nanotech Symposium & Exhibition (Nano Korea 2020), Jul. 1-3 (2020), KINTEX, Korea, Oral.

Abstract (in Korean)

지난 수십년 동안, 온도 압력과 같은 성장 조건 혹은 성장 방향을 조절함으로써 기상 증착 방법으로 나노스케일 III-V 재료를 성장시키는 것은 굉장히 많은 발전을 이루었다. 이와 같은 나노스케일 성장에 대해서는, 성장 조건에 따라 변하는 표면 에너지나 구조가 기체 소스와 결정 표면의 이방성 상호작용을 결정짓는다. 그럼에도 불구하고, 원자스케일에서의 이해 부족은 실험과 이론적 시도를 여전히 경험적인 수준에 머무르게 하여, 성장을 미세하게 조절하기 위한 발전을 더디게 해왔다. 이 학위 논문은 III-V 나노재료의 성장을 모델링 함에 있어, 이론적인 접근 방법이 한 단계 더 발전하기 위해 필요한 밀도범함수론에 기반한 제일원리 열역학 계산 방법을 제시한다.

첫번째로, 대표적인 III-V 화합물 반도체인 GaAs (100) 표면 구조의 변화를 온도 압력에 대한 함수로 계산하였다. 제일원리 계산과 기상 증착 시스템의 열역학적 모델링을 조합하여, 임의의 온도 압력 조건에서 표면 상 변화를 예측할 수 있었다. 또한 기존의 원자스케일 계산에서 주로 무시되어 왔었던 표면 진동과 배치 엔트로피가 계산 예측에 어떤 영향을 미치는지 분석하였다. 두번째로, GaAs 의 평형 결정 형상을 계산된 저지수 표면들의 표면에너지로부터 예측하였다. 이때, 높은 엔트로피 효과에 의해 고온 조건에서 안정해지는 새로운 (111)B 표면 구조를 제시하였다. 마지막으로, GaAs 나노와이어가 <111>B 단일 방향으로만 선택적으로 자라는 메커니즘과, <111> 방향으로 GaAs

나노와이어가 성장할 때 적층 결함의 형성이 극성에 영향을 받는 이유를 설명했다. 단일 방향으로 성장하는 메커니즘은 서로 다른 결합 상태를 가지는 결정 표면에 대한 이방성 흡착에 의해 기인하는 것으로, 이는 표면 방향 별로 핵형성 속도의 현저한 차이를 유발하는 것으로 밝혀졌다. 또한 zinc-blende 구조에서 극성 방향인 <111> 의 서로 반대 방향, <111>A 와 <111>B, 으로 성장할 때 나타나는 적층 순서의 비대칭 형성은 (111)A 와 (111)B 의 표면 구조 차이에서 기인하는 것으로 설명되었다.

이번 학위 논문에서 제시한 전체적인 제일원리 기반의 계산 방법은 실험 데이터를 전혀 필요로 하지 않으면서도 임의의 온도 압력 조건에서 일어나는 성장 과정을 예측할 수 있게 한다. 계산을 통한 예측이 실험 관측과 놀랍도록 잘 맞는 것은 이 시뮬레이션 방법의 타당성을 검증해준다. 따라서 여기서 제시된 방법은 GaAs 뿐만 아니라 다른 재료의 나노스케일 성장을 예상하고 조절하는데 많은 도움이 될 수 있을 것이다.

핵 심 어: III-V 표면 구조, 평형 결정 형상, 나노와이어, 이방성 성장, 제일원리 열역학, 표면 진동

학 번: 2015-20877